Chapter 1

Introduction

This chapter gives an overview concerning the historical background of conjugated conducting polymers along with their structures and salient properties. This chapter discusses doping, formation of charge carries, band formation and charge transport in conducting polymers. The importance of poly(3,4-ethylenedioxythiophene) among the family of conducting polymers is highlighted. Different routes for the synthesis of conducting polymer nanostructures are briefly summarized. At the end of this chapter the scope of the thesis and statement of the thesis problem are presented.

1.1 Historical background

Polymeric materials have been used from the prehistoric time by human being in the form of wood, bone, skin and fibers. The synthesis of cellulose nitrate in the year 1868 was considered as the beginning of plastic industry. Despite the development of synthesis and characterization of polymers, a proper understanding of molecular structures of polymers was developed by Hermann Staudinger during 1920s [1]. Staudinger proposed that polymers were giant molecules or macromolecules and for the discovery in the field of macromolecular chemistry he was awarded the Nobel Prize in chemistry in the year 1953. Most of the polymers are electrically insulating and are used as insulating and inactive packaging materials in electronic applications. In contrast, conjugated conducting polymers are materials which exhibit electrical conductivity approaching that of metals. Conducting polymers research has roots back to the 1960s when Pohl, Katon and their co-workers first synthesized semiconducting polymers [2, 3]. The discovery of poly(sulfurnitride) $(SN)_x$, a polymeric inorganic explosive and its interesting electrical properties were a step towards research on conducting polymers [4-6]. A breakthrough in the development of conducting polymers came in 1977, when Shirakawa, MacDiarmid and Heeger discovered polyacetylene (PA). They observed that upon oxidation of PA with bromine, chlorine or iodine vapor, the conductivity of PA films enhanced by 10^9 times than that of the pristine PA [7-9]. For opening up a new era in the field

of materials science research by the discovery of conducting polymers, the Nobel Prize for chemistry was awarded to Alan J. Heeger, Alan G. MacDiarmid and Hideki Shirakawa in 2000. Figure 1.1 presents the chemical structures of some common conjugated conducting polymers.

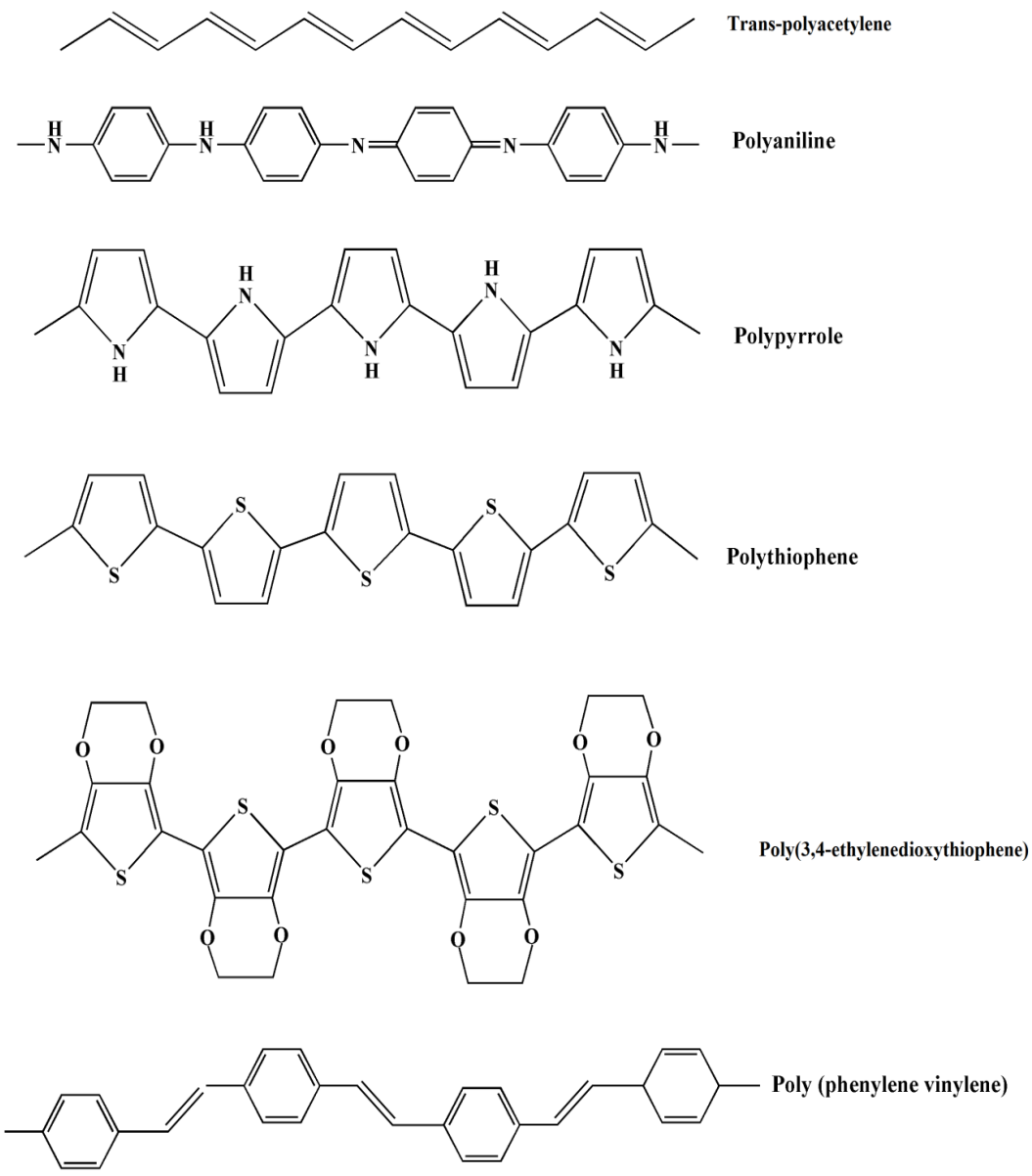

Figure 1.1: Chemical structure of some conjugated conducting polymers.

A variety of conducting polymers and its derivatives were synthesized in the subsequent years after the discovery of polyacetylene [10-13]. In the early years the research in conducting polymers was limited to the synthesis of new conducting

polymers and electrical conduction [14-16]. Gradually, the research in the field of conducting polymers focused on the study of conduction processes in doped conducting polymers, their optical properties and other physical properties [17, 18]. In the recent years, the distinct development has been made in understanding the structure-property relationship of many conducting polymers [19-21]. Conducting polymers combine the advantageous properties of common polymers such as low density, flexibility and light weight with those of organic semiconductors e.g., absorption and emission of light and tunable conductivities, which make them prospective candidates for modern electronic devices. The fascinating developments have taken place in the field of conducting polymers stimulated by various prospective applications in diverse areas such as polymer light emitting diodes [22-24], field effect transistors [25, 26], photovoltaic devices [27, 28], supercapacitor [29, 30], electrochromic windows [31-33], actuators [34-36], chemical sensors [37-39] and bio-sensors [40, 41] etc.

1.2 Salient features and Structure of conducting polymers

A special characteristic of conjugated conducting polymers is the presence of alternate single and double bonds along the polymer backbone. The basic components of organic materials are carbon and hydrogen atoms. Commonly, these compounds also contain other atomic species such as sulfur, nitrogen, oxygen and halogens. The electronic configuration of a ground state carbon atom is $1s^2\ 2s^2\ 2p^2$, which gives four electrons in the outer electronic orbit. In presence of other atoms such as hydrogen, oxygen etc., these levels may hybridize either into *sp*, sp^2 or sp^3 orbitals and each of them possesses unique spatial character. In case of conventional polymers the carbon atom is in sp^3 hybridization and all the valence electrons are paired and hence they don't conduct electricity. In conducting polymers the carbon atom is in sp^2 hybridization, as a result three of the four valence electrons are in the three sp^2 orbitals while the remaining electron is in the unhybridized $2p_z$ - orbital. The unhybridized $2p_z$ - orbital is oriented perpendicular to the three sp^2 orbitals that are coplanar with angles of 120º between each other [42]. The three sp^2 hybridized orbitals form three σ-bonds and they are located at the same plane with an angle 120° to each other. When a carbon atom binds to three other atoms it leaves one valence electron free in unhybridized $2p_z$ - orbital. This allows the overlapping of the

remaining $2p_z$ - orbitals to form π bond. The electrons in the $2p_z$ - orbitals are not associated with any specific atom or bonds which lead to delocalized electron clouds along the entire polymer chain. This builds up the conjugated π-system and allows charge mobility along the polymer backbone [43].

1.2.1 Doping in conducting polymers

Conducting polymers are either insulators or wide-gap semiconductors in their pristine neutral state. These neutral polymers need to be treated with suitable oxidizing or reducing agents to make it conducting and this phenomenon is termed as "doping". However, the doping in conducting polymer is much differs from that of inorganic semiconductors. In case of inorganic semiconductors, the dopant species occupies positions within the lattice of the host material which results either electron-rich or electron-deficient sites (holes) without charge transfer between the two sites. However, the doping process in conducting polymers is a charge transfer reaction and it can be regarded as redox reaction where removal of electron is called oxidation and the addition of electron is called reduction. Conducting polymers can be transformed into its highly conducting form by the process of doping i.e., by adding (n-doping) or removing (p-doping) electrons from the π-system present in the polymer chains. Thus, the number of electrons associated with the polymer was either decreased or increased, respectively during the doping process [44, 45]. The charge neutrality in doped conducting polymers is maintained by the incorporation of the dopant counter-ions [46]. Doping in conducting polymer is a reversible process and a doped polymer can be transformed into undoped one by the process of undoping with little or no degradation of the polymer backbone. The doping of conducting polymer leads to the formation of conjugation defects, viz. solitons, polarons or bipolarons depending upon the ground state energy nature and doping level. Some of the doping processes are discussed in the following sub-sections.

1.2.1.1 Chemical doping

The chemical doping can be performed either by removal of electrons from the polymer back-bone chain (p-doping) or by the addition of electrons (n-doping) to the chain. For better observation of p-doping and n-doping we consider the trans-

polyacetylene. p-doping is obtained by partial oxidation of polymer backbone with an oxidizing agent such as iodine [47]. The oxidation process of trans-polyacetylene is shown in eq. (1.1):

$$(CH)_x \rightarrow [CH^{y+}]_x + (xy)e^- \tag{1.1}$$

In order to preserve electrical neutrality in the system a counter-anion, A^-, must be provided,

$$[(CH)^{y+}]_x + (xy)A^- \rightarrow \left[(\mathrm{CH})^{y+}\mathrm{A}_y^-\right]_x \tag{1.2}$$

n-Doping in conducting polymer is performed through the partial reduction of polymer backbone, for example,

$$(CH)_x + (xy)e^- \rightarrow [(CH)^{y-}]_x \tag{1.3}$$

Same in the case of p-doping, in order to preserve electrical neutrality, a counter cation M^+ must be provided,

$$[(CH)^{y-}]_x + (xy)M^+ \rightarrow \left[\mathrm{M}_y^+(\mathrm{CH})^{y-}\right]_x \tag{1.4}$$

1.2.1.2 Electrochemical doping

In electrochemical doping process, a polymer coated working electrode is suspended in an electrolyte solution along with separate counter and reference electrode. In this method, the oxidation is carried out by applying a positive potential or current. As there is no need of oxidizing agent in electrochemical doping so it is possible to have greater purity of polymer film. The growth of polymer film occurs simultaneously with insertion of dopant anions and can be expressed as the stoichiometric equation:

$$nM + nyA^- \xrightarrow{oxidation} [M^{y^+}(A^-)^{y^-}]_n + n(2+y)e^- \tag{1.5}$$

where, *M* is the monomer, A^- is dopant anion which compensate the positive charge at anode and y is the doping level defined as ratio between the number of charges in the polymer and number of monomer units. The beauty of this method is that it gives doped polymer as a freestanding film [48, 49].

1.2.1.3 Photo-doping

When a conjugated conducting polymer is irradiated with photons of energy higher than the band gap of the conducting polymer, electrons are promoted to the higher energy state across the band gap. The polymer is doped and the doping process is

called photo doping. Consider the case of photo doping of trans-polyacetylene. When the irradiation is exposed on trans-polyacetylene, positive and negative solitons are generated which are delocalized over about 15 CH units. Under appropriate experimental condition of photo doping, the characteristics spectroscopic signatures of solitons can be observed. Photo doping does not sustain after the irradiation is removed due to the rapid recombination of electrons and holes. A photo-current can be obtained from a photo doped conducting polymers under the application of potential difference during irradiation process [50, 51].

1.2.1.4 Charge-injection doping

Charge-injection doping is another type of redox doping used to dope conducting polymers. The charge-injection is carried out by using a metal/insulator/ semiconductor (MIS) configuration, where the metal and conducting polymer separated by a high dielectric strength insulating thin layer. Under the application of appropriate potential difference across the MIS structure, surface charge layer is produced and the electrons and holes are injected from the metallic contacts into the π^* and π bands, respectively. In the case of charge injection doping, the polymer is either oxidized i.e., electron is added to the π^* band or reduced i.e., removed from the π band. The basic difference between charge-injection doping and chemical or electrochemical doping is that there is no counter ion associated with the doping center. The major drawback of charge-injection doping is that it is very much unstable and the charge carriers are present within the conjugated polymer till the biasing voltage is applied [50, 51].

1.2.2 Charge carriers in conducting polymers

In inorganic semiconductors, the presence of four-fold (or six-fold, etc.) coordination of every atom to its neighbor through covalent bonds leads to a rigid structure. Therefore, the electrons and holes are the dominant electronic excitation in such rigid structure. However, in case of conducting polymers the situation is somewhat different and the two-fold symmetry makes these systems more prone to structural distortion. As a result, the dominant "electronic" excitations are strongly coupled to chain distortion. Thus, rather than the electrons and holes characteristic of a rigid

lattice, soliton, polaron and bipolaron are the fundamental nonlinear excitations and the dominant charge carriers of conducting polymers [52, 53].

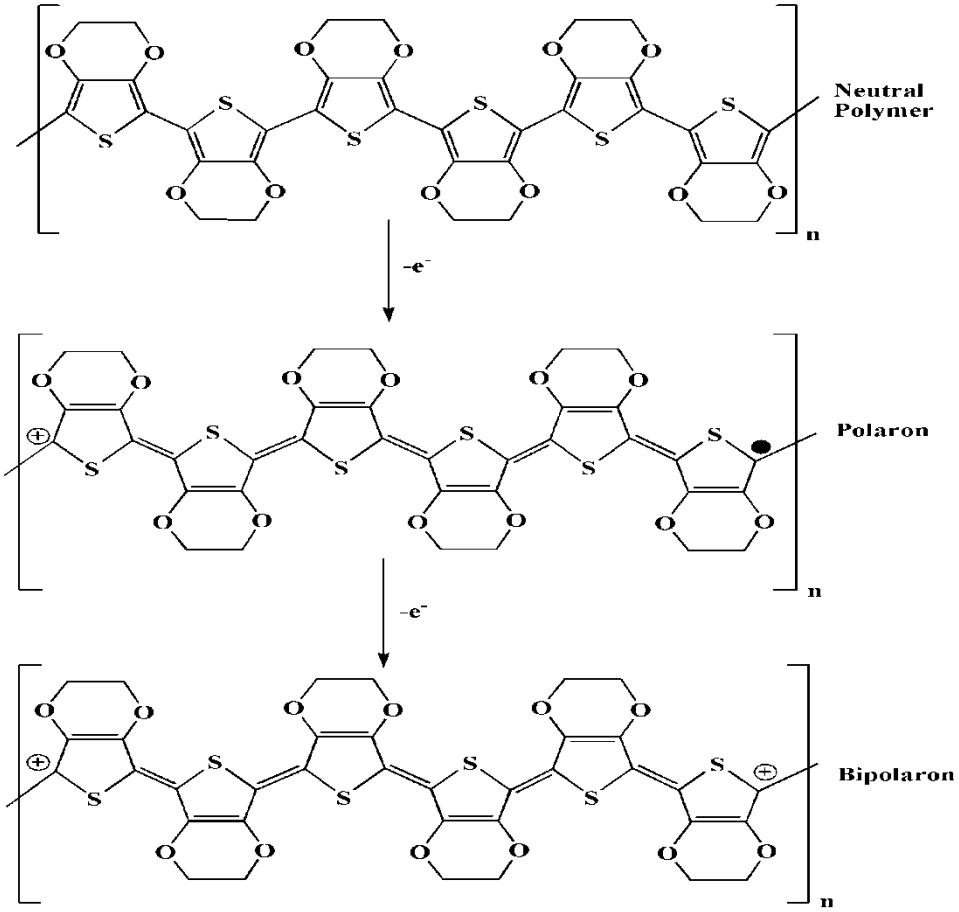

Figure 1.2: Formation of polaron and bipolaron in PEDOT upon doping.

Most of the conducting polymers have non-degenerate ground energy state i.e. the energy of the system changes upon changing the bond length alternation. Doping in conducting polymer can be achieved either by oxidation or reduction. Consider the case of oxidation; i.e. when an electron is removed from the conducting polymer chain, a free radical and a positive charge are formed. The radical and the positive cation are coupled to each other via a local resonance of the charge and the radical. The combination of a charge site and a radical is called a polaron, which can be either radical cation or radical anion. Polarons can also be defined as a radical cation or radical anion with spin ½, which is partially delocalized over some of the polymer segments. As the doping level increases, consider the removal of second

electron from the polymer chain. In that case, an electron can be dragged out either from polaron or from the conjugated polymer backbone. If the electron is removed from the neutral portion of the polymer chains then the second polaron will form. On the other hand if the electron is removed from polaron then it results a dication composed of two positive charges which are coupled through the lattice distortion. The newly formed spinless defect is known as bipolaron [54, 55]. Figure 1.2 shows the formation of polarons and bipolarons in PEDOT upon doping.

In case of conducting polymers having degenerate ground energy states, the charge carrier is different. Trans-polyacetylene falls in this category wherein the ground state has two equivalent ways of arranging the single and double bond alteration. In degenerate conducting polymers, the ground states are two-fold generate, in this condition the charged cations are not bound to each other and can freely move along the polymer chain. The charged defects are independent and they can form two separate phases of opposite orientation and identical energy. At low doping level in trans-polyacetylene, polarons are also formed but at higher doping level a different type of charge defects is formed and they are called solitons [56, 57]. Solitons have reversed spin-charge relationship i.e. charged solitons are non-magnetic, whereas neutral solitons have spin ½. The formation of polaron and soliton in trans- polyacetylene is shown in Figure 1.3.

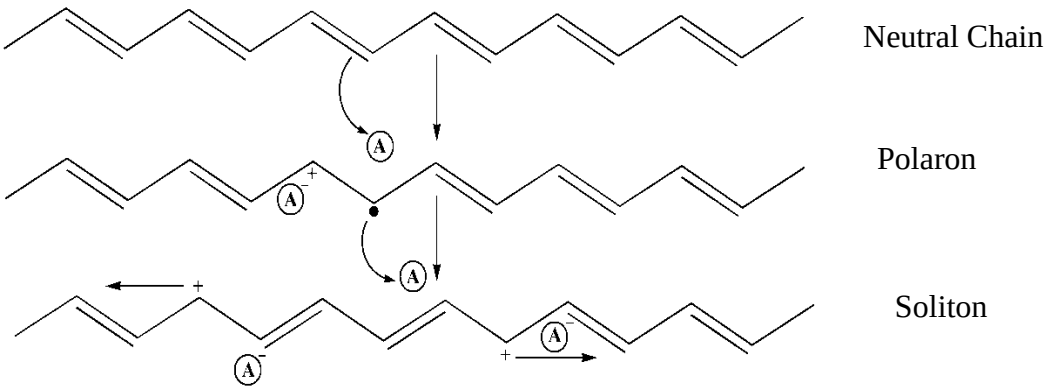

Figure 1.3: Formation of polaron and solitons in trans-polyacetylene.

1.2.3 Band structure in conducting polymers

The electrical behaviors of any material are determined by its electronic structure and the electrons move within discrete energy states called bands [58]. Metals can be considered as a crystalline arrangement of cations within a sea of electrons that are

free to move through the entire lattice under the application of an electric field. These free electrons are considered as charge carriers for the electrical conduction in metals. The theory that is used to understand the electronic structure of a material is known as band theory. According to band theory, materials can be distinguished into conductors, semiconductors and insulators from their band diagram study. For conductor, the valence band (VB) and conduction band (CB) overlap and intrinsic conductivity is attributed to the zero band gap. For semiconductor, it has narrow band gap energy and electrons can easily jump from VB to CB by thermal excitation even at room temperature. Materials where the energy separation is too large for thermal excitation to pump electrons to the CB are termed as insulators. Figure 1.4 displays the schematic energy band diagrams of conductors, semiconductors and insulators. According to Bloch theory, solids made from atoms or molecules with half filled shells lead to partially filled band with metallic transport properties. To understand the electrical properties of conducting polymers, it is important to understand the chemical structure of the system. The semiconducting property of conducting polymer arises due to the presence of delocalized π-electron bonding along the polymer chain. According to the Peierls instability [59] in one dimensional system such as in conducting polymers, the simple metallic band splits into two sub-bands, a filled valence band (highest occupied molecular orbital or HOMO level) and empty conduction band (lowest unoccupied molecular orbital or LUMO level). The band structure of a conjugated polymer originates from the interaction of the orbital of the repeating units throughout the chains. The energy difference between these two bands is termed as band gap and in neutral conjugated polymers, the π-π^* transition is considered as band gap. The band diagram study was initially focused on poly(acetylene) having degenerate ground energy states. The localized electronic state associated with soliton in nonbonding state at an energy lying at the middle of the π-π^* gap, between the bonding and antibonding levels of the perfect chain. As solitons are formed only those conducting polymers having degenerate ground energy states and they are confined to one polymer chain. Thus, there was no possibility of conduction via inter-chain hopping. The conducting polymers having non-degenerate ground states the band diagram is different. In such cases application of oxidizing potential destabilizes the VB, raising the energy of the orbital to a region between the VB and CB. The removal of electron results in a radical cation or polaron. Further oxidation results in the formation of dications or bipolarons,

dispersed over a number of rings. Figure 1.5 shows the schematic band diagram of conducting polymers having non-degenerate ground energy states.

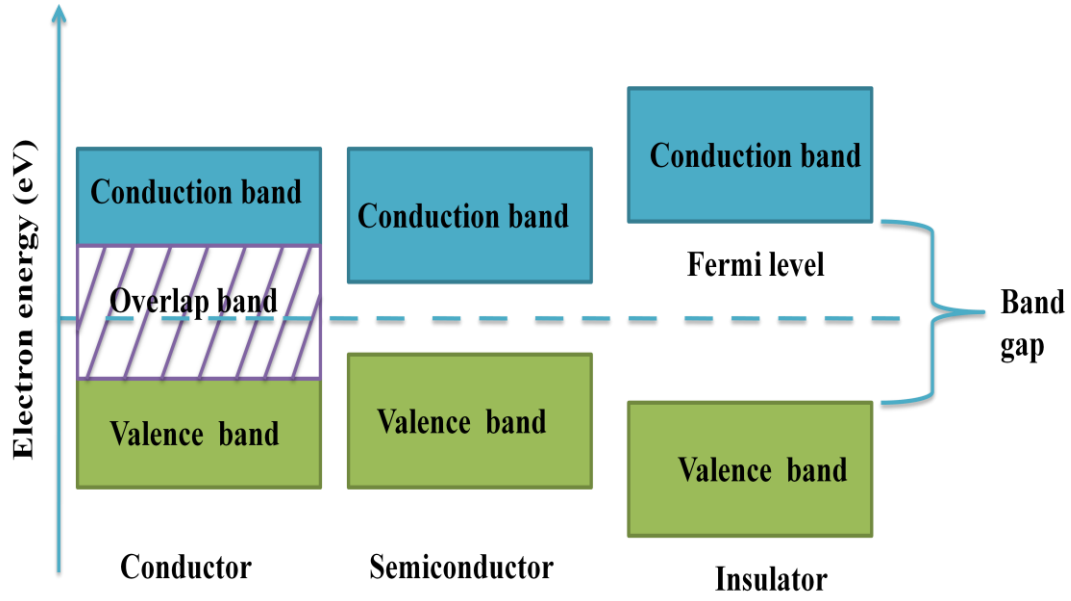

Figure 1.4: Schematic diagram of band formation in solids.

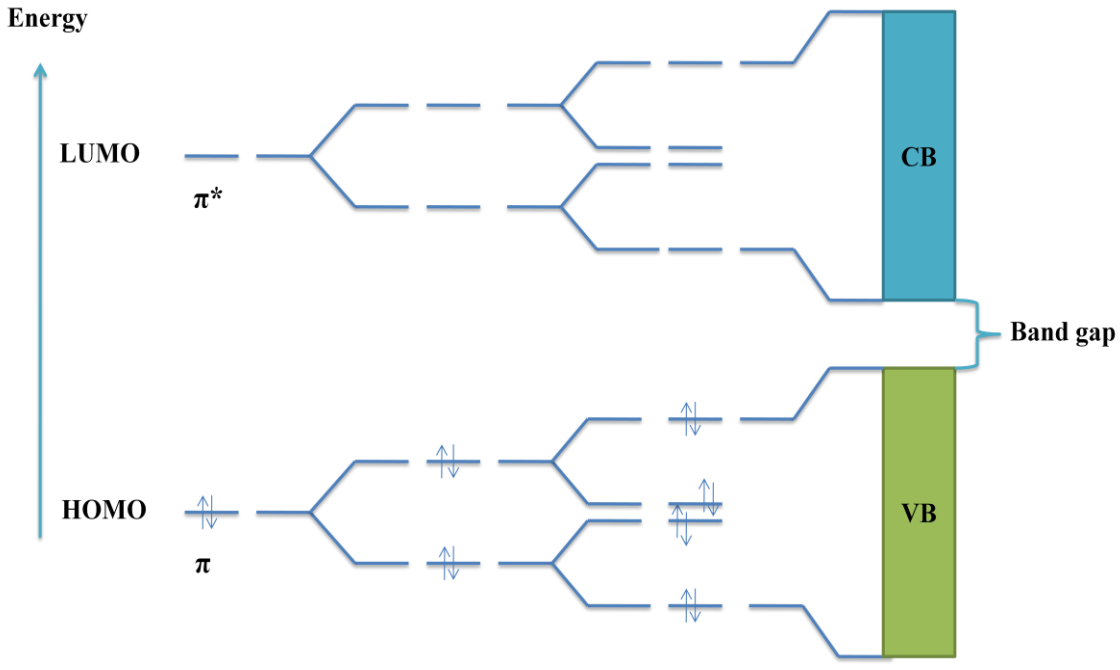

Figure 1.5: Schematic diagram of band formation in conducting polymers.

1.3 Charge transport in conducting polymers

Charge transport properties determine the applicability of a material for electronic devices. In inorganic semiconductors the charge transport is taken place through band conduction. However, in organic materials the charge transport process is very much different from that of inorganic semiconductors due to their molecular nature. The electronic conduction in conducting polymers is due to continuous strongly interacting atomic orbitals which lead to formation of electronic band structure. Conducting polymer is a heterogeneous disordered system. The inhomogeneity of conducting polymers was first addressed in 1987 by Zue et al. [60] and they proposed a model of a granular polymer metal on the basis of their DC conductivity measurements. Different experiments such as X-ray measurements [61], microwave frequency dependent conductivity [62] and NMR relaxation study [63] further supports the granular polymer metal model and it was thoroughly discussed in a paper by Prigodin and Epstein [64]. In this model, it was assumed that conducting polymers consist of small, crystalline domains separated by an amorphous or insulating region. The crystalline region would be assembled from regularly packed polymer chains whereas the amorphous region would consist of less conducting polymer fragments where the chain alignment is poor. As a result, the charge carriers are localized and charge transport within the conducting polymer involves two mechanisms: metal-like conductivity within the crystalline regions and hopping or tunneling between amorphous regions [64].

1.3.1 Effect of disorder on charge transport

The charge transport in disordered conducting polymers is greatly influenced by the presence of energetic and spatial disorder. In conducting polymers the local packing of chains determines the microscopic charge transfer rates and formation of conducting pathways [65]. Also, the fibrillar nature of many conducting polymers leads to charge carrier localization by reducing the effective dimensionality of delocalization [66]. The presence of impurities and lattice defects in disordered systems introduces backward scattering. Anderson studied this phenomenon in terms of localization effect and the disorder induces metal-insulator transition [67]. The charge carrier localization in disordered conducting polymers originates from the

rod-like quasi one-dimensional chains. The presence of partial crystallinity and impurities produces disorder in conducting polymers. The conduction of charge carrier depends on the number of defects present on the polymer and charge transport takes place between localized sites through phonon assisted hopping instead of band conduction.

1.3.2 Effect of doping concentration on charge transport

The electrical conductivity of conducting polymers results due to the formation of mobile radical cations or anions, which are generated upon doping into the π-electronic system. The attraction of an electron in one repeat unit to the nuclei in the neighboring units leads to carrier delocalization along the polymers chains and to charge carrier mobility, which is extended into three dimensions through inter-chain electron transfer. Charge transport mechanism in conducting polymers is greatly influenced by the dopant concentration. The disorder which controls the charge transport in conducting polymers can be controlled by optimizing the dopant concentration. With increasing dopant concentration, the molecular chain arrangements results in inter-chain and intra-chain order, which leads to the phase segregation of the polymer into crystalline conducting region and amorphous disorder region [68, 69]. The intra-chain electrical conductivity depends on conjugation length and number of defect in the system, whereas inter-chain conductivity depends on degree of crystallinity. The charge transport in such disordered materials is greatly influenced by the formation of crystalline moieties. The increase of doping level increases the degree of crystallinity or ordering of polymer chains leading to higher conductivity. The doping concentration dependent electronic band structure of conducting polymers is shown in figure 1.6. As the doping concentration in conducting polymers increases new energy bands are generated in between the valence band and conduction band as shown in Fig. 1.6 (b & c). At a very high dopant concentration upper and lower bipolaron bands are formed as shown in Fig. 1.6 (d) and leading to higher conductivity [70].

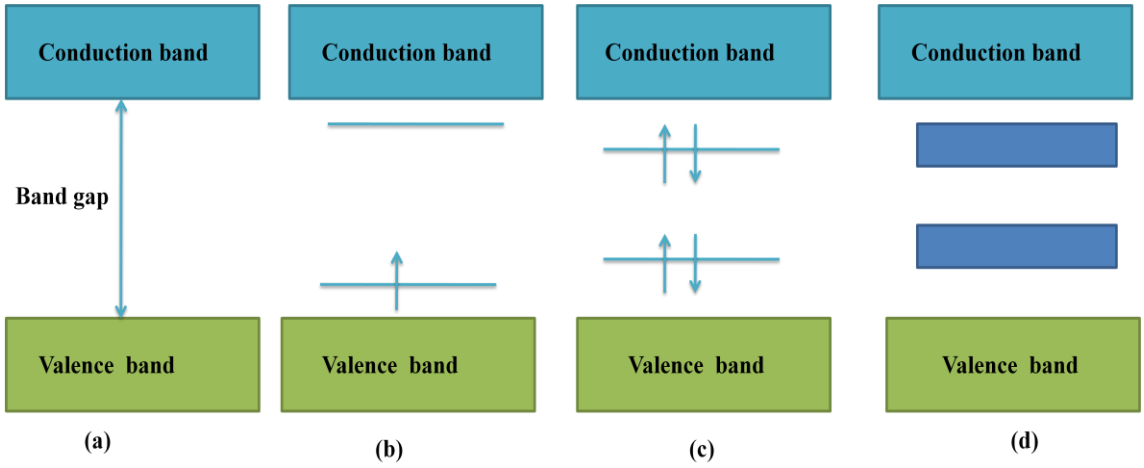

Figure 1.6: Formation of bands in conducting polymers with increasing doping concentration: (a) neutral conducting polymers, (a) formation of polaron at low doping concentration, (c) formation of bipolaron at moderate doping concentration and (d) formation of bipolaron bands at high doping concentration.

1.4 Dielectric properties of conducting polymers

Dielectric spectroscopy is a powerful tool to determine the intermolecular interactions and charge carriers relaxation present in polymeric materials. It provides a link between the investigation of the properties of the individual constituents of the complex material via molecular spectroscopy and characterization of its bulk properties. Analysis of dielectric properties gives fruitful information regarding the usefulness of these materials for different electronic applications. Moreover, the study of AC conductivity provides information about the charge transport behavior under alternating electric field [71-73]. In dielectric measurements, an AC signal is applied on the studied material, which results the positive charges to move with the electric field and negative field opposite to field direction. In other words, alignment of dipoles in the material occurs, which results in polarization. There are no permanent dipoles in conducting polymers and the charge carriers in these polymers are strongly trapped. The localized (short-range) motion of charge carriers under the applied alternating electric field acts as effective electric dipole [74]. The amount of dipole alignment, both induced and permanent is represented by the dielectric permittivity (ε') and the energy required to align the dipoles is represented by dielectric loss factor (ε'').

There are different polarization mechanisms which occur within a dielectric material under the application of alternating electric field. They are namely, electronic, ionic or atomic, dipolar or orientation and interfacial or space charge polarization. Electronic polarization occurs in a neutral atom when the external electric field displaces the electron density relative to the nucleus. Ionic or atomic polarization arises in solids having ionic bonding. Under the application of external electric field the positive and negative ions displaced from their equilibrium position resulting in net dipole moment. The dipolar or orientation polarization results from the molecules having permanent dipoles. In the absence of electric field, dipoles are oriented in random manner. When an electric field is applied, the dipoles will rotate to align in the direction of field causing orientation polarization. Interfacial polarization occurs when the motion of migrating charges is impeded and trapped within the interface of a heterogeneous system. In the absence of electric field, the space charges are randomly distributed within the interface. However, under the application of electric field the localized charge will induce its image charge on an electrode and resulting dipole moment. Figure 1.7 shows the schematic diagram of different polarization mechanisms.

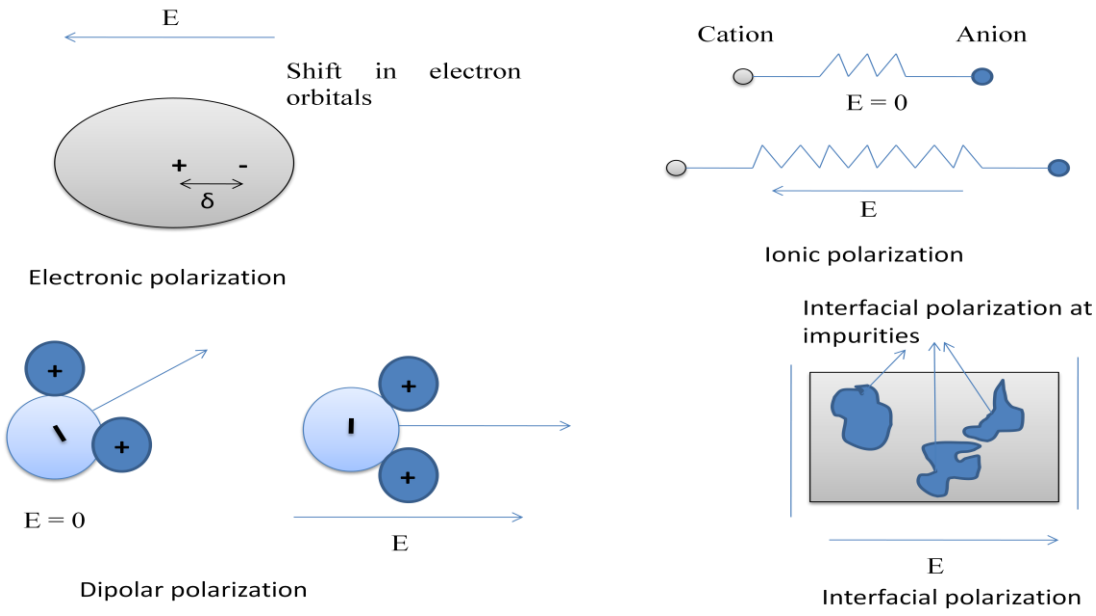

Figure 1.7: Schematic diagram of different polarization mechanisms under alternating electric field.

1.5 Conducting polymer nanostructures

Nanoscience and nanotechnology is a broad and interdisciplinary area of research that has been growing explosively worldwide in the past few years for the special properties at nano-dimension. It has the potential for revolutionizing the ways in which materials and products are created and the range and nature of functionalities that can be accessed. Materials with nanoscale dimensions not only have potential technological applications in areas such as device technology but also they have fundamental interest in that the properties of a material can change in this regime of transition between the bulk and molecular scales [75]. Conducting polymers have received considerable attention in the research field due to their distinctive electronic and optical properties, which arises due to their highly π-conjugated polymeric chains [76]. Nanostructures has large surface to volume ratio, which affect the chemical reactivity and the strength. Also at the nano scale, the quantum confinement effects become much more important determining the materials properties. Therefore, recently considerable efforts have been made to explore the possibility of improved properties by fabricating different conducting polymers nanostructures such as nanoparticles, nanofibers, nanotubes, nanospheres etc. [77]. These nanostructures of conducting polymer are found to exhibit superior properties such as high electrical conductivity, high thermal stability, improved electrochemical activity etc. as compared to their bulk counterparts [78].

1.5.1 Synthesis of conducting polymer nanostructures

Morphology and size are the two crucial parameters, which determine the properties of a material. Conducting polymers nanostructures have received extensive attention in both basic research and potential applications in nanotechnology and bio-nanotechnology [79]. The synthesis of conducting polymer nanostructures can be divided into two major categories: chemical polymerization and electrochemical polymerization. In case of chemical polymerization, the monomer reacts with an excess amount of an oxidant in a suitable solvent and the polymerization takes place spontaneously after adding oxidant. In the second method, the counter and reference electrodes are placed into the solution containing diluted monomer and electrolyte in a solvent. Polymerization starts after applying a suitable voltage and the film starts to

form on the working electrode. The main advantage of chemical polymerization over electrochemical polymerization is the possibility of large scale production. On the other hand, one of the important features of the electrochemical polymerization method is the direct formation of films [80].

1.5.1.1 Chemical polymerization

(i) Interfacial polymerization method

The interfacial polymerization is performed in an immiscible organic/aqueous biphasic system to separate the byproducts according to their solubility in the organic and aqueous phases. The interfacial polymerization technique was first developed by Huang *et al.* [81-83] and they synthesized high quality polyaniline nanofibers with controlled distribution of diameters. Interfacial polymerization process suppresses the secondary growth because the monomer and oxidant are separated by the boundary between aqueous and organic phases. Here the polymerization is restricted only at the interface where all the components needed for polymerization come together. In this method, hydrophobic monomer is dissolved in organic solvent and the hydrophilic oxidant is dissolved in aqueous solvent. When the equal amount of aqueous solvent is poured onto the organic solvent, it spreads over the organic solvent and form an aqueous/organic interface. After a short period of time the polymerization starts and colored polymers migrate into the water phase and finally filled the entire aqueous phase. As nanofibers, after formation, are continuously withdrawn from the interface, so there is no possibility of secondary growth and allow new nonofibers to grow at the interface. A schematic representation of interfacial polymerization technique is shown in Fig. 1.8.

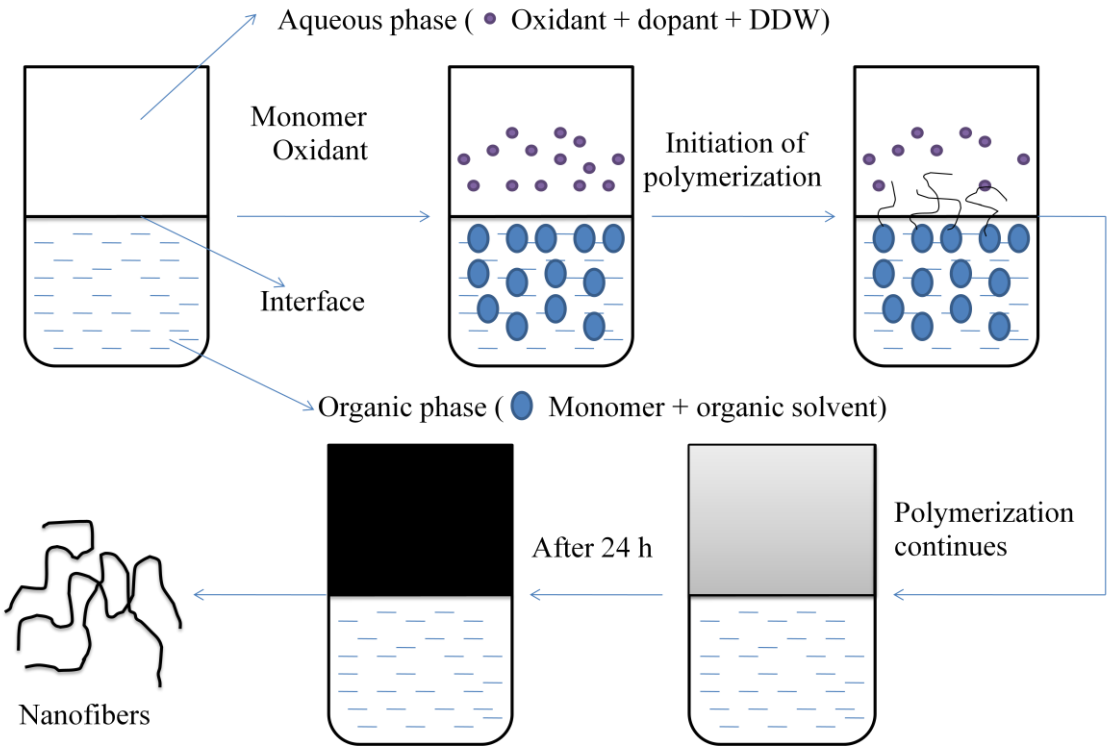

Figure 1.8: Schematic diagram of synthesis of conducting polymer nanofibers by interfacial polymerization method.

(ii) Hard template method

The hard template method was developed by Martin [84], for the synthesis of organic, inorganic and metallic nanostructures. Template assisted synthesis is an effective method for the fabrication of well designed nanostructures with controlled shape and size. Most of the studies in hard template synthesis have used two types of nano-porous materials: particle track-etched polymeric membranes (PTMs) and porous alumina membranes anodic aluminum oxide (AAO) obtained by anodic oxidation of aluminum in acid solution. PTMs are available in a wide range of pore diameter (some are as small as 10 nm), pore densities ranging from 10^5 to 10^9 pores/cm^2. However, in AAO the pore density is around 10^{11} pores/cm^2 [80]. In recent years the hard template method is widely used by several research groups for synthesis of conducting polymer nanostructures [85-89]. In this method, the polymerization of monomer has been performed inside the pores either chemically of electrochemically. During the polymerization process, the conducting polymer preferentially nucleates and grows on the pore walls. The synthesized nanostructures

are separated from the template by dissolving the nanostructures in a suitable solvent or by dissolving the template. Figure 1.9 shows the schematic diagram of synthesis of conducting polymer nanotubes using hard template. Hard template method exhibits several advantages; such as (a) the shape and size of the synthesized nanostructures can be controlled by selecting appropriate diameter of the template pore. (b) Moreover, in this method highly ordered micro or nanostructures can be obtained by simple chemical and electrochemical methods [90]. Besides these advantages, some of the disadvantages are; (a) post synthesis process is needed to remove the template which may destroy the synthesized nanostructures. (b) The quantity of the synthesized nanostructures is limited up to the number of pores that are present in the membrane. (c) Moreover, it is very difficult to synthesize templates with uniform pore sizes [91].

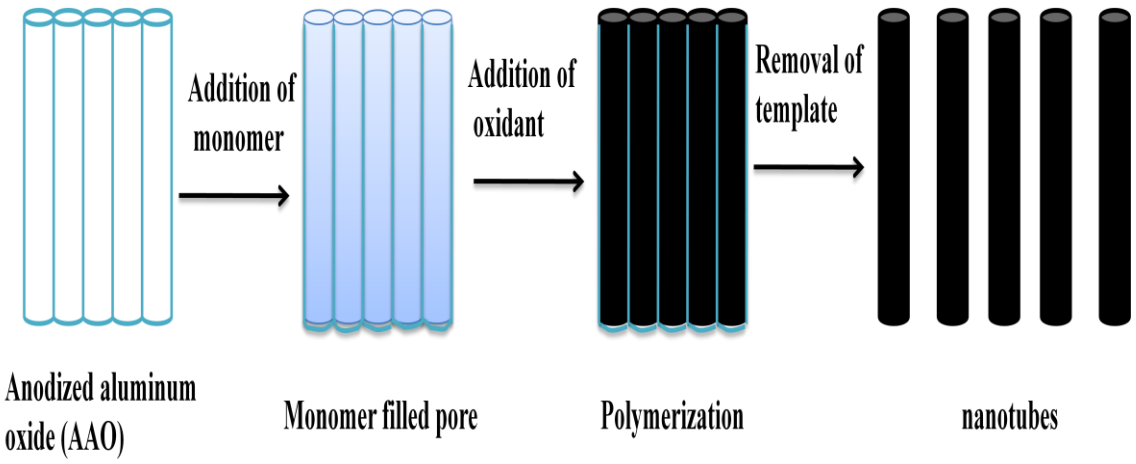

Figure 1.9: Schematic diagram of synthesis of conducting polymer nanotubes using hard template.

(iii) Soft template method

Soft template method is relatively simple, cheap and powerful method for fabrication of conducting polymer nanostructures and it is also known as self assembly method or template free method [92, 93]. This method employs some structure directed molecule such as surfactant, which forms micelles and allows the monomer to polymerize within the micelle. The self-assembly mechanism is based on the selective control of hydrogen bonding, π-π stacking, van der Waals forces and electrostatic interaction [94]. There are different soft templates which have been used

to synthesize conducting polymer nanostructures such as surfactant, liquid crystalline polymer, cycoldextrin and functionalized polymer. Among the different soft template surfactants having cationic, anionic and non-ionic amphiphilies are mostly used for the synthesis of conducting polymer nanostructures [95]. The microemulsion polymerization and reverse-microemulsion polymerization synthesis techniques fall in soft template method. Microemulsion polymerization has been widely used to synthesize conducting polymer nanoparticles, hollow nanospheres, core-shell nanostructures and nanofibers [96]. In microemulsion method (oil-in-water), the microemulsions are macroscopically homogeneous mixtures of oil, water and surfactant. Two main characteristics of oil-in-water microemulsion polymerization are: (a) the system is optically transparent and (b) there are no monomer droplets and inactive micelles exist. Reversed microemulsion polymerization (water-in-oil) method has been employed to synthesize conducting polymer nanostructures such as monodispersed nanoparticles, nanotubes and rods.

In self assembly method, the monomer or dopant-monomer super-molecules form micelles and they act as templates for the formation of nanostructures. Wan and his group have synthesized conducting polymer nanostructures such as micro/nanotubes, nanofibers and hollow microspheres. They have reported that the morphology and structural parameters of polyaniline nanostructures can be tuned by varying dopant type, dopant to monomer molar ratio, redox potential of oxidant and reaction condition [97-99]. Figure 1.10 represents the schematic mechanism of soft-template synthesis of conducting polymer nanoparticles.

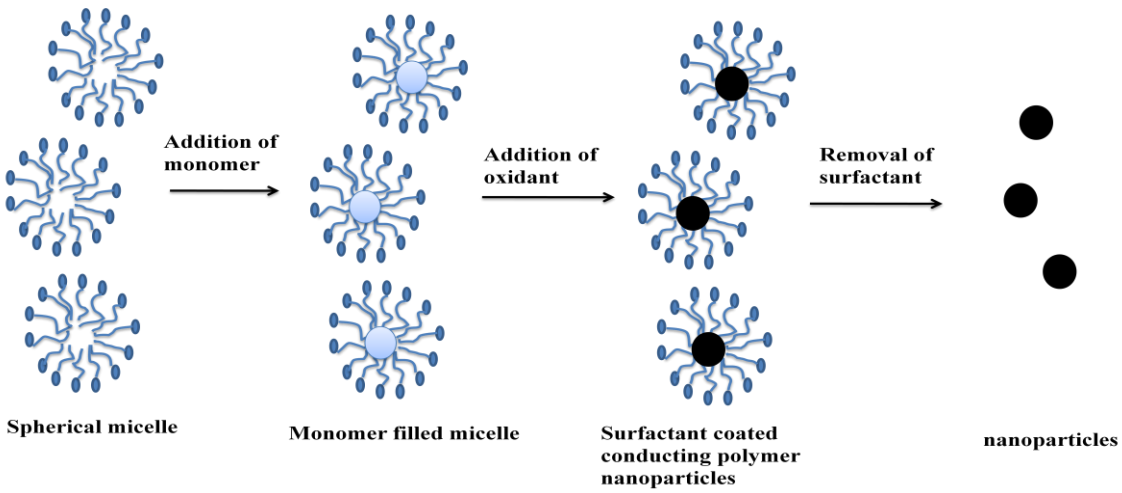

Figure 1.10: Schematic representation of synthesis of conducting polymer nanoparticles through self-assembly method.

(iv) Reactive template method

In reactive template method, the template not only directs the growth of conducting polymer nanostructures but also initiates the polymerization process of monomers by the oxidative reaction [100]. This is a simple and one step method as most of the reactive templates can be converted to soluble ion in redox reaction. Therefore, no additional purification step is required to obtain the pure polymeric nanostructures. By changing the shape and size of reactive template, one can obtain different shape and size of conducting polymer nanostructures. Lia *et al.* [101] reported synthesis of PAni nanotubes by using Mn_2O_3 nanowires as reactive template. Mn_2O_3 nanowires initiate the polymerization process and also induce the growth of PAni nanotubes on its surface. Similarly the use of methyl orange-ferric chloride (MO-$FeCl_3$) for the synthesis of PPy nanotubes has been reported by Lu *et al.* [102]. This template directs the growth of PPy nanotubes and degrades automatically during the polymerization process due to the reduction of oxidizing cations and resulting in the formation of azo functionalized PPy nanotubes in high yield.

1.5.1.2 Electrochemical polymerization method

The electrochemical polymerization is performed at conductive substrate (electrode) using the positive voltage. In case of chemical polymerization, the resultant product is in powder form whereas in electrochemical polymerization method film is deposited on the electrode. Normally, the electrochemical cell has three electrode cell arrangements namely, working, reference and counter electrode. The working electrode operates as anode on which the polymerization and deposition of film take place. The reduction of electrolyte occurs at the counter electrode, while reference electrode serves for the potential control. In recent years different research groups [103-105] have synthesized conducting polymers nanostructures like nanowires, nanotubes, nanobelts and nanospheres by using electrochemical polymerization method. In this method, a colloidal suspension of monomer is used for deposition on the electrode. Polymerization can be carried out in different way such as, potentiostatic (constant potential), galvanostatic (constant current), or potentiodynamics (potential scanning/cycling) methods [106]. Among them potentiostatic and galvanostatic methods are most commonly used to investigate the

polymerization mechanism. When a positive voltage is applied at the electrode the monomer is oxidized to form a delocalized radical cation. Radical-radical coupling reaction results the dimerization of the monomer and then chain growth proceeds via the associations of radical ions or the association of cation radical with a neutral monomer. Finally, when the chain growth is terminated then the resulted polymer film is deposited on the anodic electrode. The advantages of electropolymerization method are: (a) thin, uniform and adherent polymer films can be obtained; (b) films can be deposited on a small surface area with a high degree of geometrical conformity and controllable thickness using specific number of growth cycles in potentiodynamic cycling [107]. However, the drawback of electrochemical polymerization techniques are that a small quantity polymer is produced during polymerization and the removal of polymer thin film from the electrode surface is very difficult.

1.6 Poly(3,4-ethylenedioxythiophene) (PEDOT)

Poly(3,4-ethylenedioxythiophene) (PEDOT), a polythiophene derivatives developed in the late 1980s by the Bayer AG research laboratory in Germany is one of the most useful and promising conducting polymers for both fundamental research and application point of view [108, 109]. The main objective to produce PEDOT was to overcome the undesired α-β and β-β coupling which are generally present in polypyrrole. The undesired couplings do not take place during polymerization of PEDOT as both of the β positions are occupied by the ethylenedioxy group. As a result, the possibility of side chain reactions during polymerization is reduced and it leads to the improvement in conjugation length, giving rise to higher electronic conductivity [110, 111]. The most remarkable characteristic of PEDOT is its high environmental stability and it arises due to the 3,4-disubstituted thiophene ring. In other heterocyclic conducting polymers such as polypyrrole (PPy), these positions are prone to aerial oxidation leading to carbonyl formation and consequently lower conductivity [112]. PEDOT is a non-degenerate conducting polymer and among the different thiophene derivatives, it has received a great deal of attention among the research community due to its some excellent properties such as high environmental stability, moderate band gap at ambient temperature (1.5-1.6 eV), low redox potential (- 0.6 V), high electrical conductivity and high optical transparency (e.g., a

sheet resistance of about 100 Ω/square has been obtained at 90% transmittance) in its electrically conductive state [113-115].

The 3- and 4-position of thiophene ring in 3,4-ethylenedioxythiophene (EDOT) monomer is occupied by oxygen (shown in Fig. 1.11) and it acts as electron-donating group which increases the electron density of the thiophene ring [116]. Polymerization of EDOT takes place via 2, 5- couplings which results in polymers with fewer defect and thus possesses improved properties compared to other conducting polymers. PEDOT can be synthesized by different polymerization method such as electrochemical polymerization method, chemically oxidative polymerized method, vapor-phase polymerization method etc. Among the different polymerization methods chemically oxidative polymerization is most common and easy method for synthesis of PEDOT. Chemically oxidative polymerization can be achieved by using an oxidant such as ferric chloride ($FeCl_3$). The oxidative polymerization reaction is initiated by the oxidant which reacts with monomer-EDOT to generate radical cation. The radical cation reacts with another radical cation to form a dimeric dication. Subsequently the dimeric dication loses two protons, leading to the formation of dimers. Oxidizing agent reacts with dimer and the repetition of these steps lead to formation of PEDOT [116]. The oxidative polymerization of EDOT monomer to PEDOT is shown in Fig. 1.12.

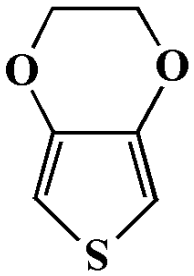

Figure 1.11: Chemical structure of 3,4-ethylenedioxythiophene (EDOT).

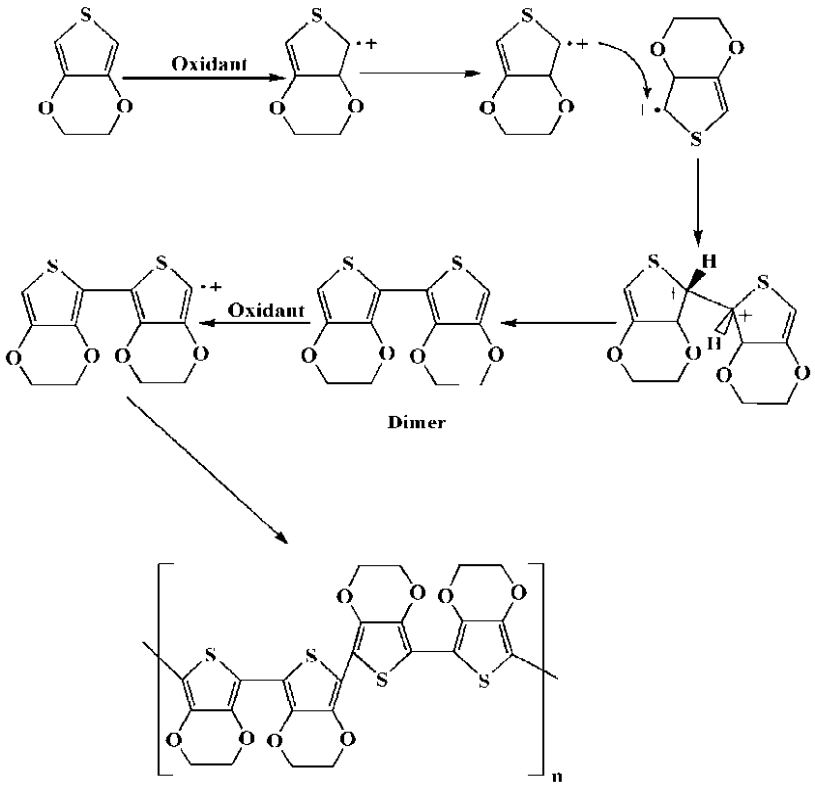

Figure 1.12: Chemically oxidative polymerization of EDOT into PEDOT.

Oxidative polymerization of EDOT can also be achieved by using iron (III) p-toluenesulfonate ($Fe(OTs)_3$) as oxidizing agent. The resultant black PEDOT can be converted into conductive polycation by oxidative doping [117]. Among the different synthesized conducting polymers PEDOT has unique building block for the design of different π-conjugated systems with enhanced electronic and optical properties [118]. PEDOT is also beneficial in energy storage devices such as supercapacitors due to its high specific capacitance, fast charge-discharge kinetics, tunable morphology and fast doping-dedoping process [119, 120]. Numerous research groups have followed different synthesis techniques to synthesize PEDOT nanostructures with a view to improve the physical and chemical properties. Some of the most promising applications of PEDOT nanostructures are in light-emitting diode, field effect transistors, electrochromic windows, sensor etc. [121-123].

1.7 Scope of the thesis and statement of the thesis problem

A quest at the forefront of modern technology involves the development of new materials with enhanced properties. Compared to inorganic materials organic

materials offer unique versatility in their physical and electronic properties, which can be tuned at molecular level through the chemical modification of the materials. The studies of conducting polymer systems have generated new scientific concepts for technological and biomedical applications. Some of the potential technological applications of conducting polymers in different solid state devices are organic light emitting diodes [124], field effect transistors [125], solar cells [126], molecular electronics [127], supercapacitors [128] and electrochromic devices [129] etc. However, in order to estimate the full potential demands of these materials, a better understanding of the electrical properties of these nanostructures is crucial. The resistivity, magnetoresistance and dielectric permittivity are the important properties, which can provide deep insight into the charge transport mechanism and charge carrier trapping in these materials. The measurements of dc resistivity and AC conductivity are reliable tools to study the localized states near the band edges below the lowest unoccupied molecular orbital (LUMO) and above the highest occupied molecular orbital (HOMO) produced by the disorder that controls the charge transport properties. The study of magnetoresistance properties in these materials will throw light on the nature of charge carriers under the application of magnetic field [130]. Analysis of dielectric permittivity, impedance and modulus formalisms can give information about the charge carriers' polarization and relaxation dynamics under the application of alternating electric field.

Conducting polymer nanostructures have been growing in interest among the scientific community for their potential technological and bio-medical applications. However, in all of these applications, the performance of conducting polymer nanostructures is strongly dependent upon their properties such as morphology, conductivity, chemical composition etc. In order to realize the full potential of nanotechnology, functional nanomaterials like conducting polymer nanostructures must be synthesized with control over dimensions, orientation and properties. Molecular and supermolecular modification induced during the synthesis of conducting polymer nanostructures at a submicroscopic scale may result in significant enhancement in electrical, optical and thermal properties. They offer advantage in the tenability of the electronic properties of the materials by chemical modification to confer desired features. Although in the last few years there are tremendous developments in the field of conducting polymer nanostructures, both

from technological and fundamental point of view [131-134], still their transport mechanism is not fully understood. Among the different properties a thorough understanding of charge transport mechanism in conducting polymer nanostructures is important because many applications are based on the electrical behavior. The nanostructures based on conducting polymers exhibit superior physical and chemical properties than that of the bulk counterparts due to quantum mechanical effects including quantum confinement and finite size effects [135, 136]. Different factors such as the effective conjugation length, carrier mobility, inter-chain interaction, band gap and morphology, which are greatly influenced by the charge transport mechanism in conducting polymers. The electrical, optical, magnetic and thermal properties of conducting polymer nanostructures can be tuned by the doping processes. The variation of doping concentration is an effective tool to understand the charge transport mechanism, which is greatly influenced by the quantum size effect and the intrinsic disorder present in the low-dimensional structures. Conducting polymers are disordered materials having crystalline and amorphous regions. The disorder in conducting polymers can produce localized states within the band gap. If the magnitude of the disorder potential is large as compared to band width, then all states become localized and the material behaves as insulator [137]. The disorder in conducting polymers arises from the variations in the conjugation length, rotation and kinks in the polymer chains, van der Waals interaction with neighboring conjugated chains and the impurities present [138, 139]. To understand the charge transport behavior in such materials, it is important to consider the intra-chain and inter-chain transport in the polymer. The electronic states of conducting polymers can be tuned by doping. Doping generates charge carriers which are self trapped by the conjugated polymeric chains in the form of polarons or bipolarons. The conduction of charge carriers can take place by the thermal hopping between localized states at the cost of activation energy [140]. Changing dopants, dopant concentration, temperature, magnetic field and AC field are the valuable ways to understand the charge transport behavior in such disordered materials.

In view of the foregoing, we have chosen poly(3,4-ethylenedioxythiophene) as the parent material among the conducting polymers for the present thesis for its exceptional properties as compared to those of the other conducting polymers as discussed in section 1.3. From the perspective of a new generation opto-electronic technology based on organic semiconductors, a major objective is to achieve a deep

and detailed knowledge of the structure-property relationship in order to optimize the electronic and charge transport properties by tuning the shape of the nanostructures and dopant concentration. One of the key objectives of the present work is the detailed investigation of the influence of doping concentration on the structure, morphology and charge transport mechanism. The present work also focuses on the investigation of charge carriers polarization and relaxation dynamics processes under the application of alternating electric field.

In order to achieve the above-mentioned objectives and to gain an insight into the charge transport and relaxation dynamics in poly(3,4-ethylenedioxythiophene) nanostructures, the following investigations have been performed in the present thesis work:

1. Poly(3,4-ethylenedioxythiophene) nanoparticles, nanofibers and nanotubes have been synthesized by using dopants dodecylbenzene sulfonic acid (DBSA), sodium dodecyl sulfate (SDS) and camphorsulfonic acid (CSA), respectively. For every nanostructured systems, four sets of samples have been synthesized with systematically varying the dopant concentration.
2. High resolution transmission electron microscope (HRTEM) measurements were performed to confirm the shape, size and morphology of the synthesized nanostructures.
3. X-ray diffraction, Fourier transforms infrared spectroscopy (FTIR) and micro-Raman spectroscopy measurements were carried out for the structural and vibrational analyses.
4. Thermogravimetric analysis (TGA) measurements have been carried out for observing the thermal stability of the synthesized nanostructures.
5. DC resistivity, magnetoresistance and AC conductivity were studied to investigate the charge transport mechanism.
6. Dielectric permittivity, impedance and modulus formalisms analyses have been conducted to explore the charge carriers' polarization and relaxation dynamics in the nanostructured systems.

Chapter 2

Theoretical Aspects

This chapter deals with different theoretical models that have been used to analyze the experimental results. The chapter describes the theoretical models and mechanisms that explain the DC resistivity, magnetoresistance and AC conductivity of poly(3,4-ethylenedioxythiophene) nanoparticles, nanofibers and nanotubes. Dielectric spectroscopy and its different formalisms have also been discussed in this chapter. At the end of this chapter the thermal degradation mechanism has been briefly explained.

2.1 Charge transport in disordered conducting polymers

The electrical transport in metals and inorganic semiconductors is explained using the band theory of solids. In this framework, atoms are arranged in a crystalline lattice periodic potential and the interaction of atoms leads to the formation of delocalized bands separated by forbidden gap known as band-gap [141]. Compared to the inorganic semiconductors, in which the charge transport occurs through band transport, the charge transport in organic semiconductors takes place through hopping between the energy states in the energy gap. The electrical properties of conducting polymers are determined by the $2p_Z$ - orbitals, which overlap to form delocalized π bond. Electronic states in such conjugated systems can be changed by excitation which modifies the π-bond electron densities leading to modification of bond length and torsion angles between repeated units. The strong correlation between electronic and geometric structure is termed as electron-phonon coupling. Conducting polymers are heterogeneous systems composed of partially ordered crystalline regions separated by disordered amorphous regions. Charge carriers in the ordered regions are delocalized, while they are strongly localized in the amorphous regions. However, the morphology of conducting polymers in the amorphous region is very complex which consists of chains that are both twisted and bent forming a spaghetti-like structure [142]. The charge transport in such heterogeneous systems takes place through electron delocalization or hopping of the charge carriers. The

disorder-induced localization plays a pivotal role in determining the transport properties of conducting polymers. Common factors which generate the disorder in conducting polymers are partial crystallinity, inhomogeneous doping and synthesis processes [143-145]. The localization of charge carriers in conjugated conducting polymers arises due to defects and impurities which produce trap states in the energy gap [146]. In the last few decades there have been intensive research efforts to understanding the charge transport mechanism in such disordered systems. Different theoretical models have been proposed to explain the charge transport mechanism in such disordered systems, still the charge transport in such systems is not fully understood. Different theoretical models that have been used in the present thesis work to explain DC resistivity, magnetoresistance, AC conductivity, dielectric permittivity formalism, impedance formalism, modulus formalism are discussed in the following subsections.

2.1.1 DC resistivity

2.1.1.1 Variable range hopping (VRH) model

In disordered materials like conducting polymers the existence of localized states depends on the dimensionality of the system. However, at absolute zero temperature, these localized states do not carry current. At temperature above 0 K, the charge transport takes place through the localized states with the help of phonon which is termed as hopping conduction. In a disordered system, the atoms are distributed in random manner and the electrons associated with them have distribution of energies. In such system for hopping of charge carries from one localized site to another, a certain amount of energy is required and it is known as activation energy. Due to random arrangement of the atoms having different activation energy, the hopping distance also varies with temperature [147]. Different disordered materials including conducting polymers the charge transport is well described by Mott variable range hopping (Mott-VRH) model [148-152]. Mott and Davis pointed out that the hopping of charge carriers in disordered materials is not necessarily restricted to nearest-neighboring sites only. Mott considered that the density of states (DOS) near the Fermi energy (E_F) is constant or a slowly varying function of energy [153]. According to this model the variation of resistivity with temperature can be expressed as:

$$\rho = \rho_o exp\left(\frac{T_{Mott}}{T}\right)^{1/\gamma} \quad (2.1)$$

where ρ_o is the resistivity when $T \rightarrow \infty$, T_{Mott} is the characteristic Mott temperature i.e. the energy needed for charge carriers to hop from one localized site to another which depends on the electronic structure and the energy distribution of the localized states. The exponent $\gamma = (1+d)$, where $d = 1$, 2 and 3 for one-dimension (1D), two-dimension (2D) and three-dimension (3D), respectively. The characteristic Mott temperature for three dimensional VRH model is expressed as:

$$T_{Mott} = \frac{16}{[L_{loc}^3 k_B N(E_F)]} \quad (2.2)$$

where L_{loc} and k_B are the localization length and Boltzmann constant, respectively.

In the Mott VRH model, Mott didn't consider the Coulomb interaction between the hopping sites. Knotek and Pollak [154] observed the nearest-neighbor interaction between localized electrons at very low temperature which gives rise to a minimum in DOS near the Fermi level. According to Efros and Shklovskii (ES) [155] in a strongly localized regime, the long-range electron-electron (e-e) Coulomb interaction creates a soft gap in DOS at the Fermi level. The density of states shows power law dependence near the Fermi energy expressed as:

$$N(E) = N_o|E - E_F|^p \quad (2.3)$$

where the exponent $p = 1$ for 2D and $p = 2$ for 3D VRH mechanism. The ES theory predicts the variation of resistivity with temperature for all dimensions:

$$\rho = \rho_o exp\left(\frac{T_{ES}}{T}\right)^{1/2} \quad (2.4)$$

where T_{ES} is the characteristics ES temperature and it is expressed as:

$$T_{ES} = \frac{2.8e^2}{\varepsilon k_B L_{loc}^2} \quad (2.5)$$

where the dielectric constant $\varepsilon = \varepsilon_o + 4\pi e^2 N(E_F) L_{loc}^2$.

2.1.1.2 Fluctuation induced tunneling (FIT) model

In the fluctuation induced tunneling model, Sheng [156] assumed that the electrical conduction is taken place by tunneling between conducting regions separated by

small insulating regions. In general, disordered materials are characterized by large metallic regions separated by small insulating barriers, where the thermally activated voltage fluctuation across the insulating barriers plays pivotal role in determining the temperature and field dependence of the conductivity [157]. If the metallic islands are sufficiently large such that the electrostatic charging energy is smaller than k_BT for accessible temperatures, tunnelling can occur between metallic states of the same energy on different sides of the barrier without thermal excitation. The thickness and height of the tunneling barrier greatly influences on conductivity and degree of nonlinearity of tunneling current decreases with increasing temperature due to narrowing the barrier height. According to FIT model the temperature dependence of resistivity can be expressed by the relation [157]:

$$\rho = \rho_o exp\left(\frac{T_t}{T_s + T}\right) \tag{2.6}$$

where T_t is the temperature at which fluctuations in the voltage across the barrier become sufficiently large to make the electron energy higher than the barrier height and T_s is the temperature above which thermally activated over-barrier conductivity becomes possible. The ratio T_t/T_s determines the tunneling in the absence of voltage fluctuations. The values of T_1 and T_s can be calculated by using the expressions [158]:

$$T_1 = \frac{W_f A \varepsilon_o^2}{8\pi k_B} \tag{2.7}$$

and

$$T_s = \frac{2T_1}{\pi \chi W_f} \tag{2.8}$$

where $\chi = \sqrt{(2mV_o/h^2)}$ and $\varepsilon_o = 4V_o/eW_f$, with m and e are the electron mass and charge, respectively. V_o is the potential barrier height, W_f is the gap width and A is the cross-sectional area. For small metallic islands, the FIT model leads to the form:

$$\rho(T) \approx T^{-0.5} \tag{2.9}$$

which is similar to one-dimensional (1D) VRH.

2.1.1.3 Heterogeneous model

The heterogeneous nature of conduction in conducting polymers was first proposed by Park *et al.* [159] and further it was developed by Epstein *et al.* [160] and Travers *et al.* [161]. The crystallinity in polymers is different from that of low-molecular weight compounds where the polymer chains are aligned only in small crystallite regions of typical dimensions 10-50 nm [162]. According to this model the total resistance is dominated by disordered regions or inter-fibril contacts and it is expressed as [163]:

$$\rho(T) = \sum_i f_i \rho_i (T) \tag{2.10}$$

where $f_i = L_i A / L A_i$ is the geometric factor. Here L and A are the total effective length and cross-sectional area of the sample, L_i is the path length of material i with intrinsic resistivity ρ_i (T) and A_i is the effective cross-section area for conduction in each region.

For non-fibrillar polymers, a more complex model was proposed where the resistance depends on the morphology of the thin barrier rather than the total volume. When extended metallic regions are separated by thin barriers, the overall resistivity can be expressed as the summation of quasi-1D metallic conduction and fluctuation induced tunneling;

$$\rho(T) = f_1 \rho_m exp\left(-\frac{T_m}{T}\right) + f_2 \rho_t exp\left(\frac{T_t}{T + T_s}\right) \tag{2.11}$$

The tunneling conductivity increases with temperature whereas the metallic conductivity decreases. When the temperature coefficient of the conductivity changes sign from non-metallic to metallic, eq. (2.11) gives rise to a peak in conductivity at the crossover temperature. The fluctuation induced tunneling term can be replaced by the expression for tunneling between mesoscopic islands which is limited by their charging energies as [164]:

$$\rho(T) = f_1 \rho_m exp\left(-\frac{T_m}{T}\right) + f_2 \rho_o exp\left(\frac{T_o}{T}\right)^{1/2} \tag{2.12}$$

Equation (2.12) can be used when the conduction through barrier region is by quasi-1D VRH.

2.1.2 Metal-insulator (M-I) transition

The reduce activation energy (W) is a useful empirical parameter for sorting out the various regimes. Zabrodskii and Zeninova [165] have calculated the reduce activation energy (W) from the resistivity data by the following expression:

$$W = -T\left(\frac{d\ ln\rho(T)}{dT}\right) = -\frac{d\ ln\rho}{d\ lnT} \tag{2.13}$$

The slope of *W vs. T* plot gives the dimension of transport mechanism and the various regimes present in the studied material. If the magnitudes of *W vs. T* slopes are 0.50, 0.33 and 0.25 then it indicates the 1D, 2D and 3D VRH mechanism, respectively. The nature of slope in various regimes is as follows:

If *W* has a negative temperature coefficient, then the system is in the insulating regime.

If *W* is independent of temperature for a wide range of temperature, then the material is in the critical regime.

If *W* has a positive temperature coefficient, then the system is in metallic regime.

2.1.3 AC conductivity

2.1.3.1 Correlated barrier hopping (CBH) model

According to this model, relaxation of charge carriers occurs by hopping over the barrier height (W_b), which is correlated with the intersite separation as a result of columbic interaction between the charge carrier and the charged – defect centers. Pike [166] proposed that electron transfer is taken place by the thermal activation over the barrier between two sites, each having a columbic potential associated with it. According to this model the hopping of charge carriers between two defect sites (D^+ and D^-) takes place over a potential barrier separating them, rather than tunneling through the barrier. The potential barrier (W_b) over which carriers must hop is the random variable and the variations in W_b arises due to variations in the hopping distance R_ω separating two hopping sites. The columbic interaction between two neighbouring sites lowers the binding energy W_M and the barrier height W_b can be related by the expression:

$$W_M - W_b = \frac{4ne^2}{\pi\varepsilon\varepsilon_o R_\omega} \tag{2.14}$$

where n is the number of charge carriers involved in the hopping process, e is the electronic charge, ε and ε_o are the dielectric constants of the material and in free space, respectively.

According to CBH model, the AC conductivity is expressed as [167]:

$$\sigma_{ac}(\omega) = \frac{n\pi^3}{24} N^2 \varepsilon\varepsilon_o \omega R_\omega^6 \tag{2.15}$$

where $N = k_B T N(E_F)$ the density of pair of sites. The hopping distance R_ω at a particular angular frequency ω and temperature (T) is given by:

$$R_\omega = \frac{e^2}{\pi\varepsilon\varepsilon_o} \frac{1}{W_M + k_B T ln(\omega\tau_c)} \tag{2.16}$$

and, the frequency exponent according to CBH model is expressed as:

$$s = 1 - \frac{6\, k_B T}{[W_M + k_B T ln(\omega\tau_c)]} \tag{2.17}$$

The frequency exponent s decreases with increasing temperature and it tends to unity when $T \rightarrow 0$K.

2.1.3.2 Jonscher's power law

The electrical conductivity as a function of frequency of disordered materials like ion conducting glasses, amorphous semiconductors, highly defective crystal and conducting polymers etc. can be described as frequency independent (DC conductivity) and a strongly frequency dependent component [168-170]. In general, the AC conductivity decreases with increasing frequency in the case of band conduction, whereas it increases with increasing frequency in the case of hopping conduction. At low frequencies, one observes a constant frequency independent conductivity and at higher frequencies, the conductivity becomes strongly frequency dependent. The generality of such behavior of frequency dependent conductivity is suitably described by the Jonscher's universal power law [171]:

$$\sigma_{tot}(\omega) = \sigma_{dc} + A\omega^s \tag{2.18}$$

where σ_{dc} is the DC conductivity of the material, A is the dispersion parameter and $0 < s < 1$ the dimensionless frequency exponent.

2.1.3.3 Scaling of AC conductivity

The charge carrier dynamics in disordered materials has been the subject of intense scientific interest for the past several years. The frequency dependence AC conductivity is the direct evidence of the charge carrier dynamic process in solids. Nearly four decades ago, an empirical relation was introduced by Barton [172], Nakajima [173] and Namikawa [174], known as BNN relation. This expression correlates the electrical conductivity to the dielectric strength expressed as:

$$\sigma_{dc} = p\varepsilon_o \Delta\varepsilon\omega_c \tag{2.19}$$

Where p is a numerical constant almost equal to 1, $\Delta\varepsilon=\varepsilon(0)-\varepsilon_\infty$ is the dielectric loss strength and ω_c is the characteristic crossover frequency. According to BNN the master curve can be represented as:

$$\frac{\sigma_{tot}(\omega)}{\sigma_{dc}} = F\left(\frac{c\omega}{\omega_c}\right) \tag{2.20}$$

where F is a temperature independent function, c depends on the charge carrier concentration and temperature. Sidebotton [175] proposed scaling law considering the dielectric strength as:

$$\frac{\sigma_{tot}(\omega)}{\sigma_{dc}} = F\left(\frac{\varepsilon_o \Delta\varepsilon\omega}{\sigma_{dc}}\right) \tag{2.21}$$

Later Summerfield [176] considering the extended pair approximation model, the scaling law proposed as:

$$\frac{\sigma_{tot}(\omega)}{\sigma_{dc}} = F\left(\frac{p\omega}{\sigma_{dc}T}\right) \tag{2.22}$$

where p depends on charge carrier concentration only. Within the hopping transport model according to Monte Carlo calculations [177], the scaling relation represented by eq. (2.22) is valid at sufficiently law temperature. In most of the disordered materials including conducting polymers the following scaling behavior has been observed [178, 179]:

$$\frac{\sigma_{tot}(\omega)}{\sigma_{dc}} = 1 + \left(\frac{\omega}{\omega_c}\right)^s \tag{2.23}$$

The scaling behavior of AC conductivity of the present thesis work is described by relation (2.23).

2.1.4 Magnetoresistance (MR)

The intrinsic magnetoresistance (MR) is defined as: $MR = \big(\rho(B) - \rho(0)\big)/\rho(0)$, where $\rho(0)$ is the resistance without magnetic field and ρ(B) is the resistance under magnetic field *B*. Magnetoresistance is the change in electrical resistance of the material in response to an external applied magnetic field and gives information about the dynamics of charge carriers. In conducting polymers both positive and negative MR have been observed. Generally, the MR of disordered localized systems in the VRH regime can be described by using quantum interference model (also orbital magnetoconductivity theory) and wave-function shrinkage model [180]. In the present work the observed MR has been explained using wave-function shrinkage and quantum interference model.

2.1.4.1 Wave-function shrinkage model

This theory considers the contraction of electronic wave-function under the application of magnetic field, which results the hopping probability reduction between two sites causing a positive MR. The optimum hopping probability parameter ξ_C (B) in terms of resistance ratio $r_{wave} = \rho(B,T)/\rho(0,T)$ under magnetic field is described as [181]:

$$r_{wave} = exp\left[\xi_c(0)\left\{\frac{\xi_c(B)}{\xi_c(0)} - 1\right\}\right] \tag{2.24}$$

where $\xi_c(0) = (T_{Mott}/T)^{1/4}$for the 3-D Mott VRH system [182]. ξ_C(B)/ξ_C(0) is the normalized hopping probability parameter. *B* is the magnetic field, P_C is the fitting parameter and for 3-D Mott VRH system, it is expressed as [183]:

$$P_c = {6\hbar}/{[eL_{loc}^2 (T_{Mott}/T)^{1/4}]} \tag{2.25}$$

where e is electron charge and $\hbar$ is the reduced Planck's constant. In the low magnetic field limit, eq. (2.24) can be simplified to as [184]:

$$\frac{\rho(B,T)}{\rho(0,T)} \approx 1 + t_2 \frac{B^2}{P_c^2}\left(\frac{T_{Mott}}{T}\right)^{1/4} \tag{2.26}$$

and MR is defined as:

$$MR = \frac{\rho(B,T) - \rho(0,T)}{\rho(0,T)}$$

$$\approx t_2 \frac{B^2}{P_c^2}\left(\frac{T_{Mott}}{T}\right)^{1/4}$$

$$= t_2 \frac{e^2 L_{loc}^4}{36\hbar^2}\left(\frac{T_{Mott}}{T}\right)^{3/4} B^2 \tag{2.27}$$

where numerical constant t_2 = 5/2016.

2.1.4.2 Quantum interference model

The quantum interference model was proposed by Nguyen, Spivak and Shklovskii (NSS) [185], to analyze the negative MR. NSS considered the effect of interference among all possible hopping paths. These hopping paths include the scattering sequence of tunneling electrons by the impurities located within the cigar-shaped domain length R_{hop} (hooping length) and width $(R_{hop}\ L_{loc})^{1/2}$ between the hopping sites [186]. The overall conductivity is proportional to the sum of all the possible hopping paths between two localized sites. As a result of forward interference under magnetic field, a decreased resistivity is observed i.e. negative MR [181]. The resistance ratio $r_{forward} = \rho(B)/\rho(0)$ caused by forward interference effects is expressed as:

$$r_{forward} \approx {}^{1}/_{[1 + C_{sat}(B/B_{sat})/(1 + B/B_{sat})]} \tag{2.28}$$

where the parameter C_{sat} is the saturation constant and temperature independent. The fitting B_{sat} is the effective saturation magnetic field. From eq. (2.28), it is observed that $r_{forward}$ saturates at high magnetic fields to a value of (1 + C_{sat}) and at intermediate fields, it becomes linear dependence on B. In case of Mott-VRH transport mechanism, B_{sat} can be expressed as [186]:

$$B_{sat} \approx 0.7\left(\frac{8}{3}\right)^{3/2}\left(\frac{1}{L_{loc}^2}\right)\left(\frac{h}{e}\right)\left(\frac{T}{T_{Mott}}\right)^{3/8} \tag{2.29}$$

where h is Planck's constant. When B/B_{sat} and C_{sat} are small eq. (2.28) takes the form:

$$r_{forward} \approx 1 - C_{sat}\left(\frac{B}{B_{sat}}\right) \tag{2.30}$$

Now the negative MR can be expressed as [186]:

$$MR = \frac{\rho(B,T) - \rho(0,T)}{\rho(0,T)} \approx -C_{sat}(B/B_{sat})$$

$$= -C_{sat}\frac{B}{0.7\left(\frac{8}{3}\right)^{3/2}\left(\frac{1}{L_{loc}^2}\right)\left(\frac{h}{e}\right)\left(\frac{T}{T_{Mott}}\right)^{3/8}} \tag{2.31}$$

2.1.5 Dielectric relaxation

Dielectric relaxation in solids is one of the most extensively studied research topic in physics that can provide information about the different charge carriers' dynamics present in the material. When an alternating electric field is applied to a dielectric material, the material is polarized by different polarization mechanisms namely, electronic polarization, atomic polarization, orientation polarization, ionic polarization and space charge polarization. The permittivity is a measure of polarization which shows frequency dependent behavior. Dielectric spectroscopy is a non-destructive technique that can measure permittivity and conductivity as a function of frequency and gives information about polarization and relaxation dynamics of charge carriers. Dielectric information may be formulated in a number of equivalent ways and it is important to use the most appropriate form of presentation to match the particular requirement [187]. The dielectric properties can be explained by using complex parameters like complex dielectric permittivity (ε^*), complex impedance (Z^*), complex electric modulus (M^*) etc. and are discussed following subsections.

2.1.5.1 Complex dielectric permittivity formalism

The relaxation behavior of a dielectric material under the application of an alternating electric field is expressed as [188]:

$$\varepsilon^*(\omega) = \varepsilon^{'}(\omega) - i\varepsilon^{''}(\omega) \tag{2.32}$$

where $\varepsilon'(\omega)$ and $\varepsilon''(\omega)$ are the real and imaginary parts of the complex permittivity $\varepsilon^*(\omega)$, respectively. The real part $\varepsilon'(\omega)$ represents the energy storage and the imaginary part $\varepsilon''(\omega)$ represents the energy loss in each circle of the applied ac electric field. The decay function of dielectric relaxation after removal of applied electric field is expressed as:

$$\Phi(t) = \frac{P(t)}{P(0)} \tag{2.33}$$

where P is a polarization vector. The complex dielectric permittivity $\varepsilon^*(\omega)$ is related with the relaxation function according to the relation [189, 190]:

$$\frac{\varepsilon^*(\omega) - \varepsilon_\infty}{\Delta\varepsilon} = \hat{L}\left[-\frac{d}{dt}\Phi(t)\right] \tag{2.34}$$

where ε_∞ is the dielectric permittivity when ($\omega \rightarrow \infty$) and $\Delta\varepsilon = (\varepsilon_s - \varepsilon_\infty)$ is the dielectric strength. $\hat{L}$ is the Laplace transform operator and it is defined as for time-dependent function $f(t)$ as

$$\hat{L}[f(t)] = \int_0^\infty e^{-i\omega t} f(t)dt \tag{2.35}$$

If

$$\Phi(t) = \exp\left(-\frac{t}{\tau_D}\right) \tag{2.36}$$

where τ_D is the characteristic dielectric relaxation time. Using eqs. (2.35 & 2.36) eq. (2.34) can be written as

$$\frac{\varepsilon^*(\omega) - \varepsilon_\infty}{\Delta\varepsilon} = \frac{1}{1 + i\omega\tau_D} \tag{2.37}$$

Equation (2.37) is known as Debye equation. Debye equation is valid only for materials having single relaxation mechanism. Later Havriliak-Negami (HN) modified Debye equation for materials having distribution of relaxation time and it is expressed as [191]:

$$\varepsilon^*(\omega) = \varepsilon_\infty + \frac{\Delta\varepsilon}{[1 + (i\omega\tau_{hn})^{1-\alpha_{hn}}]^{\beta_{hn}}} \quad (2.38)$$

where, τ_{hn} is the relaxation time and α_{hn} ($0 \leq \alpha_{hn} < 1$) and β_{hn} ($0 \leq \beta_{hn} \leq 1$) are the geometric shape parameters defining symmetrical and asymmetrical distribution. The parameters $\alpha_{hn} = 0$ and $\beta_{hn} = 1$ indicate the Debye-type relaxation and $\beta_{hn} = 1$ and $0 \leq \alpha_{hn} \leq 1$ indicate the Cole-Cole type relaxation. The Cole-Davidson model with an asymmetrical distribution of relaxation times follows for $\alpha_{hn} = 0$ and $0 \leq \beta_{hn} \leq 1$.

2.1.5.2 Complex impedance formalism

When an alternating electric field is applied to a system, the impedance of the system can be expressed as ratio of voltage to current in the time domain [192]:

$$V(t) = V_o exp(i\omega t) \quad (2.39)$$

$$I(t) = I_o \exp(i\omega t - \Phi) \quad (2.40)$$

Impedance is a complex quantity having both magnitude $|Z|$ and phase angle (Φ) and it is expressed as:

$$Z^*(\omega) = |Z| \exp(-i\Phi) \quad (2.41)$$

$$Z^*(\omega) = |Z|cos\Phi - i|Z|sin\Phi \quad (2.42)$$

i.e.

$$Z^*(\omega) = Z' - iZ'' \quad (2.43)$$

where $Z' = |Z|\cos\Phi$ and $Z'' = |Z|\sin\Phi$ are the real and imaginary parts of complex impedance, respectively. The equivalent model proposed by Cole-Cole function, is given by [193]:

$$Z^*(\omega) = R_\infty + \frac{R_o - R_\infty}{[1 + (i\omega\tau_m)^{1-\alpha}]} \quad (2.44)$$

where R_∞ and R_0 are the resistance when ($\omega \rightarrow \infty$) and ($\omega \rightarrow 0$), respectively. The parameter $\tau_m = RC$ is the relaxation time and $0 \leq \alpha < 1$ determines the distribution of relaxation time and for ideal Debye relaxation $\alpha = 0$. The real and imaginary parts of complex impedance are as follows:

$$Z^{'} = R_{\infty}\frac{(R_0 - R_{\infty})\left\{1 + \frac{(\omega\tau_m)^{1-\alpha}\cos(1-\alpha)\,\pi}{2}\right\}}{1 + (\omega\tau_m)^{2(1-\alpha)} + 2(\omega\tau_m)^{1-\alpha}cos\{(1-\alpha)\pi/2\}} \tag{2.45}$$

and

$$Z^{''} = \frac{-(R_0 - R_{\infty})(\omega\tau_m)^{1-\alpha}\sin\frac{(1-\alpha)\pi}{2}}{1 + (\omega\tau_m)^{2(1-\alpha)} + 2(\omega\tau_m)^{1-\alpha}cos\{(1-\alpha)\pi/2\}} \tag{2.46}$$

2.1.5.3 Complex modulus formalism

The complex electric modulus measures the conductivity relaxation dynamics of the charge carriers and it is defined as the reciprocal of the complex permittivity ε^* introduced by Macedo [194] as:

$$M^*(\omega) = \frac{1}{\varepsilon^*(\omega)} = \frac{1}{\varepsilon^{'} - i\varepsilon^{''}} = \frac{\varepsilon^{'}}{\varepsilon^{'\,2} + \varepsilon^{''\,2}} + i\frac{\varepsilon^{''}}{\varepsilon^{'\,2} + \varepsilon^{''\,2}}$$

$$= M^{'} + iM^{''} \tag{2.47}$$

where M' and M'' are the real and imaginary parts of complex modulus, respectively. Modulus can be characterized by exponential decay function which is defined by the empirical Kohlrausch-Williams-Watts (KWW) function [195]:

$$\Phi(t) = exp\left(-\left(\frac{t}{\tau_{max}}\right)^{\beta_{KWW}}\right) \tag{2.48}$$

Where τ_{max} is the relaxation time, $0 \leq \beta_{KWW} \leq 1$ is the Kohlrausch parameter. The decay function Φ(t) is related to the complex modulus in the frequency domain by the relation:

$$M^*(\omega) = M_s\left[1 - \int_0^{\infty}\exp(-i\omega t)\left(-\frac{d\Phi(t)}{dt}\right)dt\right] \tag{2.49}$$

Bergman [196] modified the KWW function for fitting approach in the frequency domain and the imaginary part of electric modulus was approximated as:

$$M^{''}(\omega) = \frac{M^{''}_{max}}{\left[(1-\beta_{KWW}) + \frac{\beta_{KWW}}{1+\beta_{KWW}}\left\{\beta_{KWW}\left(\frac{\omega_{max}}{\omega}\right) + \left(\frac{\omega}{\omega_{max}}\right)^{\beta_{KWW}}\right\}\right]} \tag{2.50}$$

2.2 Thermal degradation kinetics and activation energy

The thermal degradation reaction of a solid can be expressed as: $B_{solid} \rightarrow C_{solid} + D_{gas}$, where B_{solid} is the initial material, C_{solid} and D_{gas} are the different product during the degradation of B_{solid}. The reaction kinetics in TGA studies can be understood from the variation of degree of conversion (X) with time or temperature and it is calculated as [197]:

$$X = \frac{W_0 - W_t}{W_0 - W_f} \tag{2.51}$$

where W_0, W_t and W_f are the mass of the sample at the beginning, at time t and at the end of the mass loss reaction, respectively. For a typical TGA measurement the rate of conversion, dX/dt can be expressed as:

$$\frac{dX}{dt} = k(T)f(X) \tag{2.52}$$

where k(T) and f(X) are the functions of temperature and conversion, respectively. The temperature dependent rate constant k(T) follows the Arrhenius relation:

$$k(T) = A\ exp\left(-\frac{E_d}{RT}\right) \tag{2.53}$$

where E_d is the activation energy of thermal degradation (J/mol), A the pre-exponential factor (s^{-1}) and R the gas constant (8.314 J/mol K). Combining eqs. (2.52) and (2.53), we get,

$$\frac{dX}{dt} = A\ exp\left(-\frac{E_d}{RT}\right)\ f(X) \tag{2.54}$$

For a dynamic degradation process, the Eq. (2.54) can be expressed as:

$$\frac{dX}{dT} = \frac{A}{\beta} exp\left(-\frac{E_d}{RT}\right) f(X) \tag{2.55}$$

where β=dT/dt is the heating rate. Equations (2.54) and (2.55) represent the fundamental expression of analytical methods to evaluate the degradation kinetics parameters from TGA data. There are different methods such as Kissinger-Akahira-Sunose (KAS) method [198, 199], Friedman method [200], Flynn-Wall-Ozawa method [201, 202] to find out the degradation kinetics and activation energy. Kissinger-Akahira-Sunose (KAS) method involves obtaining the temperature values (T_{max}) which occurs at the maximum rate at which d(dX/dt)/dt is zero. The slope of

the $\log(\beta/T_{max}^2)$ *vs.* $1000/T_{max}$ gives the value of activation energy. Friedman method is a differential iso-conversional method and in this method activation energy is calculated from the slope of log (βdX/dT) *vs.* 1000/*T* plot for a constant *X* value. Flynn-Wall-Ozawa method is an iso-conversional integral method and here activation energy is calculated from the slope of logβ *vs.* 1000/*T* plot. The major advantage of Flynn-Wall-Ozawa method is that it does not require any assumptions regarding the nature of kinetic equation other than the Arrhenius type temperature dependence. In the present thesis, the Flynn-Wall-Ozawa method has been used to calculate the activation energy of thermal degradation of the PEDOT nanostructures systems.

Flynn-Wall-Ozawa method is an iso-conversional "model-free" method which assumes that the conversion function f(*X*) does not change with changing heating rate β for all values of *X*. For different heating rates β, it measures the temperatures corresponding to fixed values of *X*. The plotting of logβ *vs.* 1000/*T* should give straight line and the slope of the straight line is directly proportional to the (- E_d/R). If activation energy varies with increase of degree of conversion *X*, it indicates that the degradation kinetics follows multistep reaction mechanism, whereas the same value of activation energy for different values of degree of conversion validates the presence of single-step degradation kinetics [203]. The conversion function *f*(X) depends on the particular decomposition mechanism. The simplest and most frequently used model for *f*(X) in the degradation kinetics is

$$f(X) = (1 - X)^n \tag{2.56}$$

where *n* is the order of the reaction. Now combining eqs. (2.55) and (2.56), we have

$$\frac{dX}{(1-X)^n} = \frac{A}{\beta}\exp\left(-\frac{E_d}{RT}\right)dT \tag{2.57}$$

Flynn-Wall-Ozawa assumes that *A*, $(1\text{-}X)^n$ and E_d are independent of *T* while *A* and E_d are independent of degree of conversion, then eq. (2.57) can be integrated to the form:

$$\int_0^X \frac{dX}{(1-X)^n} = \frac{A}{\beta}\int_{T_0}^{T} exp\left(-\frac{E_d}{RT}\right)dT \tag{2.58}$$

where T_0 is the value of *T* at $t = t_0$. Generally, at low temperature the rate of reaction is very low so the next approximation is valid:

$$\int_{T_0}^{T} exp\left(-\frac{E_d}{RT}\right) dT = \int_{0}^{T} exp\left(-\frac{E_d}{RT}\right) dT \tag{2.59}$$

According to Doyle [204], the right hand side of eq. (2.59) can be expressed as a function of *P* as given below:

$$\frac{E_d}{R} P\left(\frac{E_d}{RT}\right) = \int_{0}^{T} exp\left(-\frac{E_d}{RT}\right) dT \tag{2.60}$$

According to Doyle [204], if E_d/RT is larger than 20, $P(\frac{E_d}{RT})$ can be approximated by the following formula:

$$\log P\left(\frac{E_d}{RT}\right) = -2.315 - 0.4567\frac{E_d}{RT} \tag{2.61}$$

For a given value of *X*, left hand side of eq. (2.61) is constant. Therefore, if the weight deceases to a given fraction at the temperature T_1 for heating rate of β_1, at T_2 for heating rate of β_2 and so on, the following equation can be obtained:

$$\frac{E_d}{\beta_1 R}\ P\left(\frac{E_d}{RT_1}\right) = \frac{E_d}{\beta_2 R}\ P\left(\frac{E_d}{RT_2}\right) = \cdots \tag{2.62}$$

From equations (2.61) and (2.62), we get,

$$-log\beta_1 - 0.4567\frac{E_d}{RT_1} = -log\beta_2 - 0.4567\frac{E_d}{RT_2} = \cdots \tag{2.63}$$

Equation (2.63) can be written as:

$$log\beta = -0.4567\frac{E_d}{RT} + constant \tag{2.64}$$

From eq. (2.64), it can be concluded that the plots of log β *vs.* 1000/*T* for a particular value of *X* must give a straight line and the activation energy of thermal degradation (E_d) can be calculated from the slope.

Chapter 3

Experimental Techniques

This chapter covers the extensive discussions on synthesis techniques and physico-chemical properties of parent materials that have been used to synthesis poly(3,4-ethylenedioxythiophene) nanoparticles, nanofibers and nanotubes. Characterization techniques used for structural, vibrational and thermal analyses have been briefly discussed. Lastly, DC resistivity, magnetoresistance and dielectric measurements set up have been discussed.

3.1 Parent materials

The monomer 3,4-ethylenedioxythiophene (EDOT) purchased from Sigma Aldrich Chemical Inc. (USA) was used for the synthesis of different poly(3,4-ethylenedioxythiophene) (PEDOT) nanostructures. Dodecylbenzene sulfonic acid (DBSA) and camphorsulfonic acid (CSA) were also procured from Sigma Aldrich Chemical Inc. (USA). Sodium dodecyl sulfate (SDS) was purchased from Merck (India). DBSA, CSA and SDS were used as surfactants and functional dopants for synthesis of the nanostructures. Ferric chloride ($FeCl_3$) was obtained from Merck and used as oxidant to initiate the polymerization of EDOT. Different organic solvents acetonitrile, n-hexane, methanol and acetone were received from Merck. All the purchased chemicals were analytical grade and used as received. The physical properties of the parent materials used for the synthesis of different PEDOT nanostructures in the present work are presented in Table 3.1.

Table 3.1: *Physical properties of different parent materials used for the synthesis of poly(3,4-ethylenedioxythiophene) nanoparticles, nanofibers and nanotubes.*

Physical properties of monomer (EDOT)						
Monomer	Chemical formula	Molecular weight (g/mol)	Melting point (°C)	Boiling point (°C)	Density at 25 °C (g/mL)	Redox Potential (V)
3,4-ethylenedioxy thiophene	$C_6H_6O_2S$	142.18	10.5	225	1.331	-0.6

Physical properties of oxidant					
Oxidant	Chemical formula	Molecular weight (g/mol)	Melting point (°C)	Boiling point (°C)	Density at 25 °C (g/mL)
Ferric chloride	$FeCl_3$	162.2	306	315	2.898

Physical properties of dopants					
Dopants	Molecular formula	Molecular weight (g/mol)	Melting point (°C)	Boiling point (°C)	Density at 25 °C (g/mL)
Dodecylbenzene sulfonic acid (DBSA)	$C_{18}H_{30}O_3S$	326.49	10	82	1.06
Sodium dodecyl sulfate (SDS)	$C_{12}H_{25}NaO_4S$	288.38	204-207	N/A	1.01
Camphorsulfonic acid (CSA)	$C_{10}H_{16}O_4S$	232.29	198	N/A	1.331

Physical properties of solvents

Solvents	Molecular formula	Molecular weight (g/mol)	Melting point (°C)	Boiling point (°C)	Density at 25 °C (g/mL)
Acetone	C_3H_6O	58.08	-95	56	0.7910
Methanol	CH_4O	32.04	-97.6	64.7	0.7918
Acetonitrile	C_2H_3N	41.05	-45	82	0.7860
n-hexane	C_6H_{14}	86.18	-96	68.5	0.6548

3.2 Synthesis of PEDOT nanostructures

3.2.1 Synthesis of PEDOT nanoparticles

The investigation of conducting polymer nanoparticles is still a developing area in nanoscience and nanotechnology. Different research groups synthesized poly(3,4-ethylenedioxythiophene) (PEDOT) nanoparticles by following different synthesis processes such as emulsion polymerization [205, 206] and by using micellar solutions surfactants [207]. Among the different synthesis techniques, the micelle soft-template also known as self assembly method is mostly used because of its ease of synthesis, large-scale production ability and environmentally benign nature. In this method, the size, shape and morphology of the nanostructures can be tuned by controlling the surfactant concentration or surfactant to monomer molar ratio. There are different types of surfactant such as anionic (e.g., Dodecylbenzene sulfonic acid), cationic (e.g., cetyltrimethylammonium bromide) or non-ionic (e.g., poly (ethylene glycol) mono-p-nonylphenyl ether (Opi-10)) which can be used as soft templates for the synthesis of PEDOT nanoparticles. In the present thesis work, we synthesized of PEDOT nanoparticles using dodecylbenzene sulfonic acid (DBSA) as surfactant. The synthesis block diagram of PEDOT nanoparticles is shown in Fig. 3.1.

In a typical synthesis process, aqueous micellar dispersion was prepared by introducing 3 mM DBSA in 100 ml DDW in a 250 ml beaker and kept under stirring. 0.01M EDOT monomer was added to the DBSA micellar solution and solubilized by stirring for 1 h. 0.01M of oxidant $FeCl_3$ was dissolved in 100 ml

DDW and syringed quickly to the monomer-DBSA micellar solution. Finally, it was kept under stirring at room temperature for 20 h. The precipitate were collected by filtration using Whatman filter paper and washed with DDW, methanol and acetone successively, to remove the oligomers and other impurities present in the precipitate and then dried under vacuum at 40^{o}C for 24 h. Four sets of samples were synthesized by keeping DBSA concentration as 0.003M, 0.01M, 0.1M and 1M, respectively.

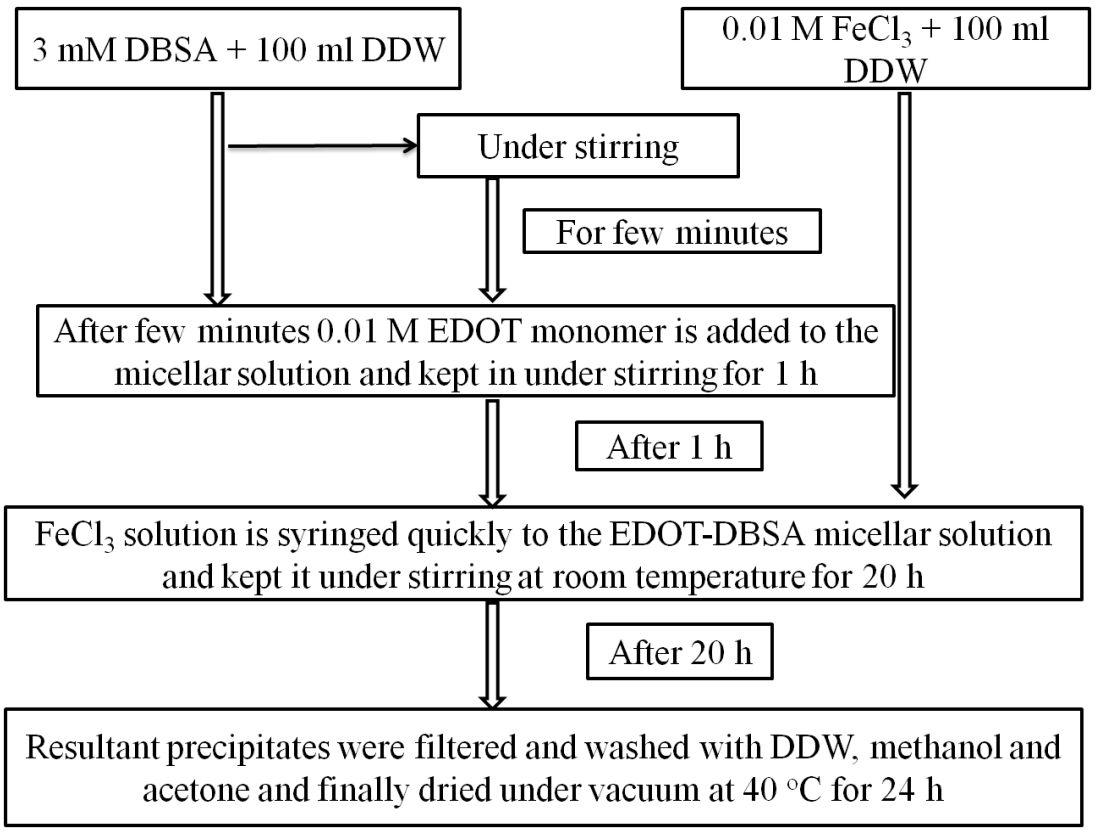

Figure 3.1: Block diagram of synthesis of PEDOT nanoparticles

3.2.2 Synthesis of PEDOT nanofibers

The conducting polymer nanofibers have received tremendous scientific interest for the fabrication of number of electronic nanodevices due to required flexibility and significant surface area. Different research groups synthesized poly(3,4-ethylenedioxythiophene) (PEDOT) nanofibers by following chemical, electrochemical and electrospinning methods. Zhang *et al.* [208] reported the synthesis of PEDOT nanofibers using V_2O_5 seeds. Duvail *et al.* [209] synthesized PEDOT nanofibers following electrosynthesis in aqueous solution. Poly(3,4-

ethylenedioxythiophene) nanofibers were synthesized by Laforgue *et al.* [210] following electrospinning method. Han *et al.* [211] have synthesized poly(3,4-ethylenedioxythiophene) nanofibers following self-assembly method using SDS as surfactant. In the present thesis, we have synthesized poly(3,4-ethylenedioxythiophene) nanofibers following soft template or self assembly method using SDS as surfactant. Synthesis block diagram of poly(3,4-ethylenedioxythiophene) nanofibers is shown in Fig. 3.2.

For the synthesis of PEDOT nanofibers, initially 30 mM SDS was dissolved in 50 ml DDW. 30 mM $FeCl_3$ aqueous solution was added to the SDS solution and kept under stirring at 50^{o}C for a few minutes. 10 mM EDOT was added slowly to the above solution with continuous stirring at 50^{o}C. The polymerization was allowed to proceed for 6 h. During polymerization, the colour of the reaction vessel changed from yellow to green and finally to dark blue. After 6 h, the dark blue precipitate was filtered and washed with DDW, methanol and acetone. Finally, the powdered samples were dried at room temperature in vacuum chamber for characterization. Four samples were synthesized by varying SDS concentration as 0.03M, 0.1M, 0.5M and 1M.

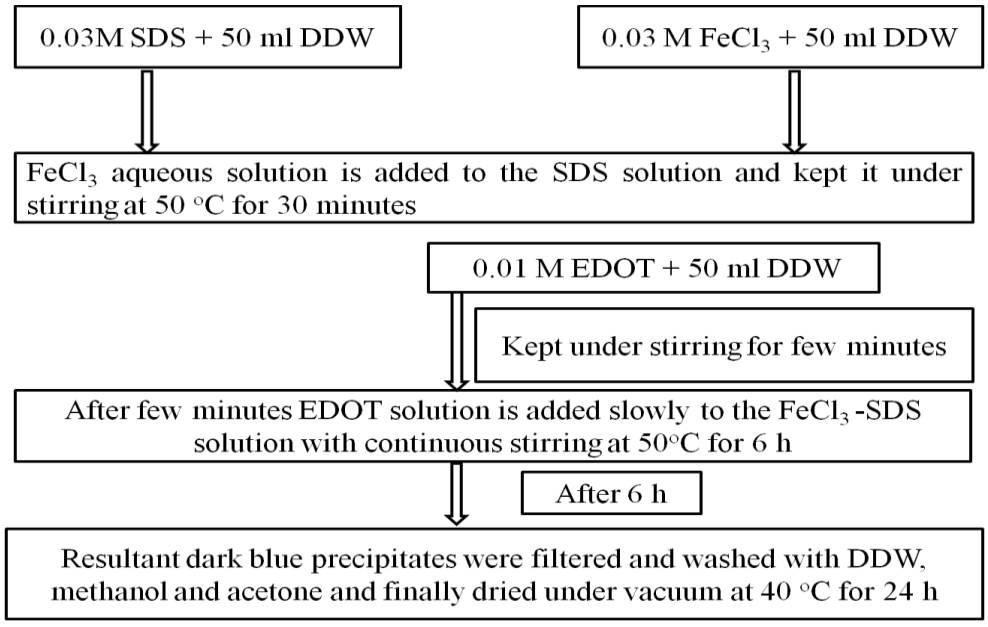

Figure 3.2: Block diagram of synthesis of PEDOT nanofibers

3.2.3 Synthesis of PEDOT nanotubes

The poly(3,4-ethylenedioxythiophene) nanotubes were synthesized by different research groups following both electrochemical and chemical methods using hard and soft template. Zhang *et al*. [212] synthesized poly(3,4-ethylenedioxythiophene) nanotubes following reverse microemulsion polymerization method using bis(2-ethylhexyl) sulfosuccinate (AOT) cylindrical micelles as the templates and $FeCl_3$ as oxidant. Cho *et al.* [213, 214] reported the electrochemical template synthesis of PEDOT nanotubes in the pores of the anodic aluminium oxide (AAO) film and track-etched porous polycarbonate (PC) membrane on the ITO/glass substrate. Dobbelin *et al.* [215] synthesized PEDOT nanotubes on conductive ZnO substrates. Wang *et al.* [216] had reported the synthesis of PEDOT nanotubes using n-hexane and acetonitrile as organic solvents.

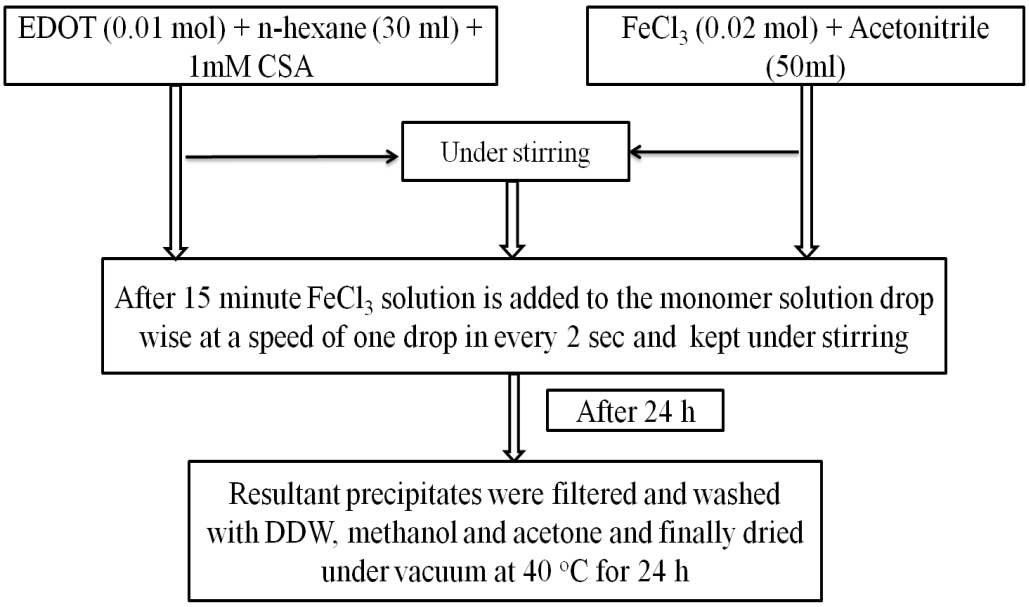

Figure 3.3: Block diagram of synthesis of PEDOT nanotubes

In the present thesis work PEDOT nanotubes have been synthesized by using n-hexane, acetonitrile as organic solvents and camphorsulfonic acid (CSA) as dopants. Here CSA acts as surfactant as well as functional dopants. The synthesis block diagram of PEDOT nanotubes is presented in Fig. 3.3. In the synthesis procedure 0.02 mol $FeCl_3$ was dissolved in 50 ml acetonitrile under magnetic stirring and named it as solution A. 0.01 mol of monomer EDOT and 0.001 M

camphorsulfonic acid were dissolved in 30 ml n-hexane under magnetic stirring and coded it as solution B. Solution A was poured into the solution B drop-wise and the mixture was kept under stirring at room temperature for 24 h. After 24 h the product was collected from the polymerization media by centrifugation and washed with DDW, methanol and acetone, then separated by centrifugation for 5 min at 4000 rpm and finally dried in vacuum at 70^{o}C. Four sets of samples were synthesized by varying camphorsulfonic acid concentration as 0.001M, 0.01M, 0.1M and 1M, respectively.

3.3 Characterization techniques

The various characterization techniques that have been employed to investigate the structural, vibrational, thermal, transport and dielectric properties are discussed in the following subsections.

3.3.1 High resolution transmission electron microscopy (HRTEM)

High resolution transmission electron microscopy (HRTEM) is a powerful tool, which is used to understand the shape, size and distribution of the nanostructures at the nanometer level. TEM operates on the same principle as the light microscope but uses electrons instead of light. It uses electrons as "light sources" and due to their lower value of wavelength, it is possible to get a resolution of thousand times better than a light microscope. The high energetic electron beam is emitted by an electron gun, commonly fitted with a tungsten filament cathode as the electron gun. The emitted electron beam is allowed to pass through a vacuum column and electromagnetic lenses are used to focus the electrons into a very thin beam. Depending upon the density of the materials present, some electrons are scattered and disappeared from the beam. When the electron beam emerges from the specimen, it carries information about the structure of the specimen that is magnified by the objective lens system of the microscope. The spatial variation in this information (the "image") is viewed by projecting the magnified electron image onto a fluorescent viewing screen coated with a phosphor or scintillator material such as zinc sulfide. The image can be photographically recorded by exposing a photographic plate directly to the electron beam, or a high-resolution phosphor may

be coupled by means of a lens optical system or a fiber optic light-guide to the sensor of a CCD (charge-coupled device) camera. The image detected by the CCD may be displayed on a monitor or computer.

In the present thesis the HRTEM images were recorded by using JEOL JEM-2100 transmission electron microscope and shown in Fig. 3.4. The micrographs were taken at 200 kV accelerating voltage and at different magnification according to the requirement. For the HRTEM measurements, the powdered samples were dispersed by using an ultrasonicator and a drop of PEDOT suspension was placed on a carbon coated copper grid and dried in an oven.

Figure 3.4: High resolution transmission electron microscope (JEOL, model JEM-2100).

3.3.2 X-ray diffraction (XRD)

X-ray diffraction is a nondestructive analytical technique used for the identification and characterization of crystalline, semicrystalline and amorphous materials based on their diffraction pattern. It provides information about the structures, phases, preferred crystal orientation, and other structural parameters, such as average grain size, crystallinity, strain and crystal defects. The X-ray diffraction pattern gives the fingerprint of periodic arrangement of atoms or molecules of a given material. X-ray diffraction peaks are produced by the constructive interference of monochromatic X-

rays scattered at specific angles from each set of lattice planes in a sample. A cathode ray tube is used to generate X-rays, which is filtered to produce monochromatic radiation and finally collimated and directed towards the sample. The incident X-rays on the target material produces constructive interference when it satisfy the Bragg's law ($n\lambda=2d\sin\theta$) condition. This law correlates the wavelength of incident X-rays with incident angle and lattice spacing. The intensities of the peaks are determined by the distribution of atoms within the lattice and the diffraction pattern is the fingerprint of periodic arrangement of atoms in a given material. Conducting polymers is a semicrystalline material composed of crystalline and amorphous region. Their crystallinity is attributed to chain folding or to the formation of single or double helices, for at least part of their chain length [217]. The X-ray diffraction is a suitable tool to determine the degree of crystallinity, crystallite size and polymer chains alignment of such semicrystalline polymeric materials.

In the present work, the X-ray diffraction pattern of different PEDOT nanostructures have been obtained by using Rigaku X-ray diffractometer (model MINIFLEX 200) with CuK_α radiation (λ = 1.5406 Å) shown in Fig. 3.5. The angular range spread over the region between 5^0 and 40^0 in 2θ, in steps of 0.05^0. The X-ray diffraction patterns have been used to determine the crystallite size (*L*) and the degree of crystallinity (*K*).

Figure 3.5: X-ray diffraction measurement unit (Rigaku, MiniFlex).

3.3.2.1 Calculation of crystallite size (L)

In the present work, the crystallite sizes (L) of PEDOT nanostructures have been calculated using Debye Scherrer equation [218].

$$\beta = \frac{0.89\,\lambda}{L cos\theta} \tag{3.1}$$

where λ is the X-ray wavelength (λ = 1.5406 Å), L is the average crystallite size, β is the full-width at half-maximum (FWHM) and θ is Bragg diffraction angle in degree.

3.3.2.2 Calculation of degree of crystallinity (K)

The local range of ordering in polymer chains of polymer samples are generally described in terms of the degree of crystallinity (K). The degree of crystallinity can provide reasonably a good estimation of the amount of crystalline phase present in a polymer sample. A typical X-ray diffractogram for a polymeric material consists of a broad amorphous hump superimposed with some sharp peaks as shown in the figure 3.6 (a). The total area under the diffractogram is the sum of the crystalline peaks and broad amorphous hump.

Consider a typical X-ray diffractogram having two crystalline peaks with areas A_1 and A_2 superimposed on a broad amorphous hump with an area A_3 as shown in figure 3.6 (b), then the degree of crystallinity (K) of the polymer will be

$$K = \frac{\alpha_c(A_1 + A_2)}{\alpha_c(A_1 + A_2) + \alpha_a A_3} \tag{3.2}$$

where α_c and α_a are proportionality constant for the crystalline and amorphous phases, respectively. Assuming $\alpha_c = \alpha_a$ for reasonable accuracy in polymers, the equation (3.2) for the degree (percentage) of crystallinity may be written as

$$K = \frac{A_1 + A_2}{A_1 + A_2 + A_3} \times 100\% = \frac{A}{A'} \times 100\% \tag{3.3}$$

where A is the sum of the areas of all the crystalline peaks in the diffractogram and A' is the total area under the diffractogram. In the present work, the area has been calculated by dividing the X-ray diffractogram into minute square grids (0.5 × 0.5 mm^2) and counting the number of grids. The degree of crystallinity of a polymer is affected by the secondary valence bonds that can be formed, the structure of the

polymer chain (range of order), the physical treatment and the molecular weight of the polymer.

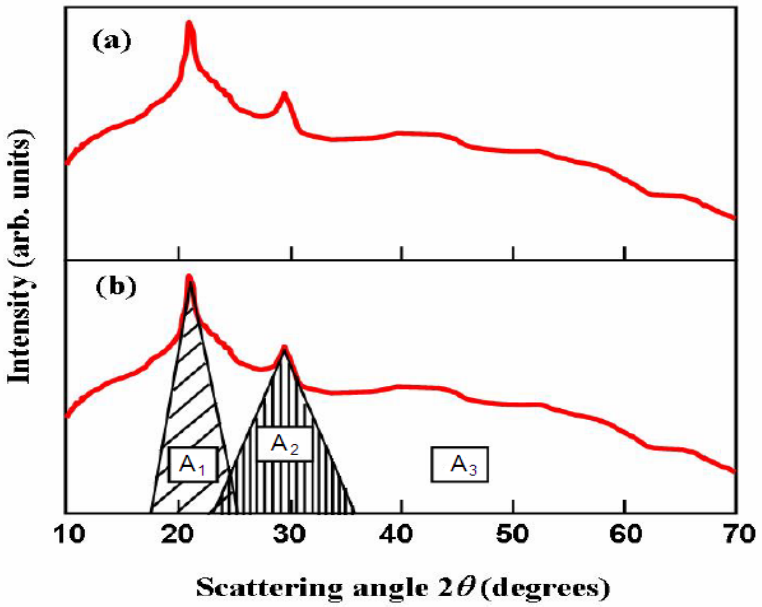

Figure 3.6: (a) Typical X-ray diffractogram of a semi-crystalline polymer and (b) XRD patterns showing the superposition of crystalline peaks and an amorphous hump.

3.3.3 Fourier transforms infrared spectroscopy (FTIR)

Fourier transforms infrared spectroscopy (FTIR) offers quantitative and qualitative analysis for organic, polymeric and some cases inorganic materials. It is an effective analytical tool for characterizing and identifying organic molecules, chemical bonds (functional groups) and the molecular structure of organic compounds. Atoms in molecules vibrate with natural frequencies in the range of 1013 to 1014 cycles per second, which is the frequency of infrared radiation [219]. When infrared radiation is exposed to an organic material, the molecules present in the material selectively absorb radiation of specific wavelength which causes the change of dipole moment of molecules. The frequency of absorption peak is determined by the vibrational energy gap and the number of peaks is related to the number of vibrational freedom of the molecule. The infrared spectrum represents a fingerprint of a material with absorption peaks which corresponds to the frequencies of vibrations between bonds

of the atoms making up the material. Since, each different material has unique combination of atoms, so no two compounds produce the exact same infrared spectrum. Therefore, FTIR spectroscopy can give a qualitative analysis of every different kind of material.

The FTIR spectroscopy measurement in the present work was carried out by employing Perkin Elmer Spectrum 100 spectrometer. For the FTIR measurement the synthesized powdered samples were mixed with KBr and pressed using hydraulic press to make pellets. Figure 3.7 shows the infrared spectrometer which is used for FTIR measurements in the present thesis work.

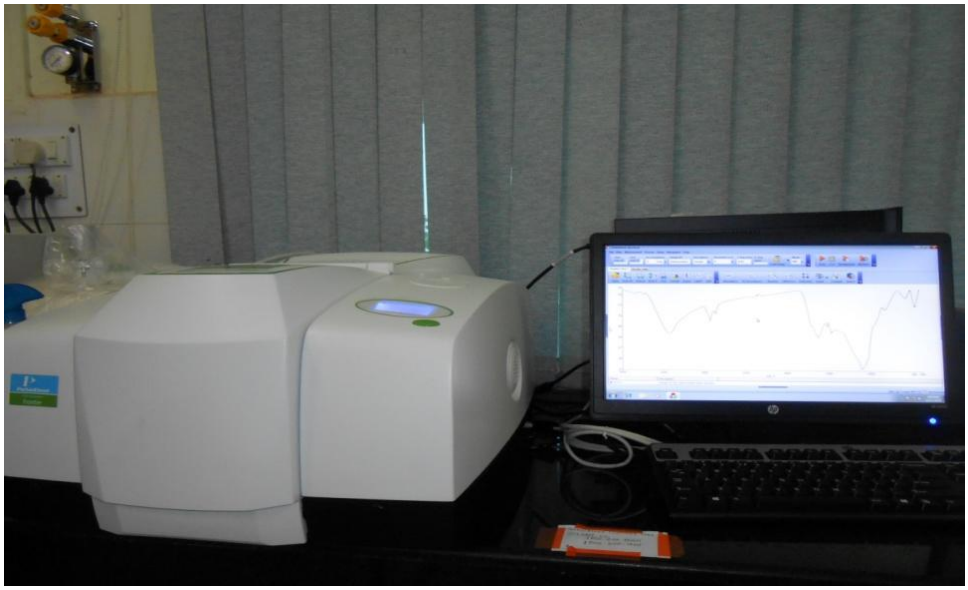

Figure 3.7: Photograph of FTIR spectrometer (Perkin Elmer, model spectrum 100).

3.3.4 Micro-Raman (μR) spectroscopy

Raman spectroscopy is the study of the interaction between light and matter in which the light is inelastically scattered. Raman spectroscopy has been widely used to characterize conducting polymers to investigate oxidation states, conductivity etc. [220-222]. Raman spectroscopy helps to identify the molecular structure of a material as the vibrational information is specific to chemical bonds and symmetry of the molecules. In Raman spectroscopy, photons of single wavelength are focused on the target material. Typically, a sample is illuminated with a laser beam at a certain frequency. When the photons incident on the target material they interact

with target materials and are either reflected, absorbed or scattered. The scattered light from the illuminated spot, which consists of Rayleigh and Raman scattering, is collected with a lens sent through a monochromator. Rayleigh scattering has the same frequency as the incident light and it is filtered out, whereas Raman scattering is dispersed onto a detector. The difference in frequency between the incident laser light and the observed Raman scattering gives the vibrational frequencies of the sample.

In the present work, the micro-Raman spectra of the poly(3,4-ethylenedioxythiophene) nanostructures were obtained by using a Renishaw in-Via micro-Raman spectrometer (Renishaw, Wotton-under-Edge, UK) with a resolution of 0.3 cm^{-1}. Ar^{+} laser of 514.5 nm wavelength was used for excitation. Figure 3.8 shows the micro-Raman spectrometer set up used for the present study.

Figure 3.8: Photograph of micro-Raman spectrometer (Renishaw in-via).

3.3.5 Thermogravimetric analysis (TGA)

Thermogravimetric analysis (TGA) is a quantitative measurement technique of mass change in materials associated with transition and thermal degradation under constant atmosphere. It records change in mass from dehydration, decomposition and oxidation of a sample with time and temperature. Characteristic thermogravimetric curves are obtained for specific materials and chemical compounds due to unique

sequence from physicochemical reactions occurring over specific temperature ranges and heating rates. The loss in weight over specific temperature ranges provides information about the sample composition as well as the thermal stability of the sample.

Thermal degradation studies in the present work were performed by using Perkin-Elmer thermogravimetric analyzer (TGA, Model 6000) in the temperature range of 50^{o}C-800^{o}C. The chamber was continuously swept with nitrogen to remove all corrosive gases formed during degradation and to avoid further thermo-oxidative degradation. To calculate the activation energy of thermal degradation of the samples, TGA measurements have been performed at four different heating rates viz., 10, 15, 20, 25 and 30 °C min^{-1}. The TGA setup used in the present work is shown in Fig. 3.9.

Figure 3.9: Photograph of set-up used for thermogravimetric analysis (Perkin Elmer, model STA 6000).

3.3.6 Dielectric relaxation spectroscopy (DRS)

Dielectric relaxation spectroscopy (DRS) has been widely employed to investigate the charge transport mechanism and relaxation phenomenon in conducting polymers [223, 224]. Dielectric relaxation spectroscopy is a useful technique that applies an AC electric field across a sample, sweeping in frequency, to provide information about the response of molecular dipoles and ionic species. Historically, "dielectric

relaxation" was coined by Dr. Petrus Debije in 1927 as the reorientation of molecular dipoles [225]. The overall frequency dependent electrical behavior can be understood by employing different formalisms such as: (i) complex impedance formalism (Z^*), (ii) complex dielectric formalism (ε^*), (iii) complex modulus formalism (M^*) and (iv) AC conductivity studies. The total AC response is a superposition of the dielectric response of the bound charges along with the hopping of localized charge carriers and the molecular structure deformation due to the charge carrier's diffusion [223]. There are different polarization mechanisms that can occur within a dielectric material such as electronic, ionic or atomic, dipolar or orientation and interfacial or space charge polarization. The complex dielectric permittivity (ε^*) is used to study the polarization mechanism, whereas the complex impedance (Z^*) and complex electric modulus (M^*) have been used to study the charge carriers relaxation mechanism [226].

In the present work, the dielectric measurements were carried out by sandwiching the pellets of the samples between the circular stainless electrodes in the frequency range of 20 Hz to 2 MHz by using Agilent E4980A Precision LCR Meter. Lakeshore temperature controller 340 has been used for controlling the temperature. From the dielectric measurements the parameters, complex impedance (Z^*), phase angle (ϕ) and capacitance (C) were obtained and the other parameters were calculated from the experimentally acquired data using different transformation equations.

3.3.6.1 Impedance formalism

The impedance is a complex quantity, having both magnitude $|Z|$ and phase angle (ϕ) and it is expressed as [227]:

$$Z(\omega) = |Z| \exp(-j\Phi) \tag{3.4}$$

$$Z(\omega) = |Z| cos\Phi - j|Z| sin\Phi \tag{3.5}$$

$$Z^*(\omega) = Z' - jZ'' \tag{3.6}$$

where Z' and Z'' are the real and imaginary parts of complex impedance (Z^*). The magnitude of impedance $|Z|$ and phase angle (ϕ) are measured using Agilent E4980A Precision LCR Meter in the frequency range of 20 Hz to 2 MHz

3.3.6.2 Dielectric permittivity formalism

The real (ε') and imaginary (ε'') parts of complex dielectric permittivity (ε^*) is calculated from using the following equations [228]:

$$\varepsilon'(\omega) = \frac{Z''}{2\pi f C_o |Z|^2} \tag{3.7}$$

and

$$\varepsilon''(\omega) = \frac{Z''}{2\pi f C_o |Z|^2} \tag{3.8}$$

where C_o is the capacitance in vacuum and it is expressed as:

$$C_o = \frac{\varepsilon_o A}{d} \tag{3.9}$$

where ε_o is the permittivity in free space and A and d are the cross-sectional area and thickness of the sample, respectively.

3.3.6.3 Modulus formalism

The complex electric modulus (M^*) has been calculated according to McCrum *et al.* [229] expression, which is expressed as:

$$M^* = \frac{1}{\varepsilon^*} = \frac{1}{\varepsilon' - j\varepsilon''} = \frac{\varepsilon'}{\varepsilon'^2 + \varepsilon''^2} + j\frac{\varepsilon''}{\varepsilon'^2 + \varepsilon''^2} = M' + jM'' \tag{3.10}$$

Where $j = \sqrt{-1}$ and M' and M'' are the real and imaginary parts of complex electric modulus respectively. The values of M' and M'' have been calculated from the real (ε') and imaginary (ε'') parts of complex permittivity (ε^*).

3.3.7 AC conductivity measurements

The total AC conductivity ($\sigma_{tot}(\omega)$) of the poly(3,4-ethylenedioxythiophene) nanostructures (nanoparticles, nanofibers and nanotubes) were calculated from the measured conductance $G(\omega)$ using the following expression [230, 231]:

$$\sigma_{tot}(\omega) = G(\omega)\frac{d}{A} \tag{3.11}$$

Where, d is the thickness of the sample and A is the cross-sectional area of the measured sample. The conductance $G(\omega)$ is measured using Agilent E4980A

Precision LCR Meter in the frequency range of 20 Hz to 2 MHz. For the AC conductivity measurements, the pellets of diameter 1 cm were inserted between the stainless steel circular electrode and stainless steel base plates of a sample holder. An AC signal with varying frequencies was applied across the sample and the conductance, impedance, phase and capacitance of the sample were measured. The instrument is interfaced with a computer to collect the data. It has a built in frequency synthesizer and has a frequency range of 20 Hz to 2 MHz. A Lakeshore temperature controller 340 was used to maintain the temperature. Figure 3.10 depict the measurement set-up used for dielectric and AC conductivity measurements.

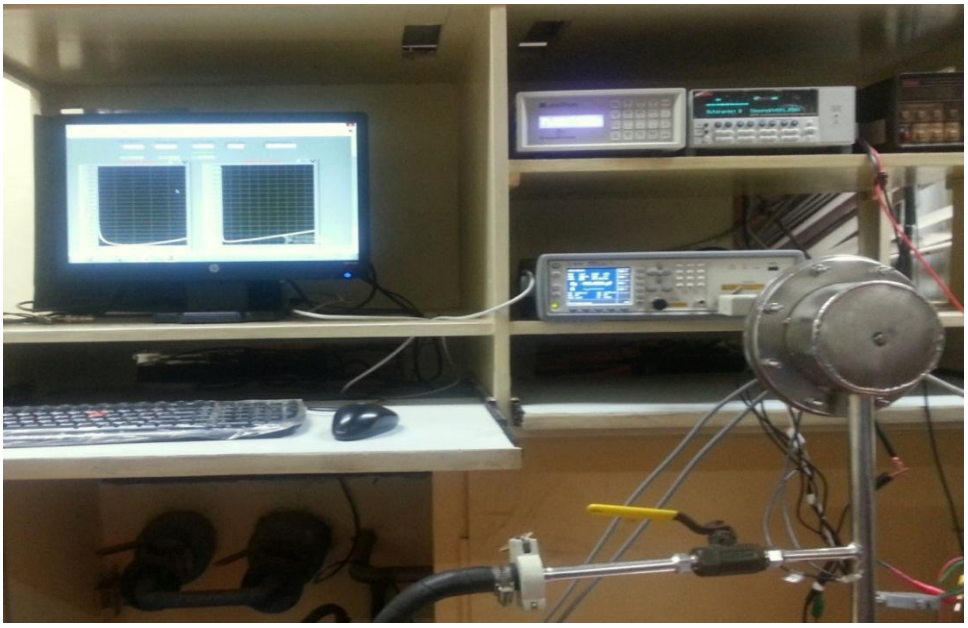

Figure 3.10: Set-up used for dielectric and AC conductivity measurements.

3.3.8 DC resistivity and Magnetoresistance

The dc resistivity and magnetoresistance measurements of the synthesized poly(3,4-ethylenedioxythiophene) nanostructures viz., nanoparticles, nanofibers and nanotubes were performed using standard four probe method. The synthesized powdered samples were pressed in a hydraulic press for making circular pellets of 1 cm diameter, which were cut into rectangular shape of typical dimension ~3.5×2.5×2 mm^3 to carry out the DC resistivity and magnetoresistance measurements. The samples were placed on a sample holder using GE varnish. For the electrical contacts

printed circuit board strips are fixed on opposite faces of the copper block at which the samples are connected. Four uninsulated copper wires (two each for current and voltage leads) are taken for the electrical contacts, which were made by using highly conducting silver paste. For a particular temperature, a desired current is allowed to pass through the outer two terminals of a sample from a sourcemeter, and a sensitive nanovoltmeter measures the resulting voltage across the inner two probes to determine the sample resistivity. A current switching card and a nanovolt scanner card which are coupled to a switching system to enable the data acquisition. After the measurements of all the connected samples is over the next temperature is set and repeats the scan steps as discussed above for the desired range of temperature. The DC resistivity measurements were performed in the temperature range of 5-300K. Magnetoresistance measurements were performed at different temperatures of 5, 10, 20, 30, 50, 100, 200 and 300K in the magnetic field range of 0 – 8 T. The magnetic field, acquired using a superconducting solenoid magnet made by Oxford Instruments, UK, was applied parallel to the sample. Lakeshore temperature controller 340, Keithley source meter 2400 and Keithley digital voltmeter 180 were used for the measurements. Figure 3.11 presents the measurement set-up used for resistivity and magnetoresistance measurements.

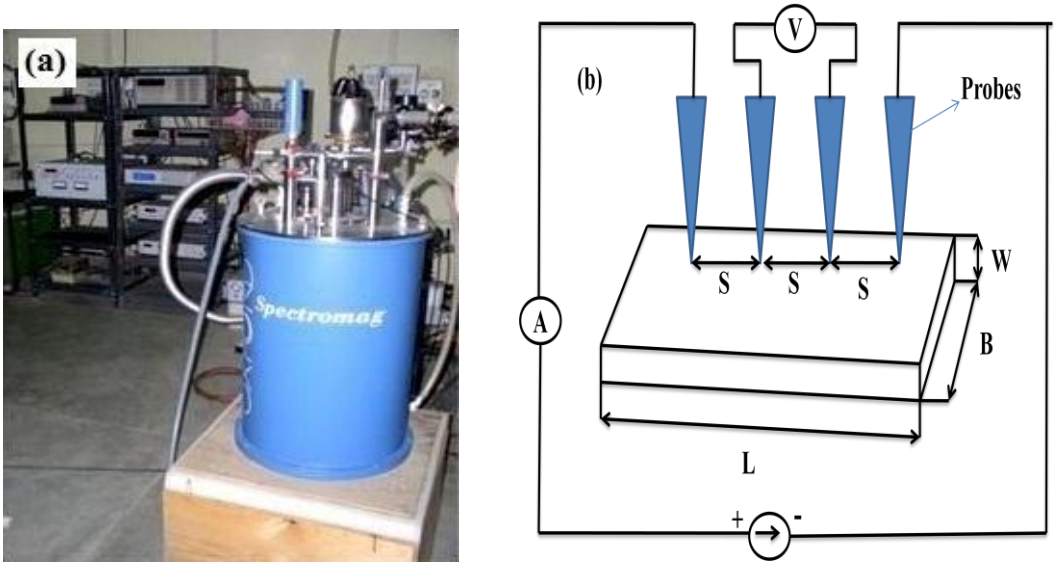

Figure 3.11: (a) The set-up used for measuring DC resistivity and magnetoresistance, and (b) schematic of four probe measurement.

Chapter 4

Structural, vibrational and thermal analysis of poly(3,4-ethylenedioxythiophene) nanoparticles, nanofibers and nanotubes

This chapter describes the investigations of structural, vibrational and thermal properties of poly(3,4-ethylenedioxythiophene) nanoparticles, nanofibers and nanotubes. The shape and size of poly(3,4-ethylenedioxythiophene) nanostructures are determined by using high resolution transmission electron microscope. X-ray diffractometer is used to study the polymer chains alignment in the nanostructures. Different bonds vibrations present in the poly(3,4-ethylenedioxythiophene) nanostructures have been studied through the framework of Fourier transform infrared spectroscopy and micro-Raman spectroscopy. Finally, the thermal stability of the nanostructures has been studied using thermogravimetric analyzer.

4.1 Introduction

In the last few decades, there has been remarkable progress in conducting polymer nanostructures with their nanoscale and molecular scale properties. When the size of the materials is reduced to nanoscale, its properties are radically improved or new properties emerge. These nanostructures have deep impact on both fundamental research and potential applications in nano-electronics, solid state devices, biotechnology and medicine [232-235]. Conducting polymers are heterogeneous systems composed of partially ordered crystalline regions and disordered amorphous regions. The charge transport in such heterogeneous systems takes place through electron delocalization or hopping of the charge carriers [143, 144]. The range of charge carriers' delocalization in the disordered materials is controlled by the fraction of crystalline materials and local order in the crystalline and amorphous region [236]. The charge carrier mobility is highly dependent on the structure, morphology and long-range order of polymer chains. For better understanding the

charge transport mechanism in conducting polymer nanostructures, it is important to understand the morphology, structure and ordering of polymer chains. The high resolution transmission electron microscopy (HRTEM) and X-ray diffraction (XRD) characterization can provide vital information about the morphology, shape of nanostructures and the alignment of polymer chains. Different bonds vibrations present in the system and conformational transition can be figured out with the help of Fourier transform infrared spectroscopy (FTIR) and micro-Raman spectroscopy.

In the present thesis, we have synthesized three different PEDOT nanostructures namely, dodecylbenzene sulfonic acid (DBSA) doped nanoparticles, sodium dodecyl sulfate (SDS) doped nanofibers and camphorsulfonic acid (CSA) doped nanotubes. Four different samples were synthesized for each nanostructured system with systematically varying dopant concentration. All the nanostructures were synthesized following chemical method using surfactants and amphiphilic acids.

In this chapter the structural, vibrational and thermal properties of different PEDOT nanostructures viz., nanoparticles, nanofibers and nanotubes have been discussed. HRTEM has been used to determine the shape and size distribution of the nanostructures. XRD measurements were carried out to know the polymer chains alignments in the nanostructures. The degree of crystallinity (K) and crystallite size (L) were calculated from the XRD patterns. FTIR and micro-Raman characterizations have been used to get information about the different bond vibrations and conformation transition from benzenoid to quinoid structure. Thermogravimetric analysis has been performed to study the thermal stability of the synthesized nanostructures.

4.2 Structural analysis of PEDOT nanoparticles, nanofibers and nanotubes

4.2.1 High resolution transmission electron microscopy (HRTEM) analysis

Figures 4.1 (a & b) show the representative high resolution transmission electron micrographs (HRTEM) of PEDOT nanoparticles for lowest (0.003M) and highest (1M) DBSA concentration, respectively. It is observed that the particles of 0.003M

DBSA doped sample are well ordered with diameter varying from 10 - 18 nm. However, the particles are larger and agglomerate for 1M DBSA doped sample with diameter varying from 25 – 70 nm. The diameter distribution histograms of PEDOT nanoparticles are shown in Figs. 4.2 (a & b). The distribution of nanoparticles diameter have been fitted with Gaussian distribution function using Origin 8.5 software, which determines the average diameter of the nanoparticles. From the histograms the average diameter of 0.003M and 1M DBSA doped nanoparticles are found to be 13 nm and 40 nm, respectively. It is observed that for 0.003M of DBSA doped sample the particles are spherical and well separated, however, for 1M DBSA doped sample the particles are larger and are agglomerated. With increasing DBSA concentration, the micelle size increases due to aggregation of smaller micelle which is formed at lower DBSA concentration resulting in the larger diameter nanoparticles at higher DBSA concentration.

Figures 4.3 (a & b) depict the selected area electron diffraction (SAED) patterns of PEDOT nanoparticles for 0.003M and 1M DBSA doped samples, respectively. The presence of diffused rings (amorphous) interspersed with bright-spots (crystalline) confirms the semi-crystalline nature of the nanoparticles.

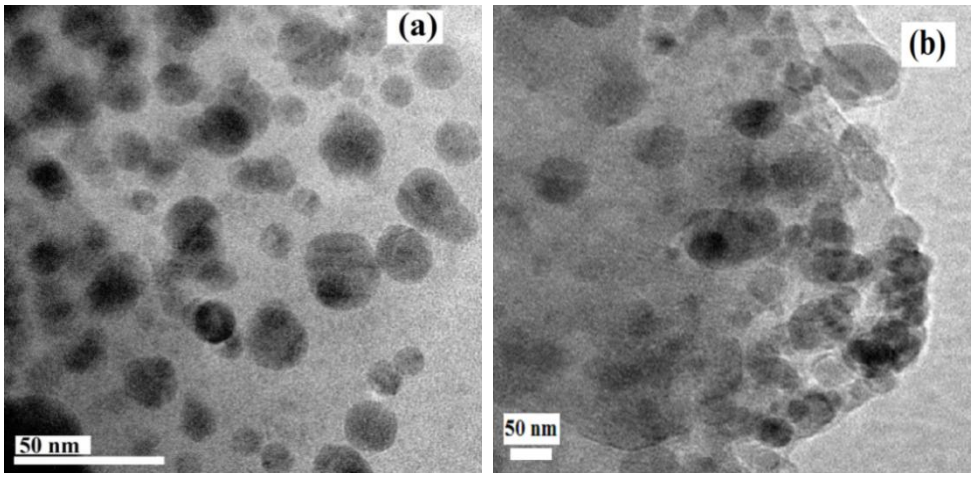

Figure 4.1: Representative HRTEM images of PEDOT nanoparticles for (a) 0.003M and (b) 1M DBSA concentration**.**

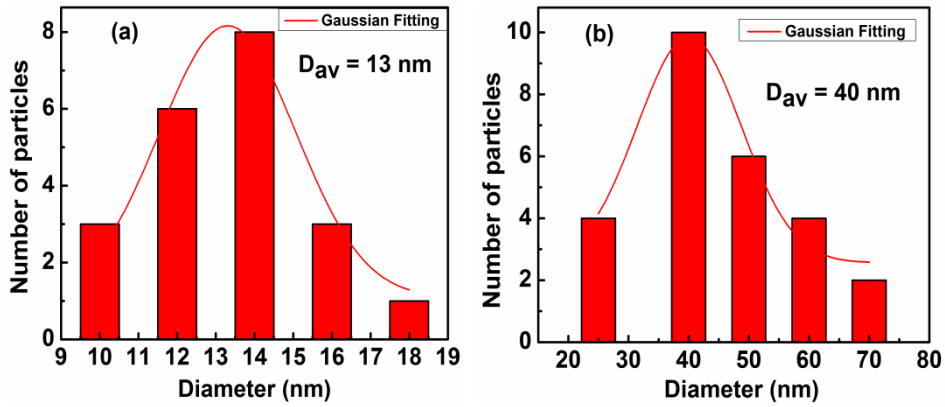

Figure 4.2: Diameter distribution histogram of PEDOT nanoparticles for (a) 0.003M and (b) 1M DBSA concentration.

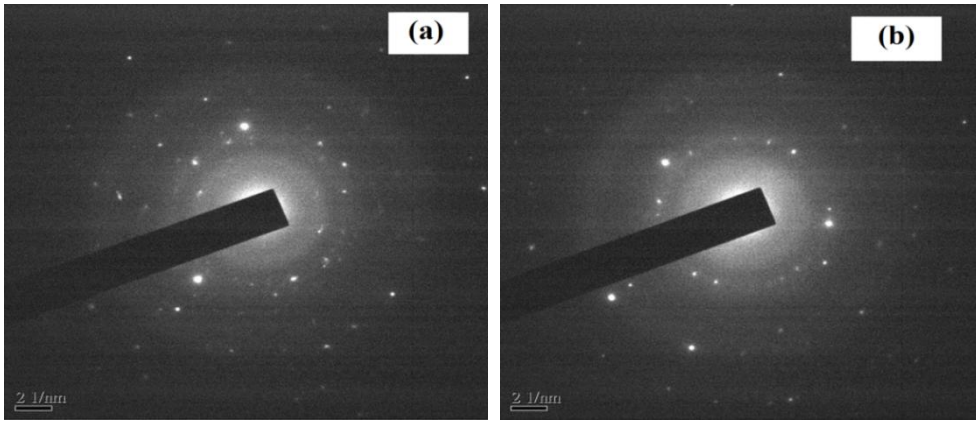

Figure 4.3: SAED patterns of PEDOT nanoparticles for (a) 0.003M and (b) 1M DBSA concentration.

The representative HRTEM images of PEDOT nanofibers for 0.03M and 1M SDS doped samples are shown in Figs. 4.4(a & b). The HRTEM images show the formation of nanofibers with diameter ranging from 6 - 20 nm. The length of the nanofibers varies from 100 nm to 200 nm. When anionic surfactant sodium dodecyl sulfate (SDS) is added to the aqueous solution, it combines with water and produce aqueous micellar solution, where the critical micelle concentration (CMC) of SDS at 20^{o}C is 8 mM. When the SDS concentration is increased to the second CMC value of 70 mM at 20^{o}C, the micelle shape transition takes place from spherical to ellipsoidal shape. Further increase in SDS concentration results in a transition to rod like shape to accommodate more surfactant molecules for minimizing the free energy of the system. As the oxidant ($FeCl_3$) solution is added to the micelle

solution, it helps in aggregation of more surfactant molecules due to increase of ionic strength. When the EDOT monomer is added into the oxidant/micelle solution, it migrates into the rod like micelles due to its hydrophobic nature and polymerization occurs inside the guided rod like micelle leading to the formation of nanofibers [237]. The diameter distribution histogram of PEDOT nanofibers are presented in Figs. 4.5 (a & b). The average diameter of PEDOT nanofibers have been determined following the same way as discussed earlier. From the Gaussian fitting, it is observed that the average diameters of PEDOT nanofibers are 14 nm and 15.5 nm for 0.03M and 1M SDS doped samples, respectively.

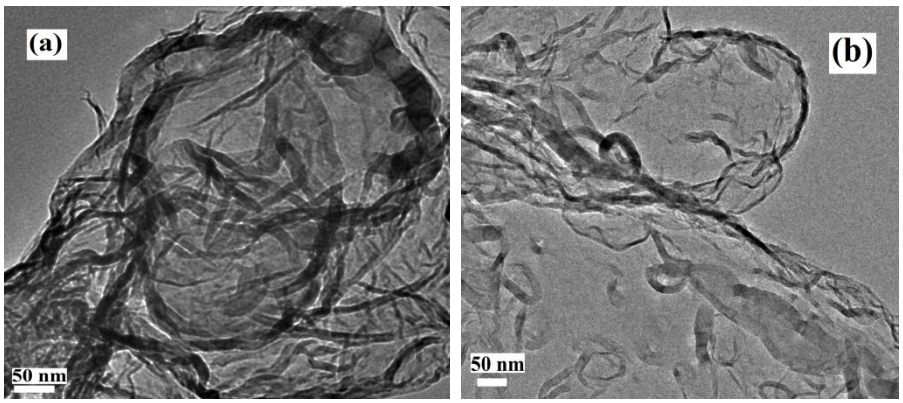

Figure 4.4: HRTEM images of PEDOT nanofibers for (a) 0.03M and (b) 1M SDS concentration.

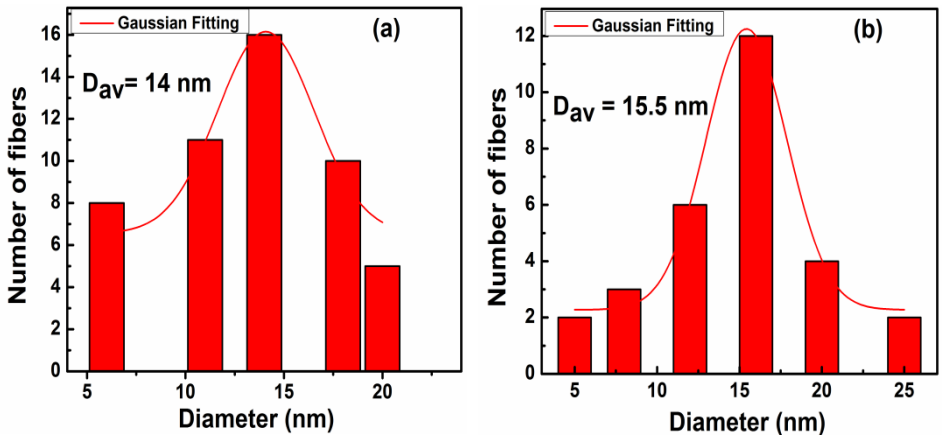

Figure 4.5: Diameter distribution histogram of PEDOT nanofibers for (a) 0.03M and (b) 1M SDS concentration.

Figure 4.6 (a & b) represents the corresponding SAED pattern of PEDOT nanofibers for 0.03M and 1M of SDS dopant concentration. The presence of

diffraction spots and blurred electron diffraction rings suggests the semi-crystalline nature of the synthesized nanofibers.

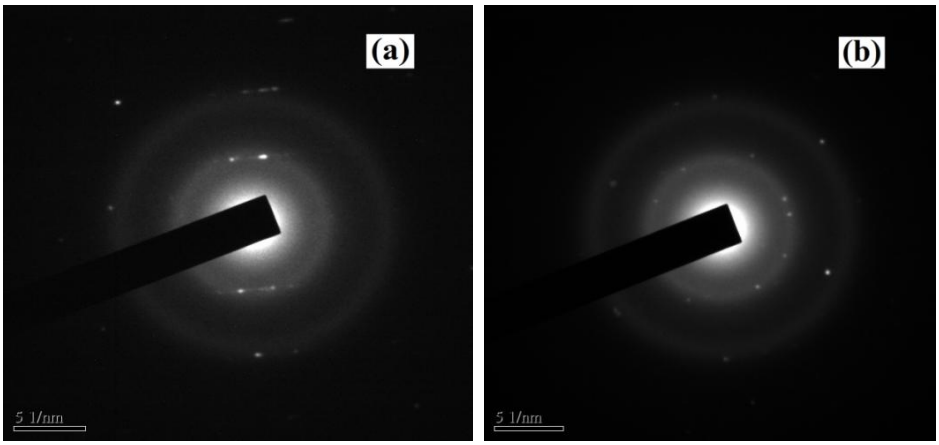

Figure 4.6: SAED patterns of PEDOT nanofibers for (a) 0.03M and (b) 1M SDS concentration.

Figures 4.7 (a & b) depict the representative HRTEM images of PEDOT nanotubes for 0.001M and 1M of CSA concentration, respectively. The outer diameter of 0.001M CSA doped nanotubes varies from 55 to 90 nm whereas it varies from 70 nm to 161 nm, for 1M CSA doped sample. The inner diameter of 0.001M CSA doped nanotubes varies from 6 to 12 nm, while it varies from 25 to 75 nm for 1M CSA doped nanotubes. The outer diameter distribution histogram of PEDOT nanotubes for 0.001M and 1M CSA concentration are shown in Figs. 4.8 (a & b). The average outer diameter of the nanotubes is found to be 65 nm and 101 nm for 0.001M and 1M of CSA concentration, respectively. The increase of nanotubes diameter with increasing CSA concentration can be explained similarly as in the case of DBSA doped nanoparticles discussed above. As CSA acts as surfactant as well as functional dopant, with increasing concentration due to increase of micelle size results in the larger diameter nanotubes at higher CSA concentration.

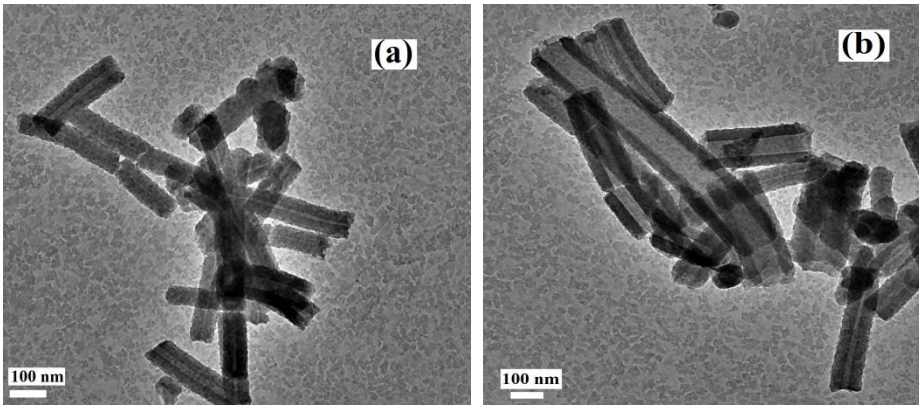

Figure 4.7: HRTEM images of PEDOT nanotubes for (a) 0.001M and (b) 1M CSA concentration.

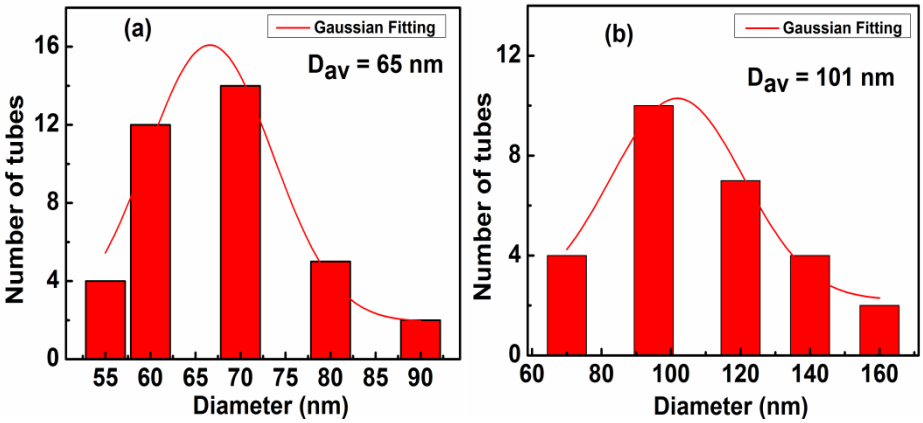

Figure 4.8: Diameter distribution histogram of PEDOT nanotubes for (a) 0.001M and (b) 1M CSA concentration.

Figures 4.9 (a & b) illustrate the selected area electron diffraction (SAED) patterns of 0.001M and 1M CSA doped PEDOT nanotubes, respectively. The diffraction patterns exhibit a set of well-defined, however, asymmetrically distributed, diffraction spots indicating an oriented crystallized structure. The figures also show spots on the circular rings indicating that the synthesized PEDOT nanotubes consist of amorphous and crystalline phases.

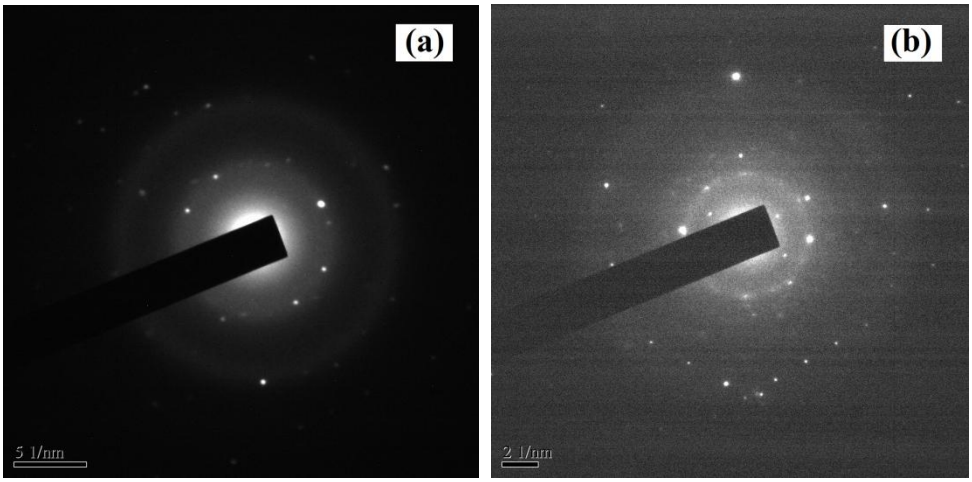

Figure 4.9: SAED patterns of PEDOT nanotubes for (a) 0.001M and (b) 1M CSA concentration.

4.2.2 X-ray diffraction studies

Figure 4.10 shows the X-ray diffraction (XRD) patterns of PEDOT nanoparticles for different DBSA concentration in the 2θ range from 5^0 to 40^0. The sharp diffraction peak observed at 12.1^o can be ascribed to the (200) planes. The diffraction hump centered at 18.7^o corresponds to the (300) planes [238]. From the diffraction patterns it is observed that with increasing DBSA concentration the diffraction peak intensity increases and it can be ascribed to the enhancement of polymer chains ordering due to insertion of DBSA anions in between the polymer chains. With increasing DBSA concentration increased numbers of DBSA anions are inserted into the interstitial regions between the polymer chains resulting in higher ordering, which leads to higher crystalline diffraction peaks in the diffraction patterns. Moreover, with increasing DBSA concentration, the diffraction peaks become narrower indicating increase in particle size as also confirmed from HRTEM.

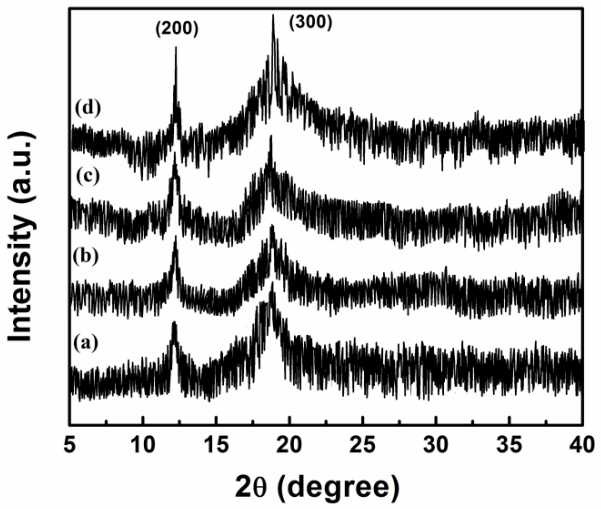

Figure 4.10: X-ray diffraction pattern of PEDOT nanoparticles for (a) 0.003M, (b) 0.01M, (c) 0.1M and (d) 1M DBSA concentration.

X-ray diffraction patterns of PEDOT nanofibers for different SDS concentration are shown in Fig. 4.11. The diffraction peaks centered around 6.7^{o}, 18.8^{o} and 25.3^{o} correspond to the (100), (300) and (400) planes, respectively [238]. The intense diffraction peak centered at 25.3^{o} is attributed to the inter-chain planar ring-stacking distance [237]. The enhancement of sharpness of the 25.3^{o} diffraction peak with increasing SDS concentration is attributed to increase in inter-chain planar ring-stacking. With increasing SDS concentration, higher number of SDS dopant anions go into the polymer chains leading to the ordering of polymer chains.

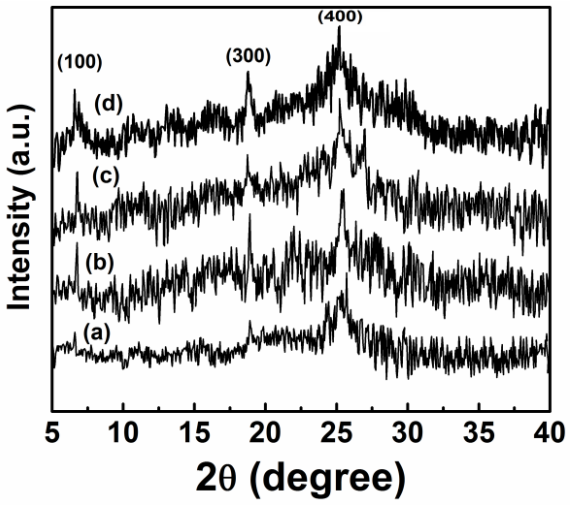

Figure 4.11: X-ray diffraction pattern of PEDOT nanofibers for (a) 0.03M, (b) 0.1M, (c) 0.5M and (d) 1M SDS concentration.

Typical XRD patterns of PEDOT nanotubes with varying CSA concentration are shown in Fig. 4.12. The XRD patterns show three diffraction peaks. The diffraction peaks centered at 2θ = 6.4^o (d = 13.8 Å) and 2θ = 18.8^o (d = 3.1 Å) are correspond to the reflection from (100) and (300) planes, respectively [238]. The main diffraction peak observed around 2θ = 26^o (d = 3.4 Å) is due to the reflection from (400) plane [238]. The diffraction peak at 2θ = 26^o is attributed to the inter-chain planar ring stacking distance [237]. The enhancement of sharpness of the diffraction peaks intensity with increasing CSA concentration can be attributed to the increase of polymer chains ordering leading to the higher crystallinity.

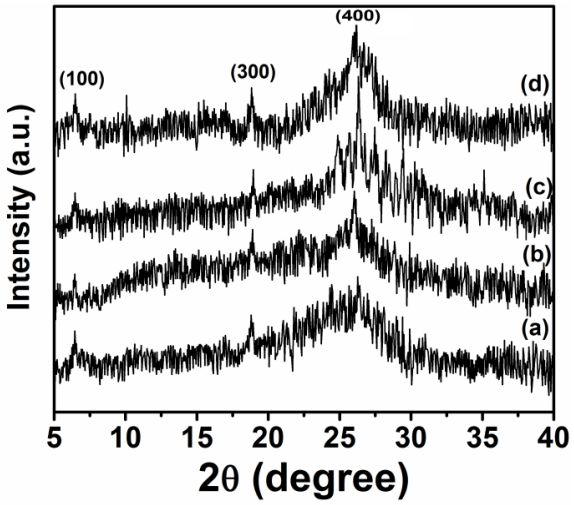

Figure 4.12: X-ray diffraction pattern of PEDOT nanotubes for (a) 0.001M, (b) 0.01M, (c) 0.1M and (d) 1M CSA concentration.

The average crystallite size (L) for all the PEDOT nanostructures are estimated through the XRD patterns using the Scherrer Equation [239, 240].

$$\beta = \frac{0.89\lambda}{Lcos\theta} \tag{4.1}$$

where λ is the X-ray wavelength (λ = 1.5406 Å), L is the average crystallite size, β is the full-width at half-maximum and θ is Bragg angle in degree. The calculated values of average crystallite size for all the systems are presented in Table 4.1. It is observed from Table-4.1 that crystallite size (L) increases with increasing dopant concentration and it can be attributed to increase in nanostructures size as confirmed from HRTEM images.

For better confirmation about the enhancement of polymer chains alignment with increasing dopant concentration for all the nanostructured systems the degree of crystallinity (*K*) has been calculated from the diffractogram by using the relation [241]:

$$K = \frac{A}{A'} \times 100\% \tag{4.2}$$

where *A* is the sum of areas of all the diffraction peaks and *A′* is the total area under the diffraction pattern. The calculated values of percentage of crystallinity are presented in Table 4.1. The degree of crystallinity increases with increasing dopant concentration for all the nanostructured systems and it can be ascribed to the increase in systematic alignment of the polymer chains due to insertion of bulky dopant anions in between the polymer chains.

Table 4.1: *Crystallite size (L) and degree of crystallinity (K) of PEDOT nanostructures at different dopant concentrations.*

Sample name	***L* (±0.01) (Å) for 2θ=18.8^o**	***K* (%)**
PEDOT nanoparticles		
0.003M DBSA	22.63	12.01
0.01M DBSA	28.37	17.45
0.1M DBSA	38.61	24.34
1M DBSA	47.93	31.73
PEDOT nanofibers		
0.03M SDS	48.46	15.23
0.1M SDS	52.05	19.37
0.5M SDS	54.12	23.67
1M SDS	54.37	38.97
PEDOT nanotubes		
0.001M CSA	28.14	16.57
0.01M CSA	28.14	22.03
0.1M CSA	35.17	31.04
1M CSA	46.84	46.19

4.3 Vibrational analysis of PEDOT nanoparticles, nanofibers and nanotubes

4.3.1 Fourier transform infrared spectroscopy

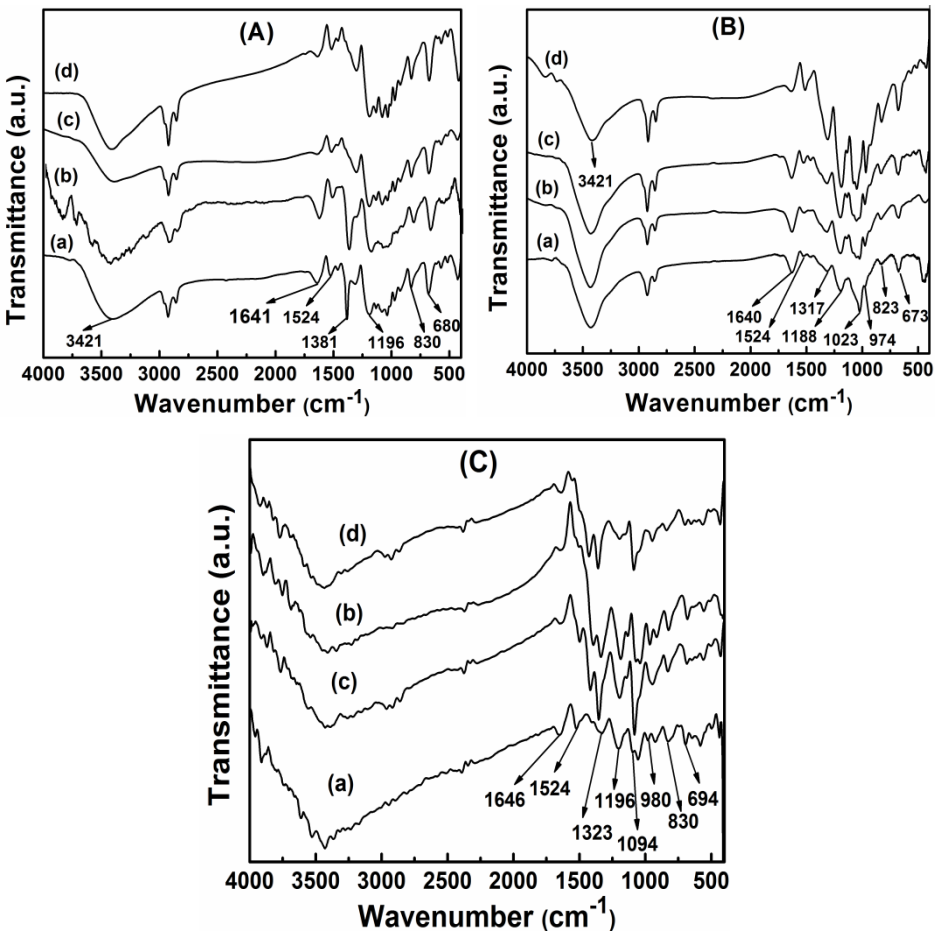

Figure 4.13: FTIR spectra of PEDOT (A) nanoparticles for (a) 0.003M, (b) 0.01M, (c) 0.1 and 1M DBSA concentration (B) nanofibers for (a) 0.03M, (b) 0.1M, (c) 0.5 and 1M SDS concentration and (C) nanotubes for (a) 0.001M, (b) 0.01M, (c) 0.1 and 1M CSA concentration.

Fourier transform infrared (FTIR) spectra provide information about the different chemical bonding present in a chemical compound. FTIR spectra of synthesized PEDOT nanostructures for different dopant concentrations are shown in Figs. 4.13 (A, B & C). Figure 4.13 (A) depicts the FTIR spectra of PEDOT nanoparticles for different DBSA concentrations. In Fig. 4.13 (A) the characteristic bands observed at 1381 cm^{-1} and 1524 cm^{-1} are ascribed to the C-C and C=C

stretching of quinoid structure and the ring stretching of thiophene ring, respectively [242, 243]. The vibrational band observed at 1196 cm^{-1} corresponds to the C-O-C bond stretching in the ethylene-dioxy group. The vibrational bands observed at 830 cm^{-1} and 680 cm^{-1} are due to C-S bond vibration [244-247]. The absorption bands observed in the wavenumber range of 2800-3000 cm^{-1} is ascribed to the aliphatic C-H stretching mode depending on long alkyl tail of DBSA [248]. The absorption bands observed at 1641 cm^{-1} and 3421 cm^{-1} are attributed to the C=C stretching vibration band of phenyl side group and O-H stretching vibration, respectively [248, 249]. The different IR bands observed in PEDOT nanostructures are presented in Table 4.2.

Table 4.2: *Characteristic IR bands of PEDOT and their assignments.*

Wavenumber (cm^{-1})	Band assignments
3421	O-H stretching [249]
2800-3000	aliphatic C–H stretching mode [248]
1641	C=C stretching [249]
1524	C=C stretching of ring thiophene [242]
1323, 1381	C-C stretching of quinoid structure [243, 250]
1196, 1094	C-O-C stretching vibration [244, 245]
974, 830, 680	C-S stretching [246, 247]

4.3.2 Micro-Raman spectroscopy

Raman spectroscopy is a powerful tool to study the bond stretching vibrations of carbon materials and conducting polymers. Figures 4.14 (A, B & C) depict the micro-Raman spectra of PEDOT nanostructures for different dopant concentrations. Figure 4.14(A) shows the micro-Raman spectra of PEDOT nanoparticles for different DBSA concentrations. In Fig. 4.14 (A) the two absorption bands at 1505 cm^{-1} and 1567 cm^{-1} are attributed to the C=C asymmetric stretching vibration of thiophene rings in the middle and at the end of the chains, respectively [251]. The vibration band observed at 1443 cm^{-1} is attributed to the symmetric $C_\alpha=C_\beta$ stretching deformation [252]. The bands at 1258 cm^{-1} and 1364 cm^{-1} are due to the inter-ring

C_α-$C_{\alpha'}$ stretching vibration and C_β-C_β stretching deformation in the aromatic deformation thiophene ring, respectively [253, 254]. The absorption bands observed at 1119 cm^{-1} and 438 cm^{-1} are ascribed to the C-O-C deformation and SO_2 bending, respectively. The bands at 988 cm^{-1} and 571 cm^{-1} are attributed to the oxyethylene ring deformation [253-255]. From Fig. 4.14 (A & C), it is observed that with increasing dopant concentration the symmetric C_α=C_β stretching deformation band red shifted (from 1443-1437 cm^{-1} for PEDOT nanoparticles and 1440-1430 cm^{-1} in case of PEDOT nanotubes). The red shifting of the symmetric band can be attributed to the conformational transition from benzenoid to quinoid structures. The benzenoid structure forms a coiled conformation, whereas quinoid structure favors a linear conformation. In the linear quinoid conformation, the charge carriers are more delocalized as a result they can hop easily from one localized site to the other. This transformation of the resonant structure suggests the change in the PEDOT chains from the coil like conformation to the expanded-coil or linear conformation [256, 257]. The π-electrons in quinoid structure are more delocalized due to the presence of two PEDOT rings almost in the same plane giving rise to higher conductivity. Different bond vibrations present in PEDOT nanoparticles, nanofibers and nanotubes are presented in Table-4.3.

Table 4.3: *Characteristic Raman bands of PEDOT and their assignments.*

Raman shift (cm^{-1})	Band assignments
1567, 1505	C=C asymmetric stretching vibration [251]
1443	symmetric C_α=C_β stretching [252]
1364	C_β-C_β stretching deformation [252]
1258	inter-ring C_α-$C_{\alpha'}$ stretching [253]
1119	C-O-C deformation [253, 254]
988, 571	oxyethylene ring deformation [254, 255]
438	SO_2 bending [254, 255]

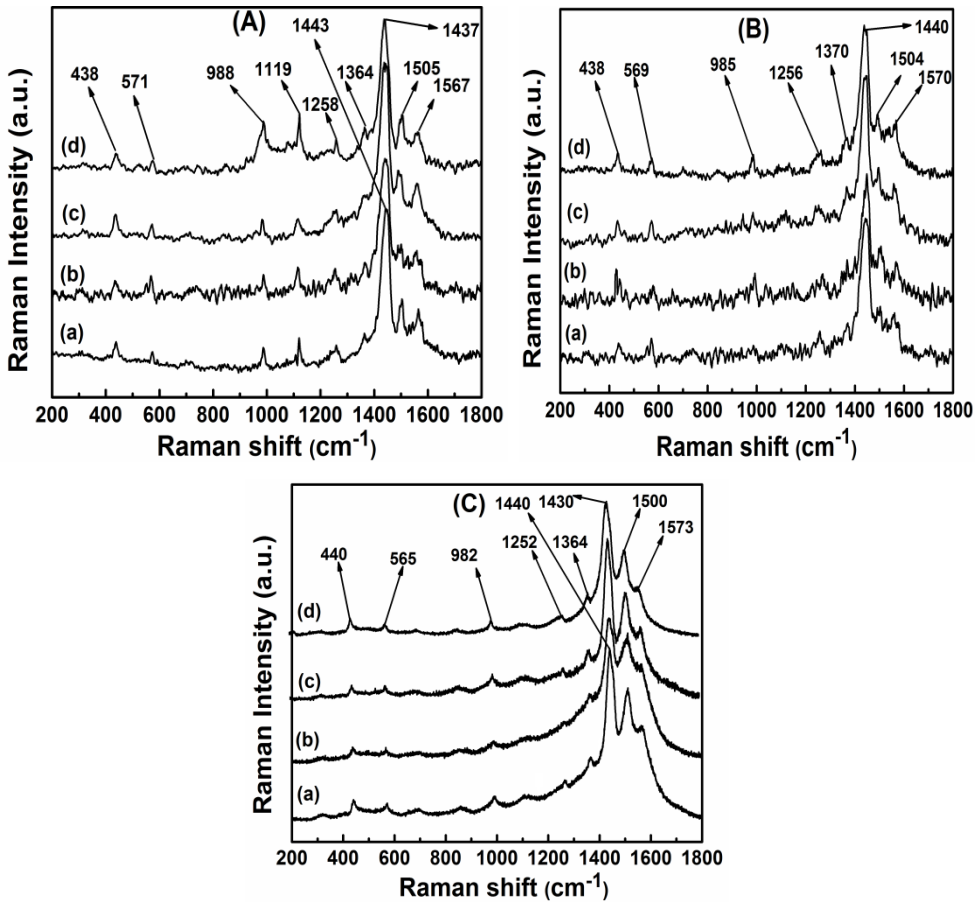

Figure 4.14: Micro-Raman spectra of PEDOT (A) nanoparticles for (a) 0.003M, (b) 0.01M, (c) 0.1 and 1M DBSA concentration (B) nanofibers for (a) 0.03M, (b) 0.1M, (c) 0.5 and 1M SDS concentration and (C) nanotubes for (a) 0.001M, (b) 0.01M, (c) 0.1 and 1M CSA concentration.

4.4 Thermogravimetric analysis (TGA) of PEDOT nanoparticles, nanofibers and nanotubes

Thermogravimetric analysis (TGA) is an important dynamic method to detect the degradation behavior of the synthesized nanostructures. Figures 4.15 (a, b & c) show the TGA plots of the PEDOT nanostructures. The thermograms show two step weight loss processes for all PEDOT nanostructured systems. The first weight loss upto 120 ^{o}C for all the nanostructured systems can be attributed to the evaporation of moisture and water molecules trapped in the polymer chains. The second major weight loss observed in the temperature range of 300-354^{o}C is ascribed to the degradation of polymer backbones.

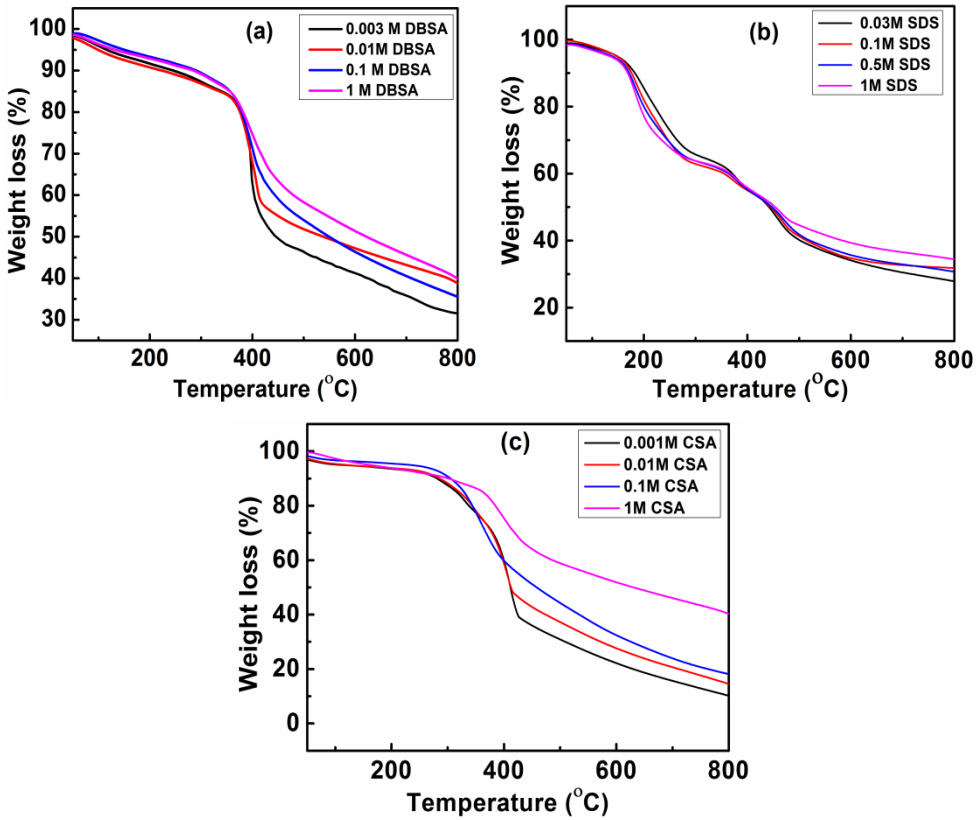

Figure 4.15: Thermogravimetric plots of PEDOT (a) nanoparticles, (b) nanofibers and (c) nanotubes for different dopant concentration.

Figures 4.16 (a, b & c) depict the derivatives TGA plots of PEDOT nanoparticles, nanofibers and nanotubes for different dopant concentrations. Different thermal decomposition temperature such as onset decomposition temperature (T_{onset}), rapidest decomposition temperature (T_{rpd}) and maximum weight loss at T_{rpd} temperature are summarized in Table 4.4. From Table 4.4, it is observed that the maximum decomposition temperature T_{rpd} shifted towards higher temperature with increasing dopant concentration and weight loss at T_{rpd} also decreases. The shifting of T_{rpd} towards higher temperature can be attributed to the enhancement of thermal stability of the systems with increasing dopant concentration. The increase of thermal stability with increasing dopant concentration results due to the increase of polymer chains ordering i.e. enhancement of crystallinity as confirmed from XRD analysis.

Table 4.4: *T_{onset}, T_{rpd} and residue at 550 °C of PEDOT nanoparticles, nanofibers and nanotubes for different dopant concentrations.*

Sample name	T_{onset} (°C)	T_{rpd} (°C)	Residue at 550 °C (%)
PEDOT nanoparticles			
0.003M DBSA	331	397	43
0.01M DBSA	333	400	49
0.1M DBSA	341	404	50
1M DBSA	350	411	54
PEDOT nanofibers			
0.03M SDS	333	372	36
0.1M SDS	346	378	37
0.5M SDS	350	380	38
1M SDS	366	393	41
PEDOT nanotubes			
0.001M CSA	279	358	26
0.01M CSA	298	373	32
0.1M CSA	325	402	38
1M CSA	340	412	56

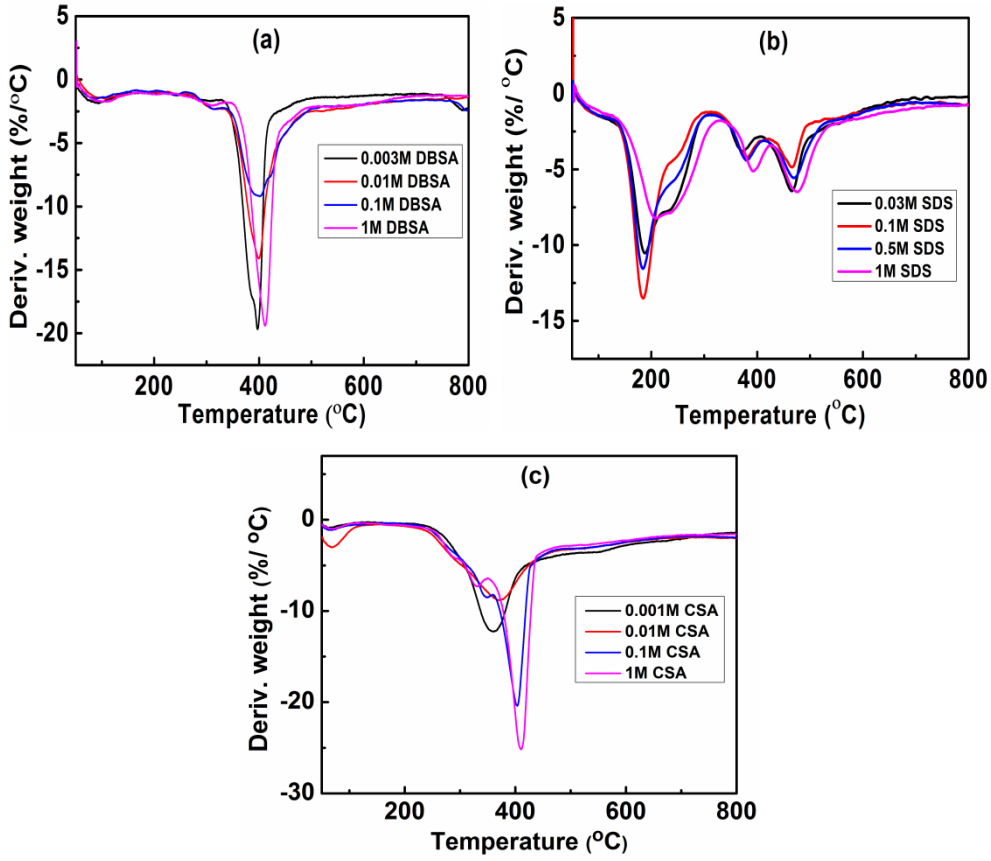

Figure 4.16: Derivative TG plots of PEDOT (a) nanoparticles, (b) nanofibers and (c) nanotubes at different dopant concentrations.

The degradation kinetics study provides a suitable platform for evaluating the thermal stability of a system. The thermal degradation kinetics and activation energy of degradation have been evaluated from the TGA curves using Flynn-Wall-Ozara (F-W-O) non-isothermal iso-conversion method [201, 202]. The kinetic parameter activation energy E_d of thermal degradation has been calculated by following the F-W-O method expressed as:

$$log\beta = -0.4567\frac{E_d}{R} \times \frac{1}{T} + Constant \tag{4.3}$$

where β, R, T and E_d are the heating rate, gas constant, temperature and activation energy of thermal degradation, respectively. The kinetic parameter activation energy of thermal degradation is calculated from the slope of the logβ *vs.* 1000/T plots. Figures 4.17 (a, b & c) show the logβ *vs.* 1000/T plots with five different heating rates (10, 15, 20, 25 and 30°C/min) for different degree of conversion (X) of PEDOT nanoparticles, nanofibers and nanotubes for 1M of dopant concentration. The degree of conversion is expressed as:

$$X = \frac{W_0 - W_t}{W_0 - W_f} \tag{4.4}$$

where W_0, W_t and W_f are the initial, at time t and final mass of the sample, respectively. In Fig. 4.17 the symbols represents the degree of conversion (X) and solid lines are the best fitted lines according to eq. (4.3). The nearly parallel behavior of fitted lines at different degree of conversions indicates the possibility of single step reaction mechanism. The calculated values of activation energy of thermal degradation for different degree of conversions of PEDOT nanoparticles, nanofibers and nanotubes for 1M dopant concentration are presented Table 4.5. The high value of thermal degradation activation energy for 1M CSA doped nanotubes indicates the higher thermal stability of the system as compared to 1M DBSA and 1M SDS doped nanoparticles and nanofibers, respectively. The high thermal stability of PEDOT nanotubes can be attributed to the high value of degree of crystallinity as confirmed from XRD analysis.

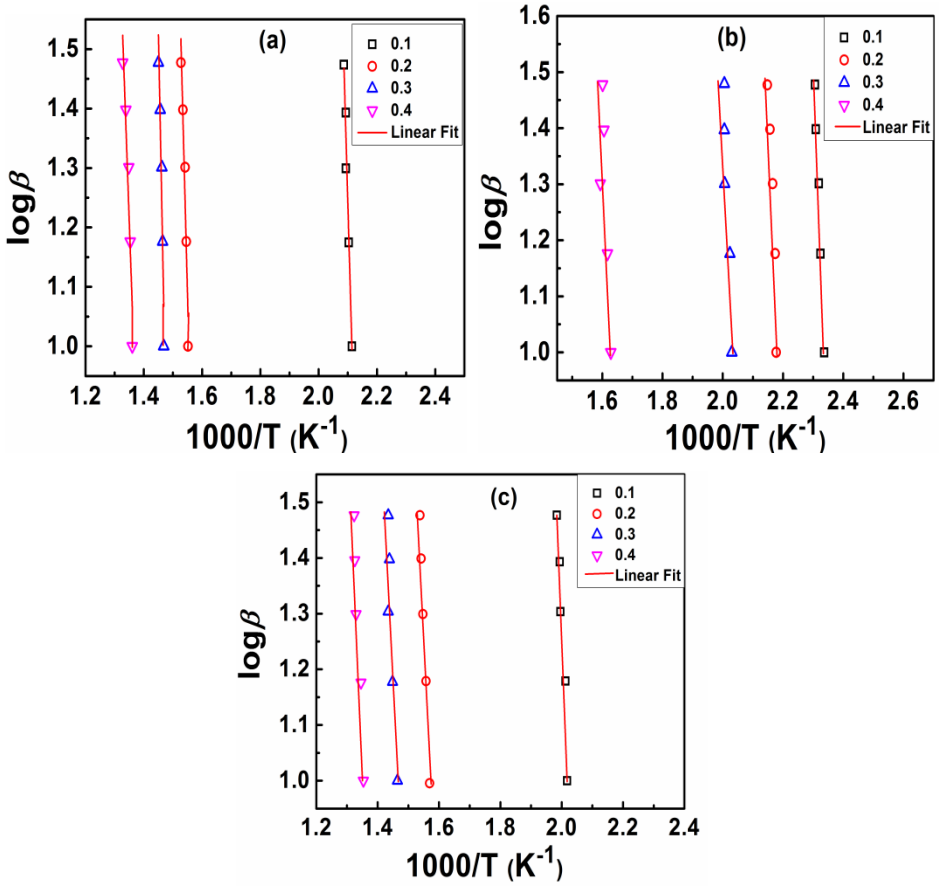

Figures 4.17: logβ *vs.* 1000/T plots at five different heating rates (10, 15, 20, 25 and 30°C/min) for different degree of conversions (*X*) of (a) 1M DBSA doped PEDOT nanoparticles, (b) 1M SDS doped PEDOT nanofibers and (c) 1M CSA doped PEDOT nanotubes.

Table 4.5: *Activation energy (E_d) of thermal degradation of PEDOT, nanoparticles, nanofibers and nanotubes for 1M Dopant concentration.*

Conversion (*X*)	***E_d* (J/mol)**		
	1M DBSA doped PEDOT nanoparticles	1M SDS doped PEDOT nanofibers	1M CSA doped PEDOT nanotubes
0.1	315.84	305.27	316.90
0.2	318.61	308.77	319.03
0.3	320.25	311.71	321.42
0.4	321.93	317.67	325.40
Average	319.15 ± 0.01	310.85 ± 0.01	320.68 ± 0.01

4.5 Summary

In summary, different poly(3,4-ethylenedioxythiophene) nanostructures namely, DBSA doped nanoparticles, SDS doped nanofibers and CSA doped nanotubes have been synthesized by self-assembly method with varying dopant concentration. High resolution transmission electron microscope reveals the formation of nanostructures (nanoparticles, nanofibers and nanotubes). The average diameters of nanoparticles are found to be 13 to 40 nm for 0.003M and 1M DBSA concentration, respectively. The average diameters of nanofibers for 0.03M and 1M SDS concentration are found to be 14 nm and 15.5 nm, respectively. The diameter of the nanotubes is observed to be increased with increasing CSA concentration. The average outer diameter of the nanotubes is found to be 65 nm and 101 nm for 0.001M and 1M CSA concentration, respectively. DBSA, SDS and CSA act as surfactants as well as functional dopants for the synthesis of different PEDOT nanostructures. Since the size of the micelle determines the diameter of the nanostructures, the size of micelle increases with increasing dopant concentration leading to the increase of diameter of nanostructures.

XRD analysis shows the semi-crystalline nature of PEDOT nanoparticles, nanofibers and nanotubes systems. Crystallite size is found to increase with increasing dopant concentration for all the PEDOT nanostructures as confirmed from HRTEM images. The degree of crystallinity is found to increase with increasing dopant concentration indicating the enhancement of ordering of polymer chains in the nanostructures resulting in increase in conductivity. Higher value of percentage of crystallinity (46.19 %) for 1M CSA doped PEDOT nanotubes lead to the higher room temperature conductivity as discussed in section 5.1 of Chapter 5. The Raman spectra of PEDOT nanoparticles and nanotubes show that the $C_\alpha=C_\beta$ symmetric stretching deformation band is shifted to lower wavenumber side with increasing dopant concentration. The red shifting of Raman band with increasing dopant concentration reveals the conformational transition from benzenoid to quinoid structure. The polymer chain has a helically twisted structure in the benzenoid configuration, whereas in the oxidized state, the polymer main chain has planar quinoid configuration and the planarity of the main chain increases with increasing quinoid configuration. The increase in linearity of the polymer chains with

increasing dopant concentration leads to enhancement of polymer chain ordering as confirmed from XRD analysis.

Thermogravimetric plots depict two step weight loss patterns for all the three PEDOT nanostructures, viz., nanoparticles, nanofibers and nanotubes. The thermal stability of all the nanostructures found to increase with increasing dopant concentration. PEDOT nanotubes doped with 1M CSA concentration exhibits relatively slower decomposition rate during the heating process, which is consistent with the degradation activation energy calculation. The higher thermal stability of 1M CSA doped PEDOT nanotubes can be attributed to the higher degree of crystallinity (46.19 %).

Chapter 5

Transport properties of poly(3,4-ethylenedioxythiophene) nanoparticles, nanofibers and nanotubes

This chapter deals with the transport properties of poly(3,4-ethylenedioxythiophene) nanoparticles, nanofibers and nanotubes. DC resistivity and magnetoresistance analyses have been performed to probe the charge transport properties and behavior of charge carriers under magnetic field. Finally, AC conductivity analysis has been carried out to get insight into the charge transport processes under alternating electric field.

5.1 Introduction

Conducting polymers are heterogeneous systems composed of partially ordered crystalline regions separated by disordered amorphous regions. The charge transport mechanism in conducting polymers is very complex and cannot be explained by using the concept of band theory of solids. However, rigorous experiments and theoretical study have been going on to gain an insight into the charge transport phenomena in such heterogeneous systems and it is commonly believed that disorder-induced localization plays the major role in determining the charge transport mechanism [143, 144]. As the metallic domain is surrounded by the amorphous region that has disordered or folded chains and the presence of these disordered chains can reduce the conductivity. The tunneling or hopping of the charge carriers may take place between the metallic islands through amorphous localized regions. The presence of structural disorder in conducting polymers has strong influence on the transport properties. The structural disorder in conducting polymers arises from the variations in the conjugation length, rotation and kinking of the polymer chains, van der Waals interactions with neighboring conjugated molecules and doping processes etc. [145, 258]. The disorder and one-dimensionality of polymer chains result in the localization of the electron wave function. The charge transport is dominated by hopping between localized states and

phonon-induced delocalization in the disordered regions or tunneling between the metallic islands, depending upon the morphology. Since, the disorder is at microscopic scale, it induces the localization of electronic wave-functions. The density of localized states near the Fermi level is finite and the temperature dependent conduction occurs via hopping of the charge carriers with variable activation energy and it is known as variable range hopping (VRH) conduction [259].

The application of external magnetic field has deep impact on charge transport mechanism because the field alters the wave-function. Magnetoresistance (MR) is a phenomenon that reflects the change of electrical resistance of a material under the application of external magnetic field. The MR observed in organic materials is related to the formation of excitons and caused by the trapping of charge carriers at triplet excitons [260]. Seeking new material system exhibiting large MR has driven important progress in both condensed matter physics and for different device applications. Compared with magnetic materials, research on MR effect of non-magnetic materials has two outstanding advantages. Firstly, large MR effect can be obtained, and secondly, the MR shows linear relationship with the applied external magnetic field without saturating even at very high magnetic field of mega gauss field [261].

In this chapter, an effort has been made to understand the charge transport behavior of different PEDOT nanostructures, namely dodecylbenzene sulfonic acid (DBSA) doped nanoparticles, sodium dodecyl sulfate (SDS) doped nanofibers and camphorsulfonic acid (CSA) doped nanotubes. The samples have been synthesized with varying dopant concentration for each nanostructure system. The details synthesis processes of different PEDOT nanostructures have been discussed in section 3.2 of Chapter 3. DC resistivity studies have been carried out in the temperature range of 5 – 300K. The isothermal MR analyses have been performed at different temperatures of 5, 10, 20, 30, 50, 100, 200 and 300K in the magnetic field ranging from 0-8 T. All the measurements have been performed during heating and cooling process and found almost similar behavior with small deviation. The standard deviations have been shown with error bars in the figures. The MR study shows a transition from positive to negative value with increasing temperature for all the nanostructured systems. The observed positive and negative values of MR have

been analyzed using wave-function shrinkage and quantum interference model, respectively. Moreover, the analysis of AC conductivity reveals the presence of correlated barrier hopping (CBH) charge transport under AC electric field.

5.2 Transport properties analysis of PEDOT nanoparticles, nanofibers and nanotubes

5.2.1 DC resistivity study

In conducting polymers based low mobility materials, the charge transport takes place via hopping process between neighboring localized sites. To investigate the charge transport mechanism in the PEDOT nanostructures (nanoparticles, nanofibers and nanotubes), the DC resistivity measurements have been carried out within the temperature range of 5 K $\leq T \leq$ 300 K. Figures 5.1(a, b & c) show the temperature dependent resistivity plots of PEDOT nanoparticles, nanofibers and nanotubes for different dopant (DBSA, SDS and CSA) concentrations. The temperature dependent resistivity shows semiconducting behavior in the entire measured temperature range. It is observed that resistivity decreases with increasing dopant concentration for all the nanostructured systems. The decrease in resistivity with increasing dopant concentration can be attributed to the formation of more defect states in the band gap which enhanced the hopping probability. At low doping concentration, the number of defect states is less in the band gap, so charge carriers have to jump longer distance which leads to smaller conductivity. However, with increasing dopant concentration, the number of defect states increases in the band gap as a result charge carriers can easily hop from one defect states to another leading to smaller resistivity i.e. higher conductivity. The room temperature (at 300K) resistivity for 1M doped PEDOT nanoparticles, nanofibers and nanotubes are 0.36 Ω cm, 0.07 Ω cm and 0.04 Ω cm, respectively. The smaller resistivity or higher conductivity in case of 1M CSA doped nanotubes suggests the presence of more aligned polymer chains resulting in larger mean free path of charge carriers. The smaller resistivity value for 1M CSA doped nanotubes can be corroborated with XRD result discussed in section 4.2.2 of Chapter 4.

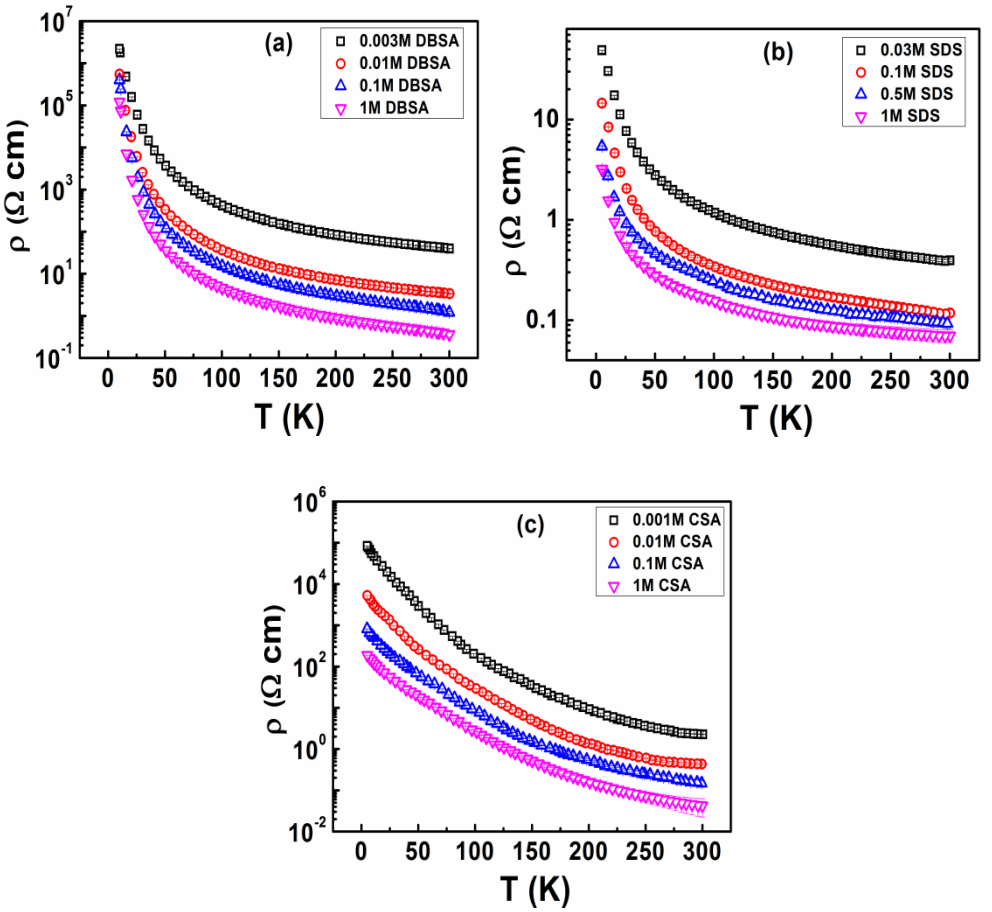

Figure 5.1: Temperature dependent resistivity plots of PEDOT (a) nanoparticles, (b) nanofibers and (c) nanotubes for different dopant concentrations. Error bars represent the standard deviation.

In disordered systems like conducting polymers the charge transport is taken place through hopping mechanism and their temperature dependence of resistivity is explained in terms of Mott's variable range hopping (VRH) model, according to which the resistivity can be expressed as [259]:

$$\rho(T) = \rho_o exp\left(\frac{T_{Mott}}{T}\right)^{\gamma} \tag{5.1}$$

where ρ_o is the resistivity at very high temperature ($T \rightarrow \infty$) and T_{Mott} is the characteristic Mott temperature, which is associated with the degree of localization of electronic wave-functions. The exponent γ = (1/1+d), where d = 1, 2 and 3 for one, two and three dimensional system, respectively.

In crystalline materials, the temperature dependence of resistivity gives the activation energy, and this method is used to differentiate materials from semiconductors and insulators. Metals and insulators have positive and negative value of reduced activation energy, respectively. In disordered materials like conducting polymers, the transport properties are strongly influenced by the disorder, which leads to charge carriers localization. For such systems, the insulating, critical and metallic behaviors can be distinguished with the help of temperature dependence of reduced activation energy (W) expressed as [165, 262]:

$$W = -\frac{d(ln\rho)}{d(lnT)} \tag{5.2}$$

The positive, zero and negative slopes of the log-log plot of *W vs. T* correspond to the metallic, critical and insulating regimes, respectively. The negative slope of *W vs. T* plots for all the nanostructured systems indicate the insulating nature of the samples. Furthermore, the magnitude of slope of *W vs. T* plot gives the value of γ, which determines the dimensionality of conduction mechanism.

Figures 5.2 (a, b & c) represent the log-log plot of *W vs. T* for all the PEDOT nanostructured systems. From the slope it has been observed that the values of γ lie in between 0.26 - 0.27 and 0.26-0.28 for PEDOT nanoparticles and nanofibers, respectively. For 1D, 2D and 3D VRH conduction mechanisms, the value of γ is 0.5, 0.33 and 0.25, respectively. The obtained values of γ are nearly equal to 0.25 for PEDOT nanoparticles and nanofibers, suggesting the presence of 3D VRH mechanism. However, from Fig. 5.2 (c), it is observed that for PEDOT nanotubes the *W vs. T* plots give two distinct slopes for all the CSA concentrations. The values of γ lie in between 0.23-0.25 above 10K and in the range of 0.47-0.50 below 10K, indicating a transition from 3D to 1D with lowering temperature. The conduction mechanism in nanostructured systems is greatly influenced by the dopant counter ion and morphology of the nanostructure. When a conducting polymer is doped, the charge carriers are generated and the dopant counter ions are incorporated into the system. The transition from Mott 3D to 1D VRH in PEDOT nanotubes with lowering temperature can be attributed to the presence of larger bulky CSA dopant anion in between polymer chains. Although, DBSA and SDS are large molecules but they don't have bulky cycloaliphatic ring as CSA. The presence of long alkyl chains in DBSA and SDS anions cannot restrict the twisting of polymer chains and charge

carriers can make inter-chain hopping easily leading to 3D VRH mechanism in nanoparticles and nanofibers. However, the presence of bulky cycloaliphatic ring in CSA hinders the overlapping of polymer chains and keep chains in a more expanded conformation. At low temperature, charge carriers have less thermal energy and they cannot make inter-chain hoping in PEDOT nanotubes due to absence of chain twisting and it leads to 1D VRH mechanism at low temperature (< 10K).

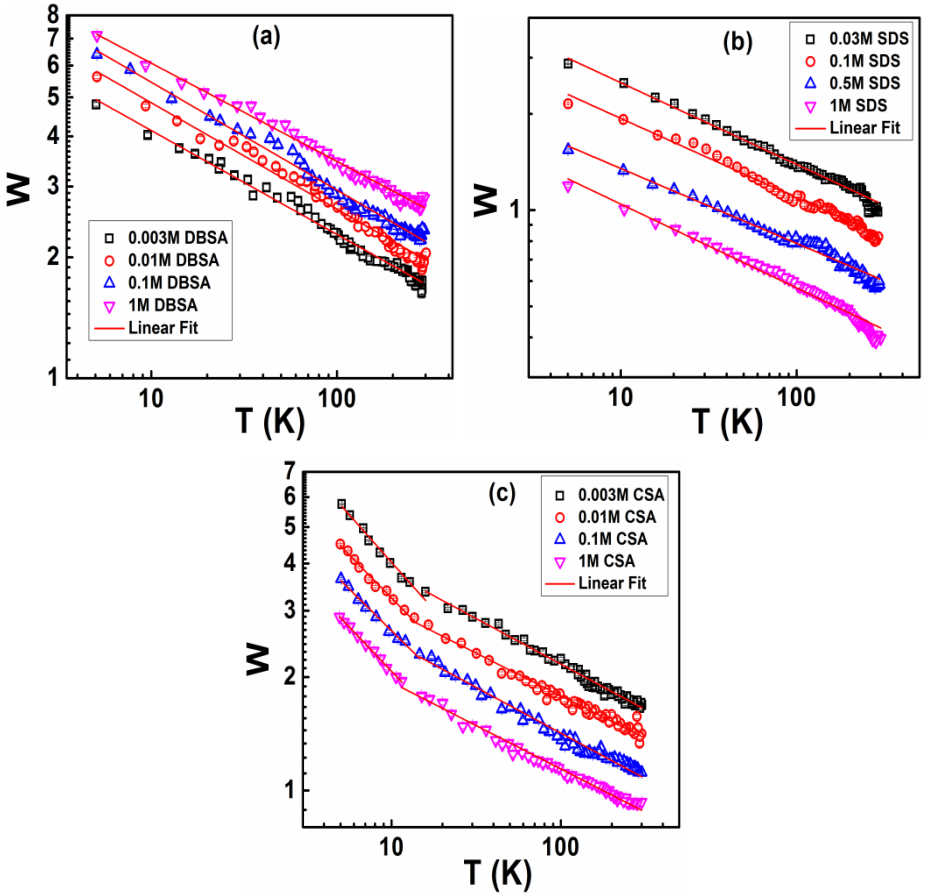

Figure 5.2: Log-log plots of *W vs. T* for PEDOT (a) nanoparticles, (b) nanofibers and (c) nanotubes for different dopant concentrations. Error bars represent the standard deviation.

Figures 5.3 (a, b & c) depict the lnρ *vs.* $T^{-1/4}$ plots of PEDOT nanoparticles, nanofibers and nanotubes for different dopant concentrations. From Figs. 5.3 (a & b), it is observed that the experimental data is well fitted according to the 3D VRH model. Whereas in case of nanotubes system (Fig. 5.3 (c)) below 10K the experimental results deviates from the fitted lines, which indicates the presence of other mechanism at low temperature. The characteristic Mott temperature, which

determines the effective thermally activated hopping energy separation between localized states, can be obtained from the slope of the fitted curve and are tabulated in Table 5.1. As the characteristic Mott temperature determines the hopping barrier height so the larger value of characteristic Mott temperature indicates the stronger localization of charge carriers in the system whereas smaller value indicates the weaker localization [263, 264].

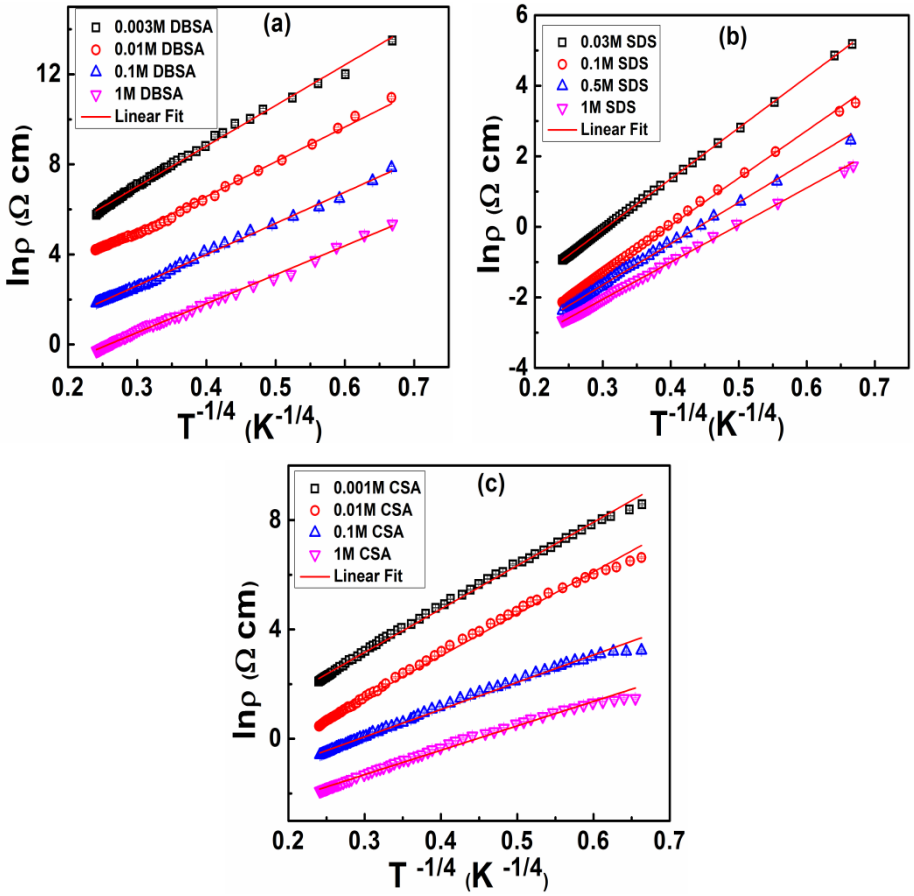

Figure 5.3: lnρ *vs.* $T^{-1/4}$ plot of (a) DBSA doped PEDOT nanoparticles, (b) SDS doped PEDOT nanofibers and (c) CSA doped PEDOT nanotubes at different dopant concentrations. In figure symbols are the experimental data and red solid lines are best linear fitted lines. Error bars represent the standard deviation.

Figure 5.4 depicts the lnρ *vs.* $T^{-1/2}$ plot of PEDOT nanotubes for different CSA concentrations. From Fig. 5.4, it is observed that the resistivity follows 1D VRH mechanism at low temperature ($\leq$ 10K) and it deviates with increasing temperature. The characteristics Mott temperatures below 10K for different dopant

concentrations have been calculated from the linear fitting of the experimental data and the obtained values are presented in Table 5.2.

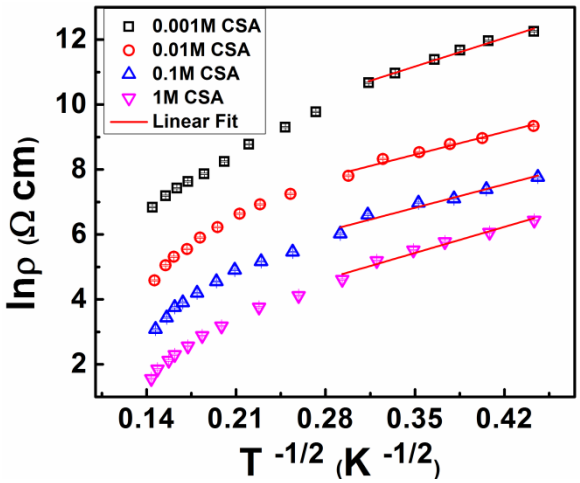

Figure 5.4: lnρ *vs.* $T^{-1/2}$ plot of PEDOT nanotubes with varying CSA concentration. In figure symbols are the experimental data and red solid lines are best linear fitted lines. Error bars represent the standard deviation.

The VRH model in presence of magnetic field can be expressed as [265]:

$$ln\left(\frac{\rho(B,T)}{\rho(0,T)}\right) = t_2\left(\frac{L_{loc}}{L_B}\right)^4\left(\frac{T_{Mott}}{T}\right)^{3/4} \quad (5.3)$$

where t_2 = 0.00248 and L_B (=$(\hbar/eB)^{1/2}$) is the magnetic length. The value of L_B at 8T magnetic field is 9 nm. Figure 5.5 (a, b & c) show the ln[ρ(B, T)/ρ(0, T)] *vs.* $T^{-3/4}$ plots of PEDOT nanoparticles, nanofibers and nanotubes for different dopant concentration. The values of localization length for different dopant concentrations have been calculated from the slopes of linear fitted lines and the calculated values are presented in Table 5.1. From the calculated values of L_{loc}, it is observed that localization length increases with increasing dopant concentration for all the nanostructured systems and it is attributed to the increase in polymer chains ordering in the nanostructures as confirmed from XRD analysis discussed in sub-section 4.2.2 of Chapter 4. The highest value of localization length in case of 1M CSA doped nanotubes leads to smaller resistivity i.e. highest conductivity.

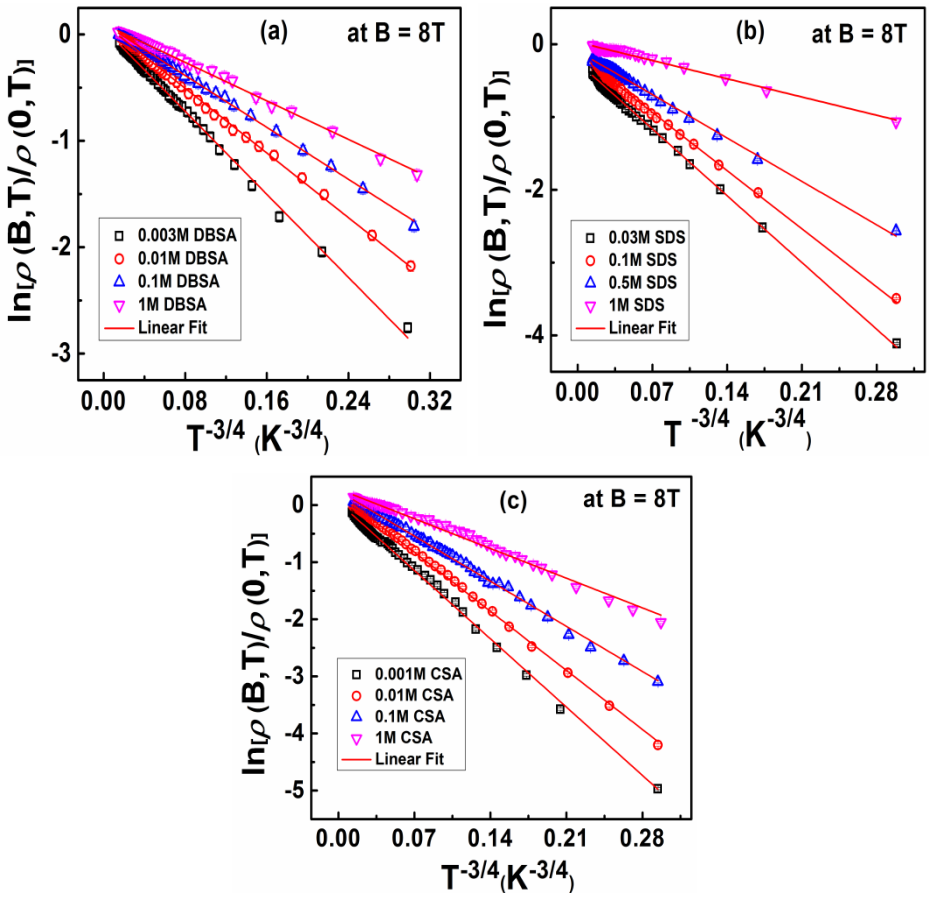

Figure 5.5: ln[ρ(B, T)/ρ(0, T)] *vs.* $T^{-3/4}$ plots of resistivity data at magnetic field 8 T for (a) DBSA doped PEDOT nanoparticles, (b) SDS doped PEDOT nanofibers and (c) CSA doped PEDOT nanotubes. In figure, symbols are the experimental data and red solid lines are best linear fitted lines. Error bars represent the standard deviation.

The transport parameters such as average hopping distance ($R_{hop,\ 3D}$ (for 3D) & $R_{hop,\ 1D}$ (for 1D)), density of states ($N(E_F)$) and charge carrier hopping energy ($\Delta_{hop,\ 3D}$ (for 3D) & $\Delta_{hop,\ 1D}$ (for 1D)) have been calculated using the following relations [266, 267]:

For Mott-3D VRH model,

$$R_{hop,\ 3D} = \left(\frac{3}{8}\right)\left(\frac{T_{Mott,\ 3D}}{T}\right)^{\frac{1}{4}} L_{loc} \tag{5.4}$$

$$T_{Mott,\ 3D} = \frac{16}{[L_{loc}^3 k_B N(E_F)]} \tag{5.5}$$

and

$$\Delta_{hop,\ 3D} = \frac{1}{4} k_B T \left(\frac{T_{Mott,\ 3D}}{T}\right)^{\frac{1}{4}} \tag{5.6}$$

For Mott-1D VRH model,

$$R_{hop,\ 1D} = \left(\frac{1}{4}\right)\left(\frac{T_{Mott,\ 1D}}{T}\right)^{\frac{1}{2}} L_{loc} \tag{5.7}$$

and

$$\Delta_{hop,\ 1D} = \left(\frac{1}{2}\right)\ k_B T \left(\frac{T_{Mott,\ 1D}}{T}\right)^{\frac{1}{2}} \tag{5.8}$$

The calculated values of transport parameters are presented in Table 5.1 and Table 5.2. From the calculated values presented in Table 5.1 and Table 5.2, it is observed that the average hopping distance and the average hopping energy decrease with increasing dopant concentration, whereas density of states increases. The decrease of average hopping distance and the average hopping energy can be attributed to the enhancement of hopping rate between the localized states leading to the smaller resistivity.

Table 5.1: *Transport parameters calculated from resistivity data for PEDOT nanoparticles, nanofibers and nanotubes.*

Sample name	$T_{Mott,\ 3D}$ **× 10^3(K)**	L_{loc} **(nm)**	$N(E_F)\times10^{18}$ **(cm^{-3} eV^{-1})**	$R_{hop,\ 3D}$ **(nm) at 300K**	$\Delta_{hop,\ 3D}$ **(meV) at 300K**
PEDOT nanoparticles					
0.003M DBSA	93.8	8.33	3.42	13.13	27.21
0.01M DBSA	56.2	8.61	5.17	11.95	23.94
0.1M DBSA	42.1	8.86	6.34	11.43	22.26
1M DBSA	35.5	9.28	6.54	11.47	21.33
PEDOT nanofibers					
0.03M SDS	42.9	10.38	3.86	13.46	22.38
0.1M SDS	35.2	10.41	4.67	12.85	21.29
0.5M SDS	25.2	10.86	5.75	12.33	19.58
1M SDS	16.4	11.16	8.14	11.38	17.59
PEDOT nanotubes					
0.001M CSA	67.9	10.18	2.59	14.80	25.09
0.01M CSA	31.3	11.39	4.01	13.65	20.67
0.1M CSA	14.2	12.31	7.02	12.11	16.96
1M CSA	9.2	12.65	9.93	11.17	15.23

Table 5.2: *Transport parameters calculated from resistivity data for PEDOT nanotubes at different CSA concentration.*

Sample name	$T_{Mott,\ 1D}$ **(K)**	$R_{hop,\ 1D}$ **(nm) at 5K**	$\Delta_{hop,\ 1D}$ **(meV) at 5K**
0.001M CSA	170	14.84	1.21
0.01M CSA	131	14.57	1.10
0.1M CSA	112	14.56	1.02
1M CSA	100	14.14	0.96

5.2.2 Magnetoresistance (MR) study

Magnetoresistance (MR) is the change in electrical resistance of material in response to an external applied magnetic field and it gives information about the dynamics of charge carriers defined as: $MR = \Delta\rho(B,T)/\rho(0,T) = [\rho(B,T) - \rho(0,T)]/\rho(0,T)$. Figures 5.6 (a, b & c) show the magnetic field dependent MR at different temperature for 0.003M, 0.01M and 1M DBSA doped PEDOT nanoparticles. For all the samples at low temperature, positive MR is observed and it makes a transition from positive to negative MR with increasing temperature. Moreover, with increasing dopant concentration, the negative contribution to the MR increases, whereas positive contribution to MR decreases. For better observation of crossover temperature, we have plotted the temperature variation of MR at 8T for 0.003M, 0.01M and 1M DBSA doped PEDOT nanoparticles and shown in Fig. 5.7. The figure clearly shows that with increasing dopant concentration the positive to negative crossover temperature decreases, whereas magnitude of negative MR increases. The high value of negative MR for 1M DBSA doped sample can be attributed to the decrease of charge carrier localization due to enhancement in polymer chains ordering as confirmed from XRD analysis.

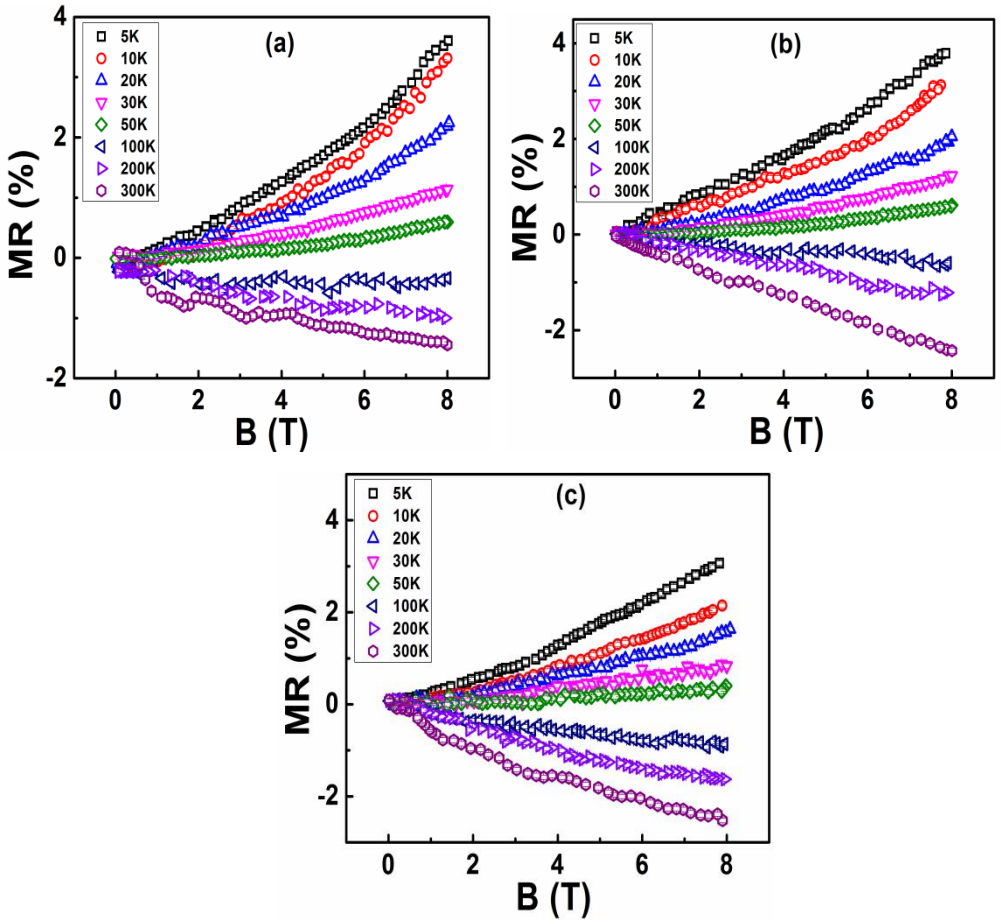

Figure 5.6: MR (%) *vs. B* of (a) 0.003M DBSA doped PEDOT nanoparticles, (b) 0.01M DBSA doped PEDOT nanoparticles and (c) 1M DBSA doped nanoparticles at eight different temperatures. Error bars represent the standard deviation.

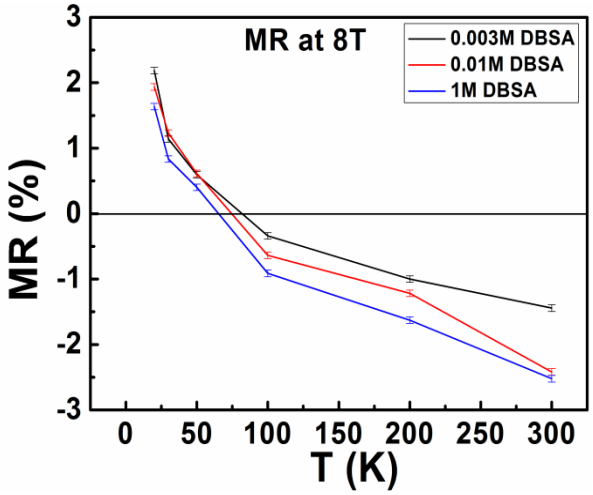

Figure 5.7: MR (%) (at B = 8T) *vs.* temperature plot for 0.003M, 0.01M and 1M DBSA doped PEDOT nanoparticles. Error bars represent the standard deviation.

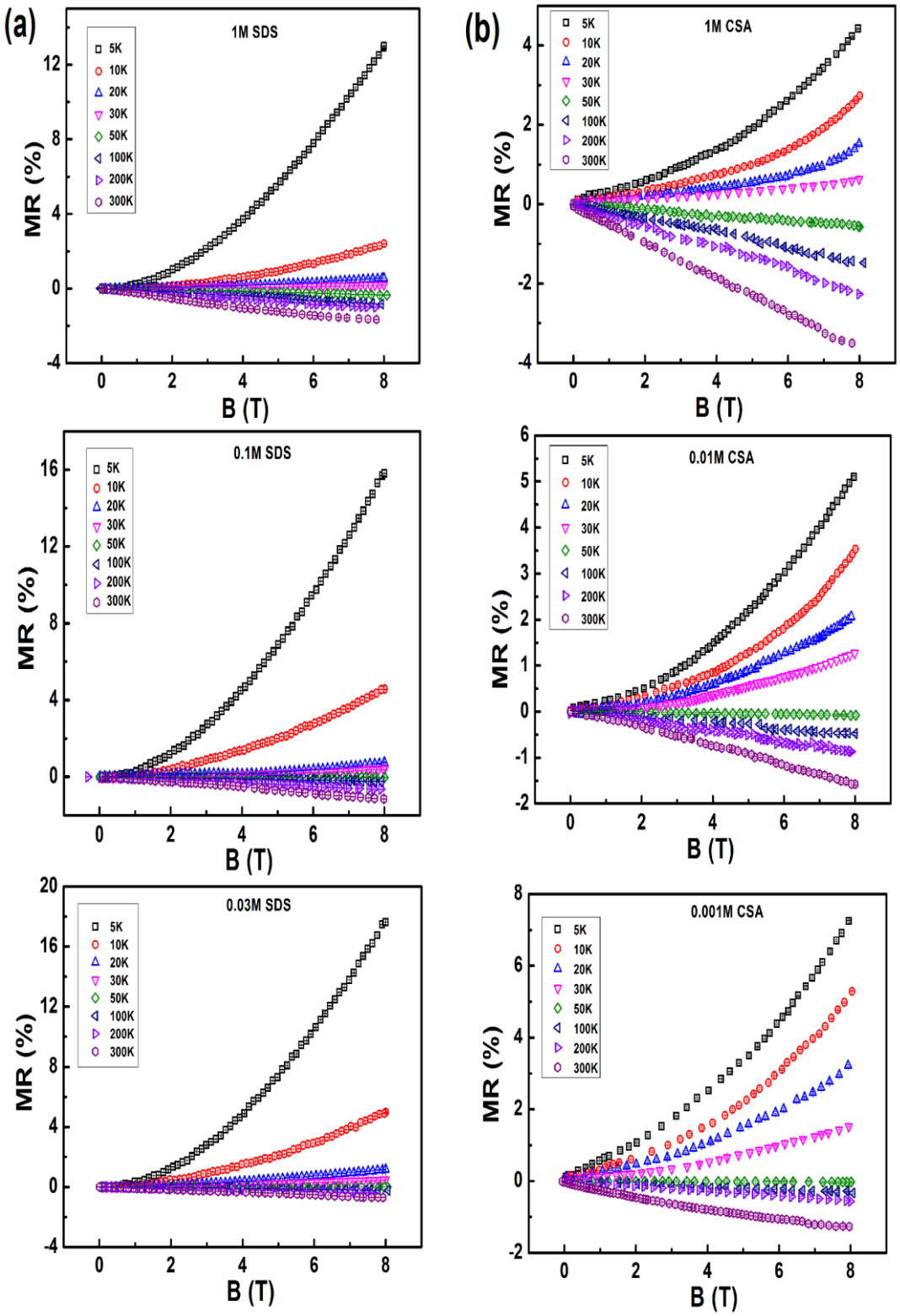

Figure 5.8: MR (%) *vs. B* of (a) PEDOT nanofibers and (b) PEDOT nanotubes at eight different temperatures. Error bars represent the standard deviation.

Figures 5.8 (a & b) show the variation of MR with magnetic field for SDS and CSA doped PEDOT nanofibers and nanotubes, respectively. Similar to that of PEDOT nanoparticles, in nanofibers and nanotubes also the MR values show transition from positive to negative with increasing temperature. The variation of MR at 8T with temperature for PEDOT nanofibers and nanotubes are shown in Fig. 5.9 (a & b). From Fig. 5.9(b), it is observed that the crossover temperature is minimum (≈ 32K) for 1M CSA doped sample. The smaller value of crossover temperature in case of 1M CSA doped nanotubes can be attributed to the higher ordering of polymer chains in the nanotubes and it can be corroborated with XRD analysis discussed in sub-section 4.2.2 of Chapter 4.

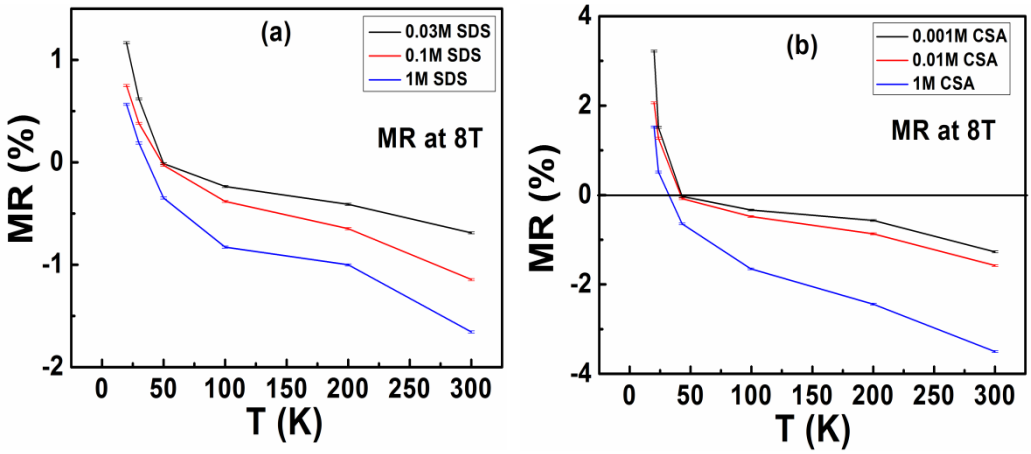

Figure 5.9: MR (%) (at B = 8T) *vs.* temperature plots of (a) SDS doped PEDOT nanofibers and (b) CSA doped PEDOT nanotubes at different dopant concentrations. Error bars represent the standard deviation.

The magnetoresistance (MR) in nonmagnetic materials arises due to the following reasons: (i) classical magnetoresistance, (ii) electron- electron (e-e) interaction, (iii) wave-function shrinkage and (iv) quantum interference. The mechanisms (i) to (iii) lead to positive magnetoresistance whereas mechanism (iv) gives rise to the negative magnetoresistance. Classical magnetoresistance results in positive MR due to the fact that the applied magnetic field causes the electrons to move around the periodic cyclotron. The magnitude of classical magnetoresistance is of the order of $\mu^2 B^2$. Since the mobility of charge carriers in conducting polymers is very low, the magnitude of MR will be very small, which rules out the validity of classical model for analyzing the positive magnetoresistance. The e-e interaction in

disordered system arises at low temperature, when the thermal energy k_BT is less than or comparable to Zeeman energy $\Delta E=g\mu_B B$, where g is the Lande's splitting factor and μ_B is the Bohr magneton. For inorganic material, g = 2, and ΔE=0.927 meV at a magnetic field of 8T, which is very much smaller than the applied thermal energy [268]. So this model is also not applicable for analyzing the observed data. The wave-function shrinkage model is applicable only when the magnetic relaxation length L_B is comparable to the hopping distance (R_{hop}). Since the calculated values of R_{hop} are comparable to L_B for all the PEDOT nanostructures systems so we can say that hopping mechanism is a suitable model to analyze the observed positive MR data [264]. Quantum interference model or weak localization model is generally used to analyze the negative MR data. It is based on back scattering processes due to constructive quantum interference.

The observed positive and negative values of MR have been analyzed by using the wave-function shrinkage and quantum interference model. According to wave-function shrinkage model under the application of magnetic field the electrons wave-function is squeezed in the transverse direction i.e., the spherical symmetric wave-functions without magnetic field transform into cigar-shaped under the application of magnetic field [264]. The transformation of electron wave-function from spherical to cigar-shaped under magnetic field leads to a sharp decrease in the overlap of the wave functions and it results the reduction in the hopping probability between two sites. The reduction in hopping probability leads to increase in resistivity i.e., positive MR at low temperature. According to wave-function shrinkage model positive MR is expressed as [269]:

$$MR = t_2 \frac{e^2 L_{loc}^4}{36\hbar^2} \left(\frac{T_{Mott}}{T}\right)^y B^2 \qquad (5.9)$$

where the exponent y = 3/4 for three-dimensional (3D) - VRH and y = 3/2 for one-dimensional (1D) – VRH. Figures 5.10 (a, b & c) depict the MR (%) *vs.* B^2 plots of the positive MR data of PEDOT nanoparticles, nanofibers and nanotubes for 1M dopant concentration. From Fig. 5.10, it is observed that MR increases linearly with B^2 below a characteristic field B_c, which decreases with decreasing temperature. As for example consider Fig. 5.10(a) in which at 30K, MR is linear with B^2 up to 8 T; at 20K, it is linear with B^2 up to 7.6 T; at 10K MR is linear with B^2 up to 7.2 T and at 5K the characteristic field decreases to 6.8 T. The decrease of linear dependence of

positive MR with B^2 with decreasing temperature can be ascribed to the increase in charge carrier localization. Since positive MR in hopping system arises due to the contraction of the charge carriers wave function and the subsequent reduction of hopping probability due to the increase in average hopping length (R_{hop}) at low temperature under magnetic field [270]. The decrease in linear dependence of positive MR with B^2 with lowering temperature results due to the increase of hopping length under magnetic field.

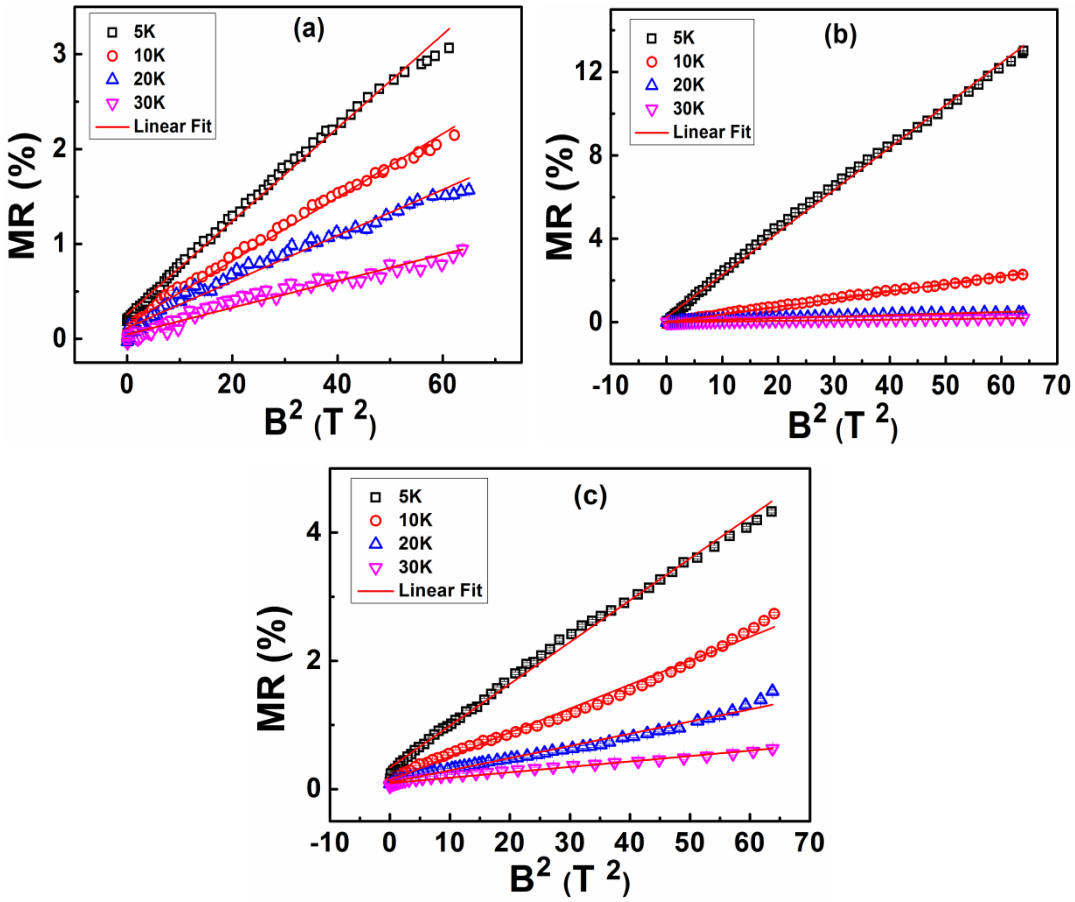

Figure 5.10: MR (%) *vs.* B^2 plots of the positive magnetoresistance data of (a) 1M DBSA doped PEDOT nanoparticles, (b) 1M SDS doped PEDOT nanofibers and (c) 1M CSA doped PEDOT nanotubes. Error bars represent the standard deviation.

The observed negative MR has been analyzed using the quantum interference model. According to this model, proposed by Nguyen, Spivak and Shklovskii (NSS) [271] the interference among different possible hopping paths results in the change in hopping probability between two sites. The conductivity is determined by the sum of all the possible hopping paths between two sites. The quantum interference

among different possible hopping paths under magnetic field leads to increase in conductivity (or decreased resistivity) i.e., negative MR [272]. According to NSS model the negative MR can be expressed as:

$$MR = -C_{sat}\frac{B}{0.7\left(\frac{8}{3}\right)^{3/2}\left(\frac{1}{L_{loc}^2}\right)\left(\frac{h}{e}\right)\left(\frac{T}{T_{Mott}}\right)^{3/8}} \qquad (5.10)$$

From Figs. 5.6 (a, b & c) and Figs. 5.8 (a & b) it is observed that negative MR varies linearly with magnetic field for all the nanostructures systems, which indicate that NSS model is more suitable to explain the observed negative MR. Moreover, the magnitude of positive MR is larger than that of negative MR, which indicates that quantum interference effect is much weaker than the wave-function effect.

5.2.3 AC conductivity analysis

An ideal insulating material does not contain free charge carriers and its conductivity is only due to the bound charges or the charge carriers hopping between localized sites, without contributing to the long range motion or DC conductivity. However, in a real system there are some free charge carriers that give rise to the DC conductivity, which does not contribute to the dielectric polarization. Hence the measured AC conductivity $\sigma_{tot}(\omega)$ will have contributions from both DC and AC conduction and can be expressed as [273]:

$$\sigma_{tot}(\omega) = \sigma_{dc} + \sigma(\omega) = \sigma_{dc} + A\omega^{s} \qquad (5.11)$$

Where σ_{dc} is the DC conductivity, A is a temperature dependent parameter and s is frequency exponent that lies between 0 and 1. Room temperature frequency dependent AC conductivity plots of PEDOT nanoparticles, nanofibers and nanotubes for different dopant concentration are shown in Figs. 5.11 (a, b & c). From the figures, it is observed that in the low frequency region the variation of $\sigma_{tot}(\omega)$ is small but increases sharply after a certain frequency with increasing frequency. The conductivity plots exhibit plateau at lower frequency and starts to increase at particular onset frequency known as cross-over critical frequency (ω_c) which increases with increasing dopant concentration. In the low frequency region below ω_c, the conductivity is frequency independent i.e. DC conductivity. At higher frequencies above ω_c the conductivity follows the power low behavior. The

frequency independent conductivity below the cross-over frequency is contributed by the free charge carriers available in the system whereas the frequency dependent conductivity at high frequency due to the trapped charges that are activated at higher frequencies [274]. The cross-over critical frequency shifts towards higher frequency side with increasing dopant concentration and it can be attributed to the increase in DC conductivity contribution due to increase of free charge carries at higher dopant concentration. With increasing dopant concentration due to the incorporation of dopant anions in between the polymer chains reduces the charge trapping centers and leading to the increase in charge carrier's participation in the conduction process.

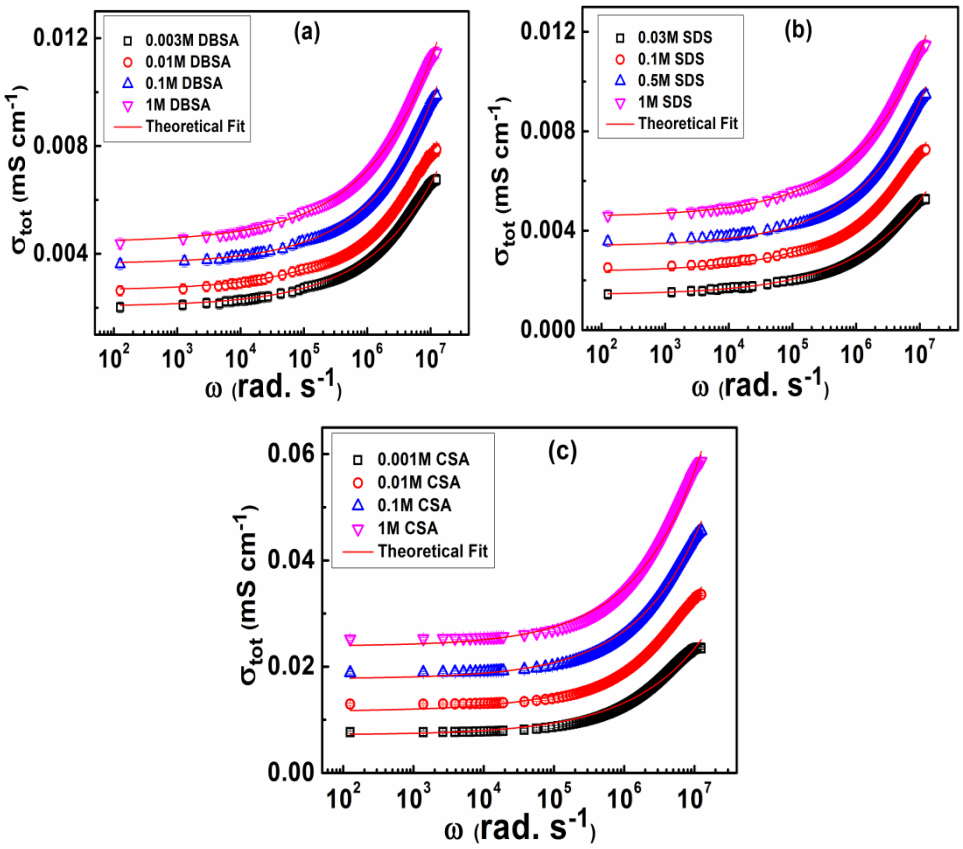

Figure 5.11: Room temperature frequency dependent AC conductivity plots of (a) DBSA doped PEDOT nanoparticles, (b) SDS doped PEDOT nanofibers and (c) CSA doped PEDOT nanotubes for different dopant concentrations. In Figs. Symbols are the experimental data and red solid lines are the fitted lines according to eq. (5.11). Error bars represent the standard deviation.

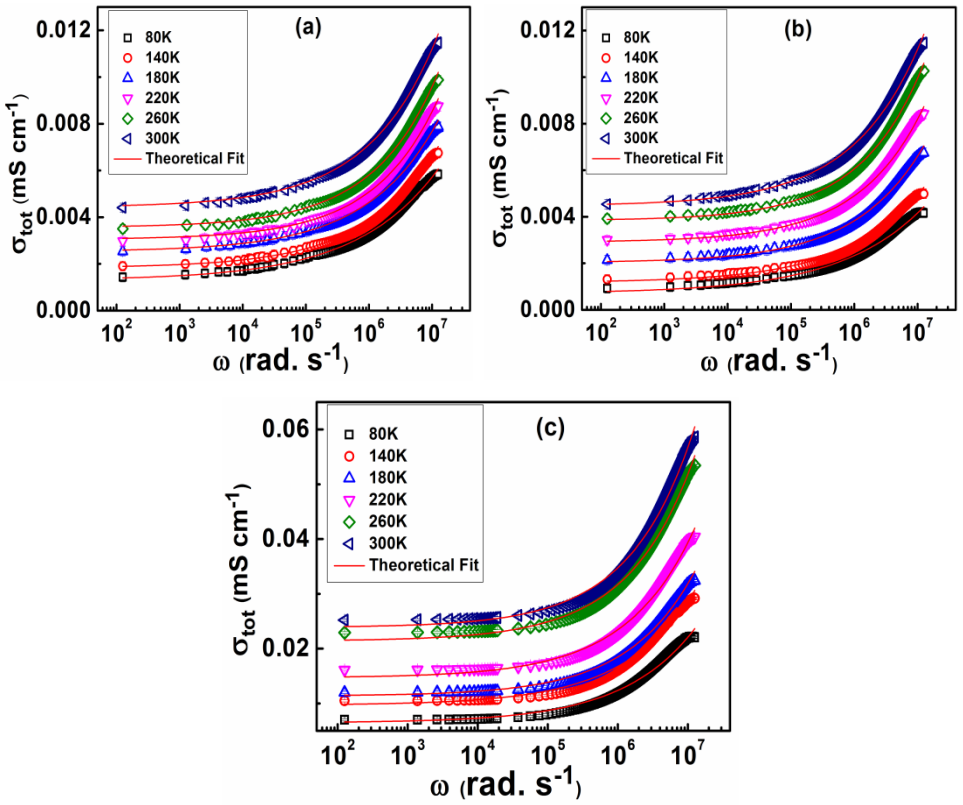

Figure 5.12: Frequency dependent AC conductivity plots of (a) 1M DBSA doped PEDOT nanoparticles, (b) 1M SDS doped PEDOT nanofibers and (c) 1M CSA doped PEDOT nanotubes at different temperature. In Figs. symbols are the experimental data and red solid lines are the fitted lines according to eq. (5.11). Error bars represent the standard deviation.

Figures 5.12 (a, b & c) depict the frequency dependent AC conductivity plots of PEDOT nanoparticles, nanofibers and nanotubes at different temperatures for 1M DBSA, 1M SDS and 1M CSA concentration, respectively. From the temperature dependent AC conductivity plot, it is observed that AC conductivity increases with increasing temperature. In disordered system like conducting polymers the charge carries are strongly trapped and due to low thermal energy of charge carriers at low temperature, they cannot make hop between localized sites. With increasing temperature, the charge carriers can hop to neighboring sites due to increase of thermal energy and form a continuous network, which allows the charge carriers to travel through the entire physical dimension of the samples resulting in electrical conduction [171].

In disordered systems, the microscopic conduction is governed by two distinct processes: the classical hopping and quantum mechanical tunneling of the charge carriers over a potential barrier between two energetically favorable randomly distributed localized sites. The mechanism responsible for the charge transport in such systems can be understood by study the nature of temperature dependence of the frequency exponent *s* [275]. Different theoretical models have been proposed to explain the obtained experimental results of AC conductivity for disordered systems. According to quantum mechanical tunneling (QMT) model [276], the exponent *s* is independent of temperature. In the overlapping large polaron-tunneling (OLPT) model [277], the exponent *s* decreases to a minimum value and then increases with increasing temperature. The small polaron (SP) model [278] is associated with the increase in *s* with increasing temperature indicating the activated behavior of polarons, which is independent of inter-site separation. In the correlated barrier-hopping (CBH) model [279], the frequency exponent *s* decreases with increasing temperature indicating the thermally activated behavior of charge carriers over the barrier between two sites having own columbic potential wells. The temperature dependence arises from the correlation between barrier height and inter-site separation. In order to understand the frequency dependent charge transport mechanism in these systems, the exponent *s* at different temperature is evaluated by fitting the experimental results according to eq. (5.11). In Figs 5.11 (a, b & c) and Figs. 5.12 (a, b & c) the symbols are the experimental results and red solid lines are best fitted line according to eq. (5.11). The obtained values of *s* from the fitted curves are tabulated in Table 5.3 and Table 5.4. For better observation of variation of frequency exponent *s* with temperature for 1M DBSA, 1M SDS and 1M CSA doped PEDOT nanostructures is shown in Fig. 5.13. From Fig. 5.13, it is observed that *s* decreases with increasing temperature for all nanostructured systems, which indicates the presence of correlated barrier hopping (CBH) charge transport mechanism in the synthesized PEDOT nanoparticles, nanofibers and nanotubes systems.

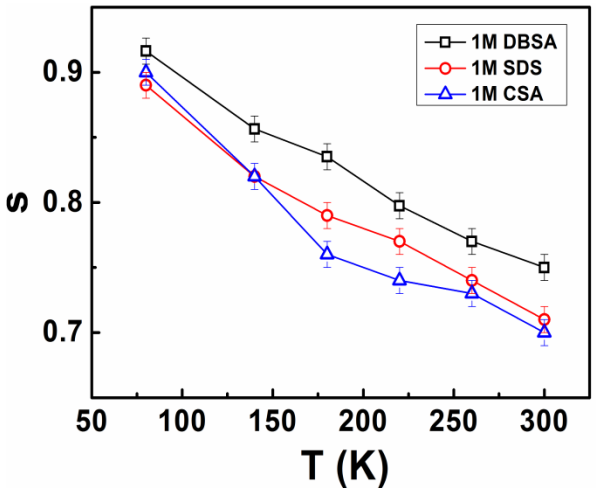

Figure 5.13: Frequency exponent *vs.* temperature plot of 1M DBSA, 1M SDS and 1M CSA doped PEDOT nanoparticles, nanofibers and nanotubes, respectively. Error bars represent the standard deviation.

Table 5.3: *Frequency exponent (s) at different temperature for 1M DBSA, 1M SDS and 1M CSA doped PEDOT nanoparticles, nanofibers and nanotubes, respectively.*

Temperature (K)	**1M DBSA doped PEDOT nanoparticles**	**1M SDS doped PEDOT nanofibers**	**1M CSA doped PEDOT nanotubes**
	***s* (±0.01)**	***s* (±0.01)**	***s* (±0.01)**
80	0.92	0.89	0.90
140	0.86	0.82	0.82
180	0.84	0.79	0.76
220	0.80	0.77	0.74
260	0.77	0.74	0.73
300	0.75	0.71	0.71

Table 5.4: *Transport parameters calculated from AC conductivity vs. frequency plots for PEDOT nanoparticles, nanofibers and nanotubes at different dopant concentrations.*

Sample name	***s* (±0.01) at 300K**	**W_M (±0.01) (eV) at 300K**
PEDOT nanoparticles		
0.003M DBSA	0.85	1.03
0.01M DBSA	0.81	0.81
0.1M DBSA	0.77	0.68
1M DBSA	0.75	0.62
PEDOT nanofibers		
0.03M SDS	0.82	0.86
0.1M SDS	0.76	0.65
0.5M SDS	0.73	0.58
1M SDS	0.71	0.54
PEDOT nanotubes		
0.001M CSA	0.83	0.91
0.01M CSA	0.75	0.62
0.1M CSA	0.72	0.55
1M CSA	0.7	0.52

In CBH model, the two sites are separated by a distance with an associated Columbic potential well. According to this model, the frequency exponent *s* at a given frequency and temperature is given by [280]

$$s = 1 - \frac{6k_BT}{[W_M + k_BTln\omega\tau_c]} \qquad (5.12)$$

where W_M is the binding energy, k_B is Boltzmann constant and τ_c is the characteristic relaxation time, which is of the order of an atomic vibrational period, $\tau_c \approx 10^{-13}$ s. At low temperature for large values of W_M/k_BT, eq. (5.12) takes the form [281]:

$$1 - s = \frac{6k_B T}{W_M} \tag{5.13}$$

The values of W_M for PEDOT nanoparticles, nanofibers and nanotubes for different dopant concentration are calculated by using eq. (5.13) at 300K and calculated values are presented in Table 5.4. From the Table 5.4, it is observed that the value of W_M decreases with increasing dopant concentration for all the three PEDOT nanostructured systems. The decrease in binding energy with increasing dopant concentration can be attributed to the formation of defect states in the band gap that facilitates the hoping of charge carries between the localized states.

5.2.3.1 Scaling of AC conductivity

The studies of dynamic processes involving charge carriers in disordered materials have received intense scientific significance in the past several years. The temperature dependence study of conductivity spectra at different temperatures in disordered materials lead to a scaling law known as the time-temperature superposition principle (TTSP) [282]. The ability to scale different data sets so as to collapse all to one common master curve indicates that the process can be explained by a common physical mechanism. According to Ghosh model [283], the AC conductivity follows a scaling law of the form:

$$\left(\frac{\sigma_{tot}(\omega)}{\sigma_{dc}}\right) = 1 + \left(\frac{\omega}{\omega_c}\right)^s \tag{5.14}$$

The scaling of AC conductivity spectra at different temperatures for 1M DBSA, SDS and CSA doped PEDOT nanoparticles, nanofibers and nanotubes are depicted in Figs. 5.14 (a, b & c), where the conductivity axis is scaled by DC conductivity (σ_{dc}) and the frequency axis by cross-over frequency (ω_c). From Figs. 5.14 (a, b & c), it is observed that all the curves for different temperatures superimpose over one another. The scaling behavior of AC conductivity suggests that the charge carriers' relaxation dynamics is independent of temperature in the conductivity formalism.

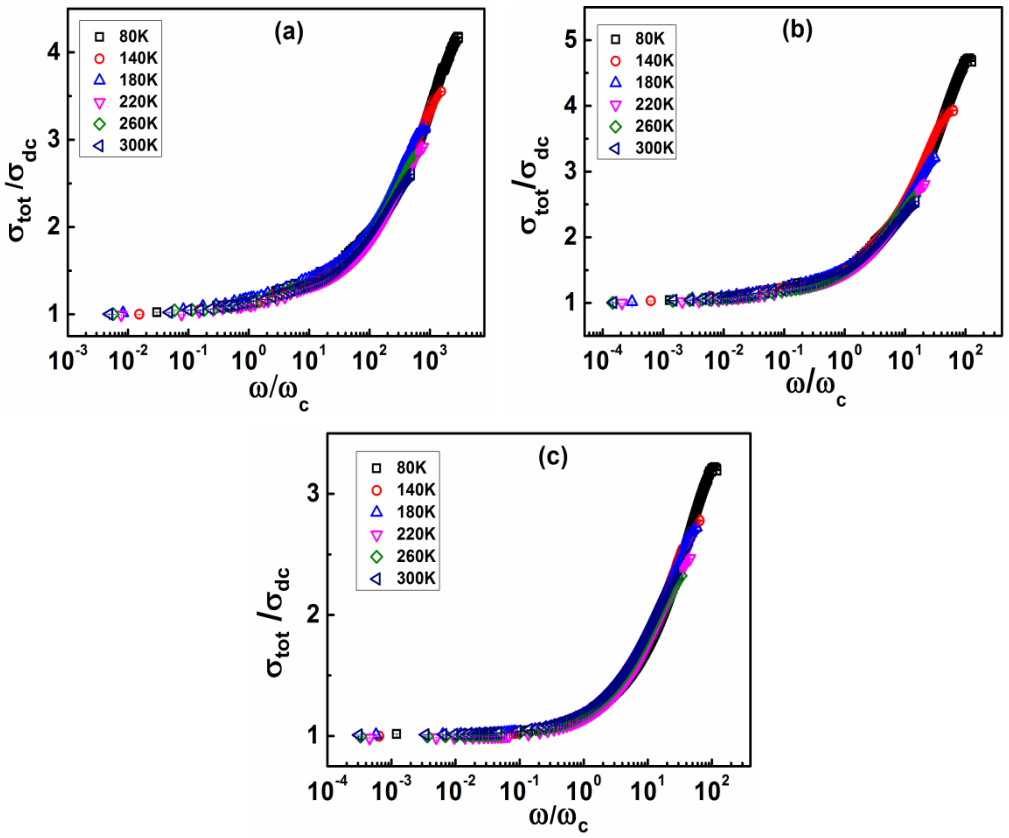

Figure 5.14: Scaling of AC conductivity spectra at different temperature for 1M (a) DBSA doped nanoparticles, (b) SDS doped nanofibers and (c) CSA doped nanotubes. Error bars represent the standard deviation.

5.3 Summary

In summary, DC resistivity, magnetoresistance and AC conductivity measurements have been carried out to get insight into the charge transport mechanism in low dimensional PEDOT nanostructures, viz., DBSA doped PEDOT nanoparticles, SDS doped PEDOT nanofibers and CSA doped PEDOT nanotubes.

For all the nanostructured systems the temperature dependent resistivity shows semiconducting behavior i.e., resistivity decreases with increasing temperature in the entire measured temperature range of 5 – 300 K. It has been observed that dopant type and dopant concentration has significant effect on charge transport mechanism and resistivity. The decrease in resistivity with increasing dopant concentration can be ascribed to the introduction of traps in the HOMO-

LUMO gap, which helps in enhancing the hopping rate. At low doping concentration the number of defect states is less in the band gap, and the charge carriers hop to a longer distance which reduces the hopping probability. With increasing doping level, the inter-chain hopping probability increases due to the increase in interstitial dopant counter-ions, which serve as defect sites. Because of the local lowering of the potential energy for the charge carriers at the dopant ions, the wave-function overlapping increases between the two chains leading to higher hopping probability. The negative slope of *W vs. T* plots indicates that the synthesized samples fall in the insulating regime of the metal-insulator transition. The charge transport in DBSA doped nanoparticles and SDS doped nanofibers follow 3D VRH mechanism, whereas a crossover from 3D VRH mechanism to 1D VRH mechanism is observed in CSA doped nanotubes below 10K. The presence of bulky cycloaliphatic ring in CSA anion restricts the twisting of polymer chains while it fills up the space between polymer chains. At low temperatures (< 10K), the charge carriers have less thermal energy as a result they cannot make inter-chain hopping due to the absence of chain twisting leading to 1D VRH mechanism in case of CSA doped nanotubes. However, the long alkyl chains in DBSA and SDS cannot restrict the twisting of polymer chains, which leads to random orientation of polymer chains giving rise to 3D VRH mechanism in nanoparticles and nanofibers. The decrease in characteristic Mott temperature with increasing dopant concentration can be attributed to the enhancement of polymer chains ordering in the nanostructures (nanoparticles, nanofibers and nanotubes), which is corroborated with XRD results (discussed in section 4.2.2 of Chapter 4). The average hopping distance and average hopping energy decrease with increasing dopant concentration for all the nanostructured systems which results in the enhancement of hopping rate between the localized states leading to smaller resistivity. The smallest room temperature resistivity of 0.043 Ω cm for 1M CSA doped PEDOT nanotubes can be attributed to the reduction of disorderness in the nanotubes as confirmed from XRD analysis.

The isothermal magnetoresistance (MR) has been measured at eight different temperatures (5, 10, 20, 30, 50, 100, 200 & 300K) in the magnetic field range of 0 – 8 T. The MR values show a transition from positive to negative with increasing temperature for all the nanostructures. The observed positive and negative MR has been analyzed using wave-function shrinkage model and quantum interference

model, respectively. The positive to negative cross-over temperature is found to be decreased with increasing dopant concentration for all the nanostructures and it can be attributed to the enhancement of polymer chains ordering in the nanostructures at higher dopant concentration as confirmed from XRD analysis discussed in section 4.2.2 of Chapter 4. The smaller magnitude of negative MR than that of positive MR suggests that quantum interference effect is much weaker than wave-function shrinkage effect. The high value of negative MR in case of 1M CSA doped PEDOT nanotubes indicates the higher delocalization of charge carriers, which gives rise to smaller resistivity.

The AC conductivity spectra exhibit plateau at lower frequency and starts to increase from a particular frequency known as cross-over critical frequency (ω_c) which increases with increasing dopant concentration as well as temperature. The frequency region of constant conductivity extends to higher frequencies with increasing dopant concentration and temperature indicating the enhancement of dc conductivity. AC conductivity study displays significant enhancement in the conductivity with increasing dopant concentration for all the nanostructures. With increasing dopant concentration the number of free charge carriers increases leading to the increase in frequency independent conductivity i.e. DC conductivity. The decrease in frequency exponent *s* with increasing temperature reveals that the correlated barrier hopping (CBH) is the dominating charge transport mechanism in the nanostructured systems under AC electric field. The scaling behavior of AC conductivity at different temperatures suggests that the conduction mechanism of charge carriers is temperature independent.

Chapter 6

Dielectric properties and charge carrier relaxation study of poly(3,4-ethylenedioxythiophene) nanoparticles, nanofibers and nanotubes

This chapter focuses on the charge carrier polarization and relaxation dynamic processes in poly(3,4-ethylenedioxythiophene) nanoparticles, nanofibers and nanotubes under the application of alternating electric field. Dielectric permittivity formalism analysis has been carried out to understand the polarization mechanism. The charge carrier relaxation dynamics has been investigated through the framework of impedance and modulus formalisms. The scaling of impedance and modulus formalisms has been performed to observe the dynamic behavior of charge carriers at different temperatures.

6.1 Introduction

In recent years, conducting polymers nanostructures such as nanoparticles, nanowires, nanotubes, nanoneedles and nanofibers are gaining increasing attention among the researchers worldwide owing to their interesting electronic and optical properties, chemical stability, environmentally friendly and promising technological applications in different fields [284]. Nanostructure provides higher surface to volume ratio and exhibit different chemical, physical, dielectric and electronic properties than that of bulk counterparts [285]. They are also expected to play a crucial role as both interconnect and develop functional units in fabricating electronic, optoelectronic and electrochemical devices of nanoscale dimension [284]. Developing a deeper insight into the charge transport mechanisms in conducting polymers has given rise to intensive investigations on their transport properties. The disorder-induced localization plays a pivotal role in determining the transport properties of conducting polymers. Common factors which create the disorder in conducting polymers are random structures, inhomogeneous doping and synthesis processes [286, 287]. Another difficulty in chain like polymeric material is the

competition between intra-chain and inter-chain processes [288]. The charge transport mechanism in conducting polymers has been widely studied using different experimental techniques such as AC conductivity [289], dielectric relaxation [290] and photoconductivity [291]. Most of the dynamical features e.g. polarization of dipoles in condensed matter is accompanied by the motion of charge carriers. Therefore, dielectric techniques are used to quantify the response of a material to a field induced perturbation [292]. Impedance spectroscopy is a nondestructive tool to characterize the electrical properties of materials under the application of an AC signal in which the overall material behavior is governed by the number of strongly coupled processes. This technique is used to investigate the electrical properties such as dielectric behavior and charge carrier relaxation characteristics of solid, liquid or amorphous materials [293, 294]. An advantage of impedance spectroscopy over other techniques is the possibility of using a wider range of frequency. Moreover, dielectric measurements are extremely sensitive to small changes in material properties. The dielectric parameters associated with the relaxation processes are of particular significance in conducting polymers. The dielectric relaxation is sensitive to the motion of charge carriers and dipoles in the polymer. In polymeric composite materials, interfacial polarization is always present because of the fillers or other impurities present in the system, which makes the system heterogeneous. The free charge carriers trapped in the insulating matrix, conductive filler, dopant ions and/or other impurities give rise to the interfacial polarization due to difference of dielectric constant between them. The dielectric relaxation occurring due to the interfacial polarization gives information about the electrical transport properties of the system [295].

In the present thesis work we have synthesized three different PEDOT nanostructures namely, dodecylbenzene sulfonic acid (DBSA) doped nanoparticles, sodium dodecyl sulfate (SDS) doped nanofibers and camphorsulfonic acid (CSA) doped nanotubes. For each nanostructured system four different samples were prepared by systematically varying the dopant concentration.

This chapter includes the investigation of dielectric and charge carriers' relaxation dynamics of PEDOT nanoparticles, nanofibers and nanotubes through the framework of dielectric, impedance and modulus formalisms. The dielectric measurements have been performed in the temperature and frequency range of 80 -

300K and 20Hz - 2MHz, respectively. All the measurements have been performed during heating and cooling process and found almost similar behavior. The standard deviations have been shown with error bar in the figures. Different parameters like relaxation time (τ_{max}), activation energy (E_a) and geometric shape parameters (α_{hn} and β_{hn}) have been determined from the experimental results.

6.2 Dielectric properties analysis of PEDOT nanoparticles, nanofibers and nanotubes

6.2.1 Dielectric permittivity formalism

Dielectric properties describe the ability of an electrical medium to be polarized by an applied alternating electric field. The dielectric relaxation results due to the movement of dipoles and electric charges under application of AC electric field. The dielectric parameter as a function of frequency is described by the complex permittivity (ε^*) in the form [284]:

$$\varepsilon^*(\omega) = \varepsilon'(\omega) - i\varepsilon''(\omega) \quad (6.1)$$

where $\varepsilon'(\omega)$ and $\varepsilon''(\omega)$ are the real and imaginary parts of the complex permittivity $\varepsilon^*(\omega)$, respectively. The real part of dielectric permittivity $\varepsilon'(\omega)$ is the measure of energy stored and $\varepsilon''(\omega)$ is a measure of energy dissipated per cycle in the dielectric material under applied AC electric field. Figures 6.1 (a, b & c) show the variation of real part of dielectric permittivity ($\varepsilon'(\omega)$) of PEDOT nanostructures (nanoparticles, nanofibers and nanotubes) at room temperature for different dopant concentrations. From Figs. 6.1 (a, b & c) it is observed that $\varepsilon'(\omega)$ increases towards lower frequencies for all the nanostructured systems. The high values of $\varepsilon'(\omega)$ at low frequency ($<10^4$ Hz) can be attributed to the building up of free charges at the interfaces between the sample and electrode resulting in space-charge polarization [296]. There are two major polarization mechanisms in polymeric materials that contribute to the dielectric permittivity: (1) polarization due to charge migration and (2) polarization due to orientation of permanent dipoles. There are no permanent dipoles in conducting polymers. The charge carriers in these polymers are strongly trapped and the localized short range motion of these carriers under the application of external alternating electric field can act as 'effective' electric dipole [297]. In the case of disordered materials, like conducting polymers the hopping of charge carriers

from one site to another is possible only when the polarization cloud around the charge also follows it. The mutual movement of charge carriers and the polarization cloud requires an electric relaxation time [284]. The dielectric relaxation in presence of AC electric field is a result of charge carrier hopping among the available localized sites. At low frequencies ($\omega << 1/\tau$, τ is the relaxation time), the induced dipoles follow the applied field and they get sufficient time to move over macroscopic distances and build up at the interfaces between the sample and the electrodes within a half cycle of the applied AC field, resulting in high value of the dielectric permittivity [298]. With the increase in frequency ($\omega > 1/\tau$), the dipoles start to lag behind the applied field leading to decrease in the value of $\varepsilon'(\omega)$. At very high frequencies ($\omega >> 1/\tau$), the dipoles no longer follow the applied electric field and $\varepsilon'(\omega)$ approaches a constant value at about 10^6 Hz.

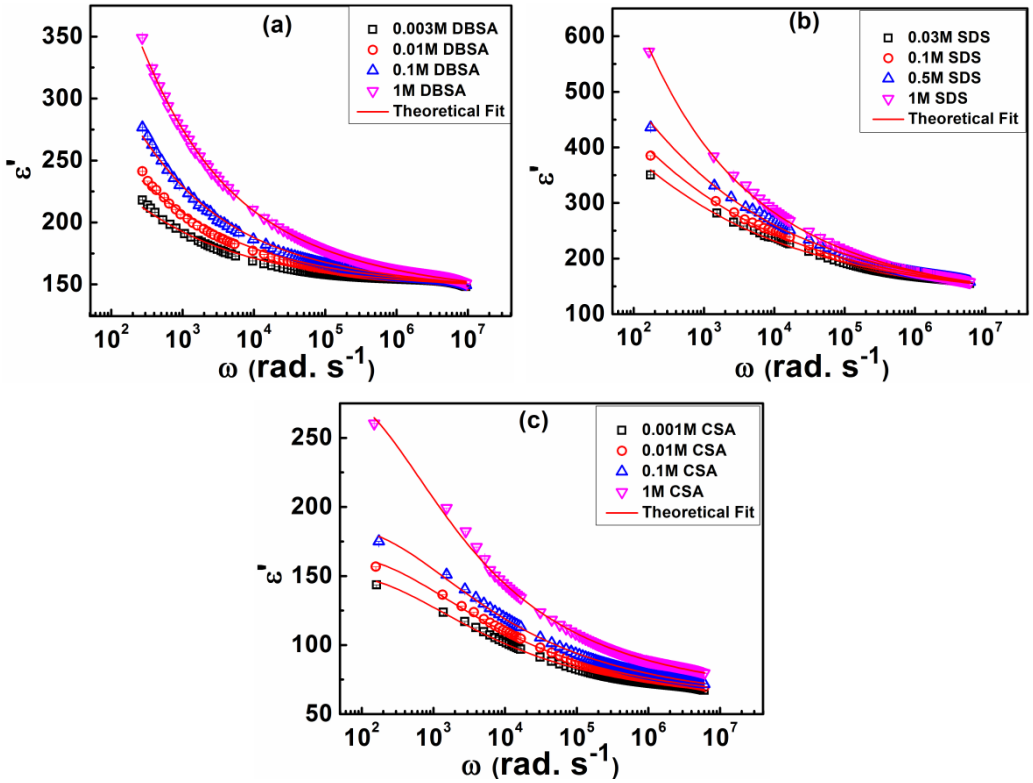

Figure 6.1: Variation of real part of dielectric permittivity ($\varepsilon'(\omega)$) of PEDOT (a) nanoparticles, (b) nanofibers and (c) nanotubes at room temperature for different dopant concentrations. In figure symbols indicate the experimental data and the red solid lines represent the theoretical best fit obtained from Eq. (6.3). Error bars show the standard deviation.

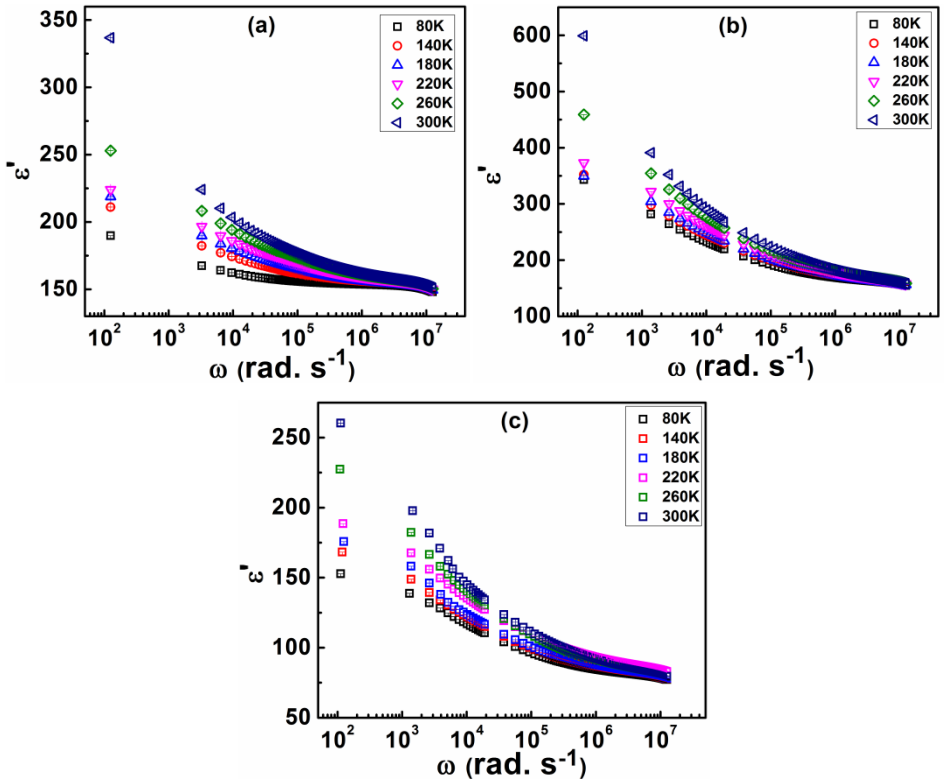

Figure 6.2: Variation of real part of dielectric permittivity ($\varepsilon'(\omega)$) of PEDOT (a) 1M DBSA doped nanoparticles, (b) 1M SDS doped nanofibers and (c) 1M CSA doped nanotubes at different temperatures. Error bars show the standard deviation.

Figures 6.2(a, b & c) depict the frequency dependent $\varepsilon'(\omega)$ plots at different temperatures for 1M DBSA, 1M SDS and 1M CSA doped PEDOT nanoparticles, nanofibers and nanotubes, respectively. From Figs. 6.2, it is observed that $\varepsilon'(\omega)$ increases with increasing temperature for all the nanostructured systems. At higher temperature, the dipoles have sufficient thermal energy to orient themselves in the direction of the applied field, which leads to high values of $\varepsilon'(\omega)$ [299]. The high value of dielectric constant at high temperature arises due to the increase of total polarization arising from induced dipoles and trapped charge carriers which are activated at higher temperatures. Increasing in temperature mobilizes the polymer chains, reducing pinning and leads to greater number of charge carrier participation in the relaxation process for a given frequency resulting in higher value of dielectric constant. At low temperature, the charge carriers have low thermal energy and they cannot orient themselves in the direction of the applied field giving a weak contribution to the polarization and resulting in smaller value of ε' [300]. However,

the increase in dielectric permittivity is more pronounced at lower frequencies than that at the higher frequencies.

The complex permittivity according to Havriliak-Negami (HN) equation over a wide range of frequency is expressed as [301]:

$$\varepsilon^* = \varepsilon_\infty + \frac{\Delta\varepsilon}{[1 + (i\omega\tau_{hn})^{1-\alpha_{hn}}]^{\beta_{hn}}} \tag{6.2}$$

where ε_∞ is the dielectric permittivity when ($\omega\rightarrow\infty$), $\Delta\varepsilon$ = (ε_s- ε_∞) is the dielectric strength and τ_{hn} is the relaxation time. α_{hn} ($0 \leq \alpha_{hn} < 1$) and β_{hn} ($0 \leq \beta_{hn} \leq 1$) are the geometric shape parameters defining symmetrical and asymmetrical distribution, respectively. The parameters α_{hn} = 0 and β_{hn} = 1 indicate the Debye-type relaxation and β_{hn} = 1 and $0 \leq \alpha_{hn} \leq 1$ indicate the Cole-Cole type relaxation. The Cole-Davidson model with an asymmetrical distribution of relaxation times follows for α_{hn} = 0 and $0 \leq \beta_{hn} \leq 1$. The parameter β_{hn} is a quantity describing the chain connectivity and α_{hn} is related to the local density fluctuations [302].

The real and imaginary parts of HN equation are given by [301]:

$$\varepsilon'(\omega) = \varepsilon_\infty + (\varepsilon_s - \varepsilon_\infty)\frac{\cos(\beta_{hn}\Phi)}{[1+2(\omega\tau_{hn})^{1-\alpha_{hn}}\sin\left(\frac{\pi\alpha_{hn}}{2}\right)+(\omega\tau_{hn})^{2(1-\alpha_{hn})}]^{\frac{\beta_{hn}}{2}}} \tag{6.3}$$

and

$$\varepsilon''(\omega) = (\varepsilon_s - \varepsilon_\infty)\frac{\sin(\beta_{hn}\Phi)}{\left[1+2(\omega\tau_{hn})^{1-\alpha_{hn}}\sin\left(\frac{\pi\alpha_{hn}}{2}\right)+(\omega\tau_{hn})^{2(1-\alpha_{hn})}\right]^{\frac{\beta_{hn}}{2}}} \tag{6.4}$$

where,

$$\Phi = \tan^{-1}\frac{(\omega\tau_{hn})^{1-\alpha_{hn}}\cos(\pi\alpha_{hn}/2)}{1+(\omega\tau_{hn})^{1-\alpha_{hn}}\sin(\pi\alpha_{hn}/2)}$$

The $\varepsilon'(\omega)$ data have been fitted according to eq. (6.3) and the best fitted curves are shown in Figs. 6.1 (a, b & c), where the symbols are the experimental data and red solid lines represent the best fits with eq. (6.3). The obtained values of α_{hn} and β_{hn} are presented in Table 6.1. From Table 6.1, it is observed that for PEDOT nanoparticles and nanofibers, the values of $\alpha_{hn} \approx 0$ and $\beta_{hn} \approx 1$. However, for PEDOT nanotubes the values of α_{hn} and β_{hn} lie in the range of 0.31-0.20 and 0.35-0.69, respectively.

The obtained values of α_{hn} and β_{hn} suggest the presence of Debye type relaxation in nanoparticles and nanofibers whereas non-Debye type relaxation in nanotubes system. In case of nanoparticles, the confinement of charge carriers along all the directions and in nanofibers, the confinement is along the diameter, which reduces the random motion of charge carriers under AC electric field. Whereas, in case of nanotubes, charge carriers can make random motion along all directions under the application of AC electric field. This may be the reason of observed Debye relaxation in nanoparticles and nanofibers whereas non-Debye relaxation in nanotubes.

Table 6.1: *Calculated values of α_{hn} and β_{hn} from real part of dielectric permittivity plots of PEDOT nanostructures at different dopant concentrations.*

Sample name	α_{hn}	β_{hn}
PEDOT nanoparticles		
0.003M DBSA	0.001	0.99
0.01M DBSA	0.003	0.97
0.1M DBSA	0.004	0.96
1M DBSA	0.005	0.95
PEDOT nanofibers		
0.03M SDS	0.002	0.99
0.1M SDS	0.004	0.98
0.5M SDS	0.006	0.97
1M SDS	0.007	0.97
PEDOT nanotubes		
0.001M CSA	0.31	0.35
0.01M CSA	0.29	0.39
0.1M CSA	0.25	0.45
1M CSA	0.20	0.69

In general, the dielectric loss factor $\varepsilon''(\omega)$ arises due to three different distinct effects [303]:

$$\varepsilon''(\omega) = \varepsilon''_{dc} + \varepsilon''_{MW} + \varepsilon''_{dip} \tag{6.5}$$

where ε''_{dc}, ε''_{MW} and ε''_{dip} are DC conductance, Maxwell-Wagner or interfacial polarization and dipole orientation (Debye loss factor), respectively. The log-log plot of $\varepsilon''(\omega)$ *vs*. ω depicts a straight line if the DC conductivity contribution is more and it will be sigmoidal curve if the polarization contribution is more in the system.

Figures 6.3 (a, b & c) present the room temperature log-log $\varepsilon''(\omega)$ *vs.* ω plots of PEDOT nanoparticles, nanofibers and nanotubes with varying dopant concentration. The figures show that $\varepsilon''(\omega)$ increases linearly with decreasing frequency for all nanostructured systems, which suggests that DC conductivity effect is more prominent than that of interfacial polarization in all the PEDOT nanostructures.

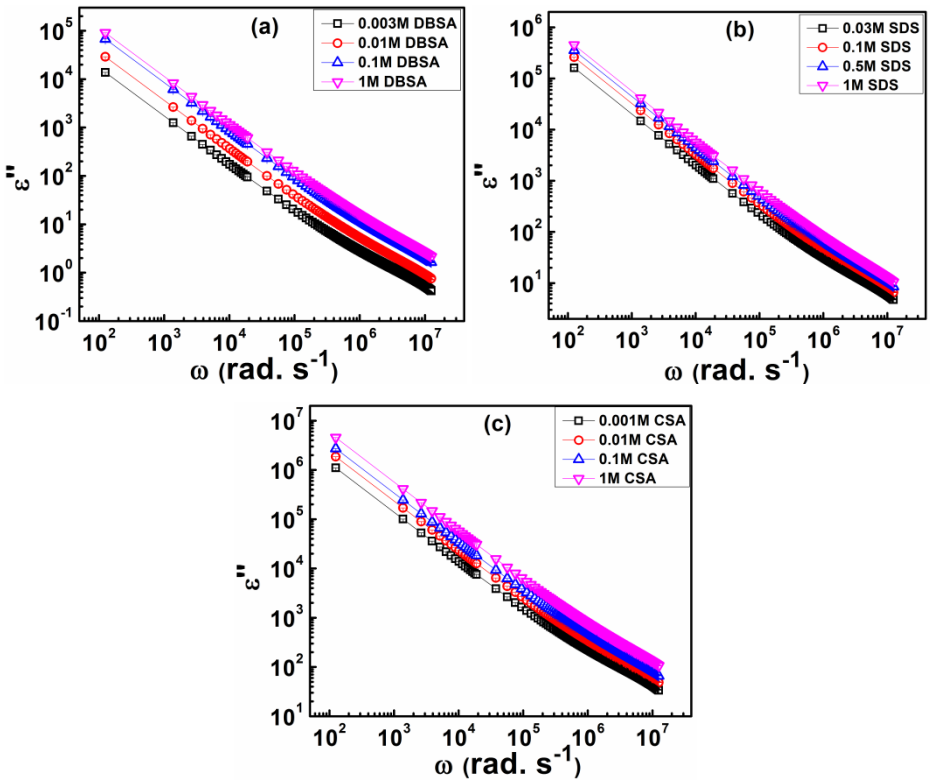

Figure 6.3: log-log plots of ε'' *vs.* ω at room temperature for PEDOT (a) nanoparticles, (b) nanofibers and (c) nanotubes for different dopant concentrations. Error bars show the standard deviation.

6.2.2 Impedance formalism

Complex impedance formalism can provide information about the electrical conductivity and nature of charge carrier relaxation processes in a material. According to the Cole-Cole formalism, the complex impedance is expressed as [304]:

$$Z^*(\omega) = Z'(\omega) - iZ''(\omega) = R_\infty + \frac{R_0 - R_\infty}{[1 + (i\omega\tau_m)^{1-\alpha}]} \qquad (6.6)$$

where R_∞ and R_0 are the resistance when ($\omega \to \infty$) and ($\omega \to 0$), respectively. The parameter $\tau_m = RC$ is the relaxation time and $0 \leq \alpha \leq 1$ characterizes the distribution of the relaxation times. For an ideal Debye relaxation $\alpha = 0$.

On separating the real and imaginary parts of complex impedance (Z^*) can be expressed as [304]:

$$Z' = R_\infty \frac{(R_0 - R_\infty)\left\{1 + \frac{(\omega\tau_m)^{1-\alpha}\cos(1-\alpha)\pi}{2}\right\}}{1 + (\omega\tau_m)^{2(1-\alpha)} + 2(\omega\tau_m)^{1-\alpha}cos\{(1-\alpha)\pi/2\}} \tag{6.7}$$

and

$$Z'' = \frac{-(R_0 - R_\infty)(\omega\tau_m)^{1-\alpha}\sin\frac{(1-\alpha)\pi}{2}}{1 + (\omega\tau_m)^{2(1-\alpha)} + 2(\omega\tau_m)^{1-\alpha}cos\{(1-\alpha)\pi/2\}} \tag{6.8}$$

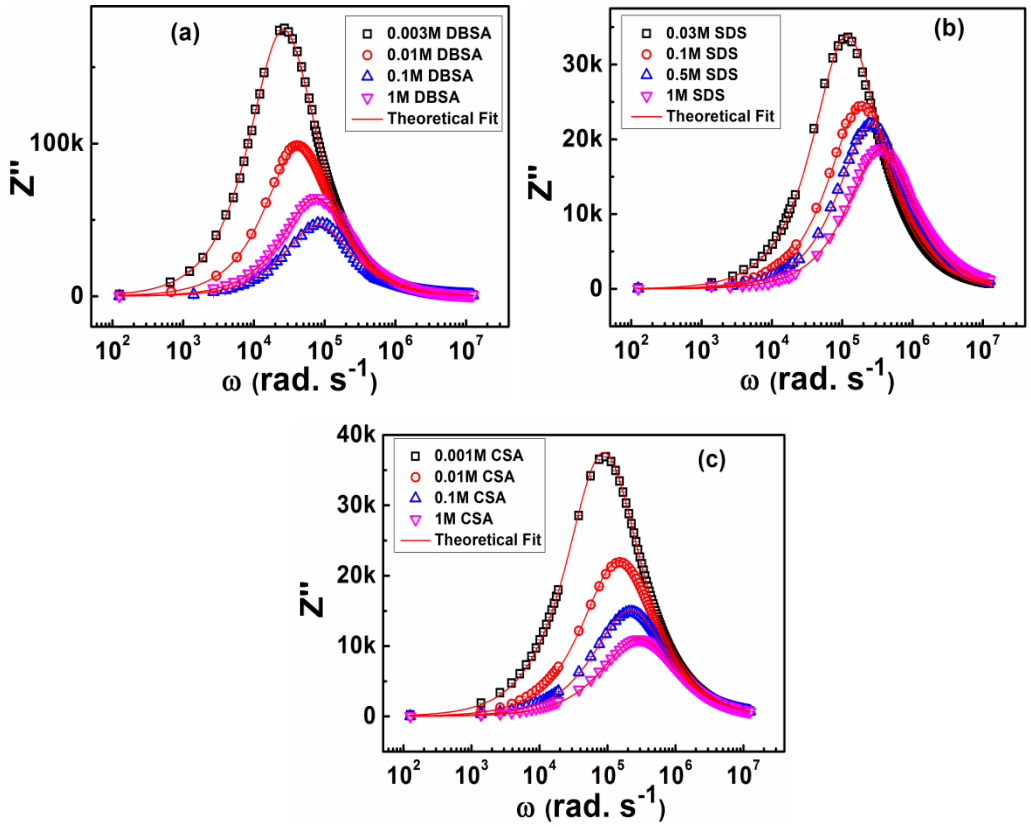

Figure 6.4: Variation of imaginary part of complex impedance (Z'') as a function of frequency for (a) DBSA doped PEDOT nanoparticles, (b) SDS doped PEDOT nanofibers and (c) CSA doped PEDOT nanotubes with varying dopant concentrations. Error bars show the standard deviation.

Figures 6.4 (a, b & c) show the frequency dependent room temperature imaginary part of complex impedance (Z'') of PEDOT nanoparticles, nanofibers and nanotubes for different dopant concentrations. It is observed that for all the nanostructured systems the impedance spectra exhibit a relaxation peak and it shifts towards higher frequency with increasing dopant concentration. The shifting of relaxation peak indicates the decrease of relaxation time i.e. faster response of charge carriers, which leads to higher conductivity as discussed in section 5.1 of Chapter 5.

Table 6.2: *Calculated values of α and β_{KWW} from the imaginary parts of impedance and modulus plots of PEDOT nanostructures at different temperatures.*

Temperature (K)	**1M DBSA doped nanoparticles**		**1M SDS doped nanofibers**		**1M CSA doped nanotubes**	
	α	β_{KWW}	α	β_{KWW}	α	β_{KWW}
80	0	0.99	0	0.99	0.68	0.75
140	0.001	0.98	0.001	0.98	0.67	0.75
180	0.002	0.98	0.003	0.99	0.66	0.76
220	0.003	0.99	0.005	0.98	0.65	0.77
260	0.007	0.97	0.007	0.98	0.64	0.77
300	0.008	0.96	0.008	0.97	0.63	0.79

The imaginary part of complex impedance (Z'') as a function of frequency for 1M DBSA, SDS and CSA doped PEDOT nanostructures (nanoparticles, nanofibers and nanotubes) for different temperatures is shown in Figs. 6.5 (a, b & c). From Figs. 6.5(a, b & c) it is observed that with increasing temperature the magnitude of Z'' decreases and the peak frequency (ω_m) shifts to the higher values. The shift of relaxation peak towards higher frequency with increasing temperature is attributed to the presence of thermally activated relaxation process. The overlapping of Z'' values in the higher frequency (> 10^6 Hz) at different temperatures is attributed to the release of space charges. The experimentally obtained values of Z'' are fitted according to eq. (6.8), where the symbols are the experimental points and red solid lines are the best fitted curves according to eq. (6.8). The obtained values of

α from the best fitted curves are presented in Table 6.2. The almost zero values of α for PEDOT nanoparticles and nanofibers systems indicate the presence of Debye type relaxation. However, the non- zero values of α in PEDOT nanotubes suggests the presence of non-Debye relaxation process i.e. distribution of relaxation time.

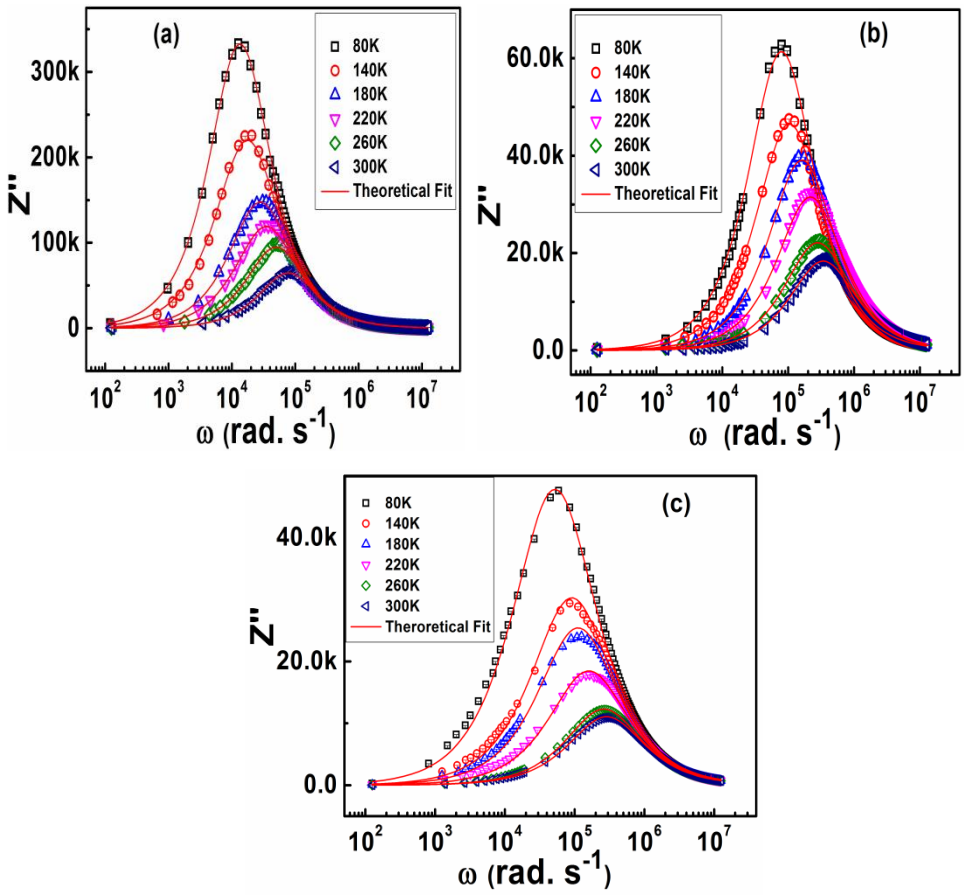

Figure 6.5: Variation of imaginary part of complex impedance (Z'') as a function of frequency for (a) 1M DBSA doped PEDOT nanoparticles, (b) 1M SDS doped PEDOT nanofibers and (c) 1M CSA doped PEDOT nanotubes at different temperatures. Error bars show the standard deviation.

6.2.3 Modulus formalism

The electric modulus formalism corresponds to the relaxation of electric field when the electric displacement remains constant and the electric modulus represents the real dielectric relaxation process by suppressing the space charge polarization or electrode polarization effects. The relaxation of an electric field in a charge carrier system results from the carrier hopping over potential barriers, which leads to short-range AC conductivity and long-range DC conductivity. The conductivity relaxation

in conjugated polymers arises due to the different of carrier hopping from that of dielectric relaxation [305]. The main advantages of study the modulus formalism is that the electrode polarization effects are suppressed in this representation and it is the effective approach for conductive system where the dielectric relaxation can be masked. According to Macedo [306], electric modulus formalism M^* can be calculated from the inverse of complex permittivity ($M^* = 1/\varepsilon^*$) expressed as:

$$M^* = \frac{1}{\varepsilon^*} = M' + iM'' = \frac{\varepsilon'}{\varepsilon'^2 + \varepsilon''^2} + i\frac{\varepsilon''}{\varepsilon'^2 + \varepsilon''^2} \qquad (6.9)$$

where M' and M'' are the real and imaginary parts of complex modulus, respectively.

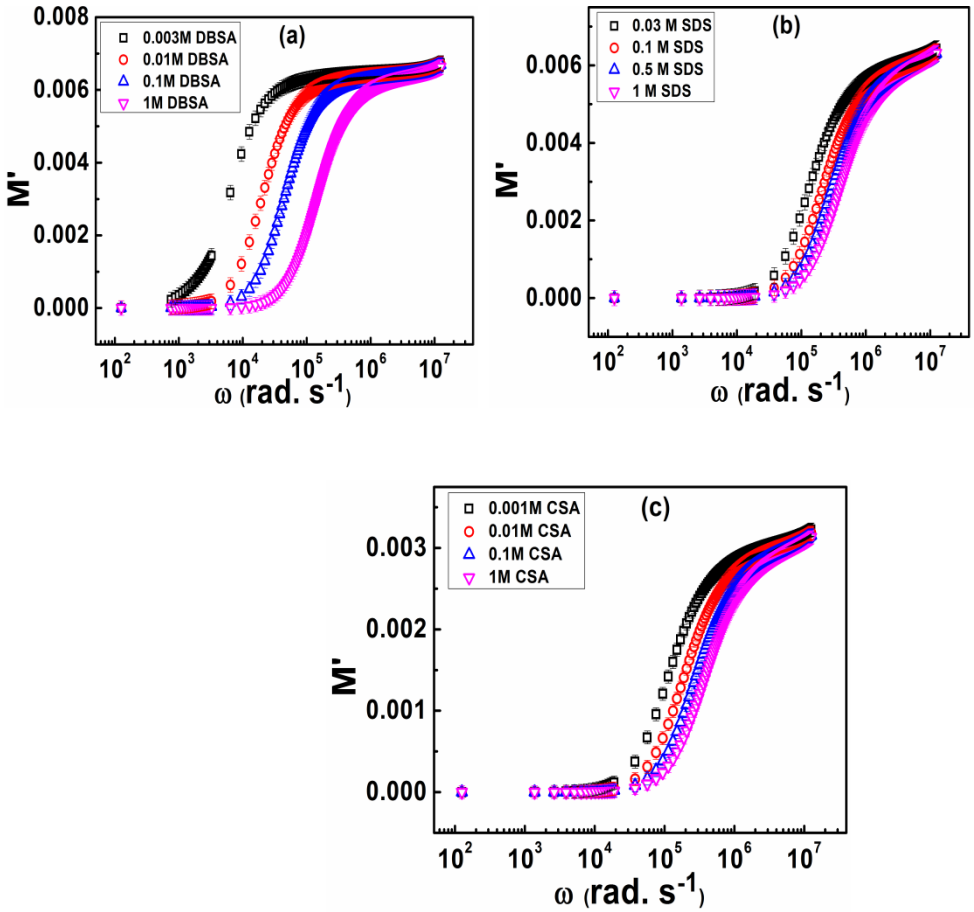

Figure 6.6: Variation of real modulus M' with frequency for PEDOT (a) nanoparticles, (b) nanofibers and (c) nanotubes at room temperature for different dopant concentrations. Error bars show the standard deviation.

Figures 6.6 (a, b & c) depict the variation of real modulus M' with frequency for PEDOT nanoparticles, nanofibers and nanotubes for different dopant concentrations at room temperature. The real part of modulus formalism M' exhibits

a sigmoidal shape that increases with increasing frequency and approaches asymptotic value M_∞, at high frequencies. The almost zero value of M' at lower frequency indicates the removal of electrode polarization effect. The dispersive behavior of M' at higher frequencies suggests that the conduction process is due to long-range motion of charge carriers [307].

The study of imaginary modulus gives detail information about the charge carrier relaxation dynamics. The room temperature frequency dependent M'' plots of PEDOT nanoparticles, nanofibers and nanotubes for different dopant (DBSA, SDS and CSA) concentrations are shown in Figs. 6.7 (a, b & c). The imaginary part of modulus M'' exhibits smaller value at lower frequencies and it can be attributed to the large value of capacitance associated with the electrode, whereas at higher frequencies well-defined relaxation peak is observed for all the nanostructured systems. The frequency at which the peak appears is known as relaxation frequency (ω_{max}) and the relaxation time (τ_{max}) can be calculated by using the expression $\omega_{max.}\tau_{max} = 1$. The frequency to the left of the relaxation peak is the region of frequency in which the charge carriers can have long-range motion i.e. DC conductivity. The frequency region to the right of relaxation peak, the charge carriers are spatially confined to their potential well and they can have only short range motion i.e. AC conductivity [308]. Under the application of alternating electric field at a particular temperature, the intrinsic immobilized free charge carriers can move freely up to a certain frequency. After the certain frequency region the free charges are blocked at the electrode and sample interface, as a consequence the dielectric difference between them produces interfacial polarization. With increasing dopant concentration the number of free charge carriers increases and they accumulate at the interface between the electrode and sample resulting in the decrease of relaxation time [309]. The shifting of the maximum relaxation peak towards higher frequency in M'' spectra indicates the enhancement of dc conductivity according to the following expression [310]:

$$\sigma_{dc} = \frac{\varepsilon_o \omega_{max}}{M''} \tag{6.10}$$

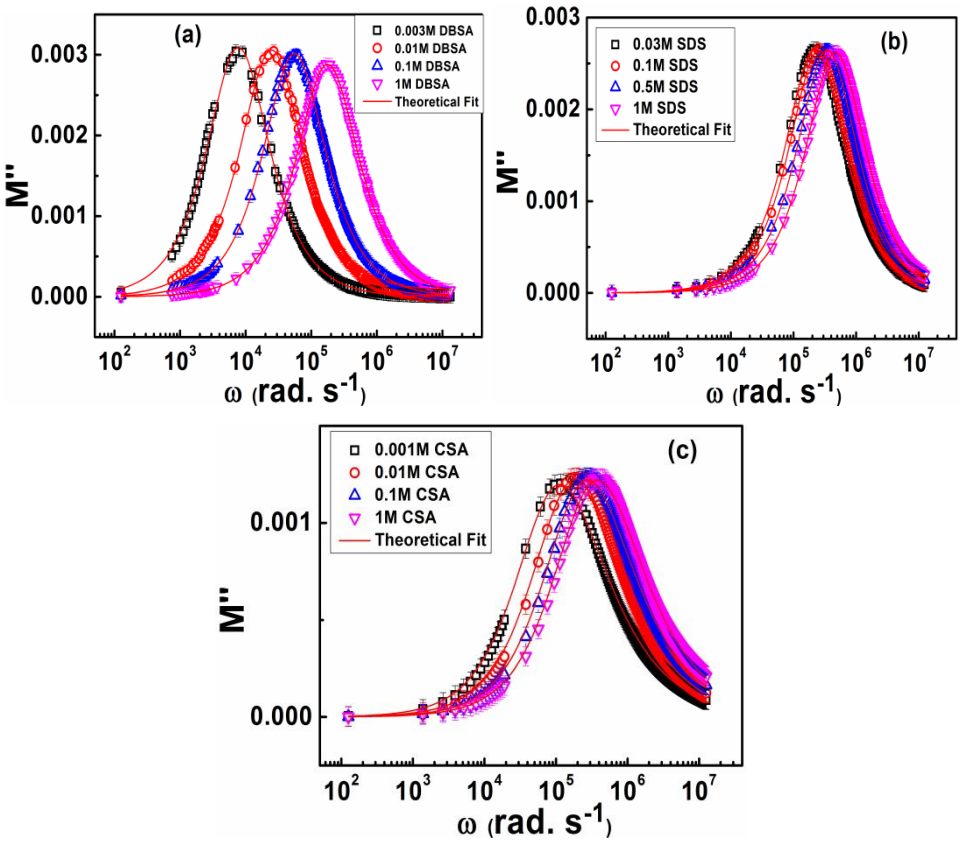

Figure 6.7: Variation of imaginary modulus *M″* with frequency for PEDOT (a) nanoparticles, (b) nanofibers and (c) nanotubes at room temperature for different dopant concentrations. Error bars show the standard deviation.

In order to understand the relation between the interfacial polarization and temperature, the isothermal dependence of *M″* with frequency for 1M DBSA, 1M SDS and 1M CSA doped PEDOT nanostructures are presented in Figs. 6.8 (a, b & c). From Figs.6.8 (a, b & c), it is observed that the relaxation peak shifts towards higher frequencies with increasing temperature. With increasing temperature the mobility of the charge carriers increases due to the increase in thermal energy of charge carriers as a result more charge carriers can accumulate at the interface within the bulk sample. This results the shift of relaxation peak towards higher frequency, indicating a thermally activated process in this frequency region [311].

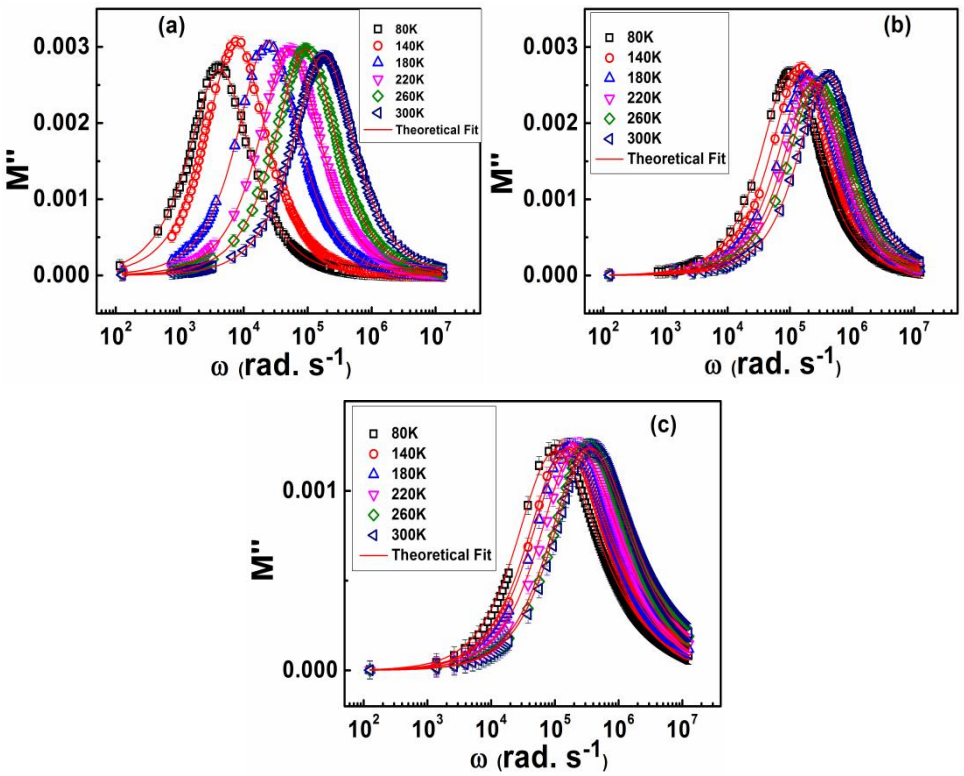

Figure 6.8: Variation of imaginary modulus *M″* with frequency for PEDOT (a) 1M BDSA doped nanoparticles, (b) 1M SDS doped nanofibers and (c) 1M CSA doped nanotubes at different temperatures. Error bars show the standard deviation.

The complex electric modulus can be expressed by the following equation [312]:

$$M^*(\omega) = M_\infty \left[1 - \int_0^\infty \exp(-\omega t)\left(\frac{d\Phi}{dt}\right) dt\right] \tag{6.11}$$

where the function Φ(t) is the time evolution of the electric field within the material and it is defined empirically by Kohlrausch-Williams-Watts (KWW) function as:

$$\Phi(t) = \exp\left[-\left(\frac{t}{\tau_{max}}\right)^{\beta_{KWW}}\right] \tag{6.12}$$

where τ_{max} is the characteristic conductivity relaxation time and β_{KWW} is the Kohlrausch exponent with the condition $0 \leq \beta_{KWW} \leq 1$. The value of β_{KWW} = 1 for ideal Debye behavior and less than 1 for non-Debye relaxation process. The smaller the value of β_{KWW}, the larger is the deviation of relaxation time from the ideal Debye-type relaxation. Bergman [313] modified the KWW function for fitting approach in

the frequency domain and the imaginary part of electric modulus was approximated as:

$$M''(\omega) = \frac{M''_{max}}{[(1-\beta_{KWW}) + (\frac{\beta_{KWW}}{1+\beta_{KWW}})\{\beta_{KWW}\left(\frac{\omega_{max}}{\omega}\right) + (\omega/\omega_{max})^{\beta_{KWW}}\ ]} \quad (6.13)$$

The imaginary part of electric modulus for different temperatures were fitted according to eq. (6.13) and shown in Figs. 6.8 (a, b & c), where the symbols are experimental data and red solid lines are the best fitted lines. The extracted parameter β_{KWW} from the fitted plots is presented in Table 6.2. For all the measured temperatures it is observed that the values of β_{KWW} ≈1 for nanoparticles and nanofibers, suggesting the presence of Debye type relaxation. However, for nanotubes system β_{KWW} < 1, which indicates the non-Debye type relaxation mechanism in the PEDOT nanotubes. The observed Debye type relaxation mechanism in nanoparticles and nanofibers and non-Debye behavior in nanotubes can be explained in the same way as discussed in permittivity analysis section.

The variation of the relaxation time (τ_{max}) with temperature can be described by an Arrhenius relation and expressed as [314]:

$$\tau_{max} = \tau_o \exp\left(\frac{E_a}{k_B T}\right) \quad (6.14)$$

where τ_o is the pre exponential factor, k_B is the Boltzmann constant and E_a is the activation energy associated with the relaxation process of charge carrier. The Arrhenius plot of lnτ_{max} *vs.* 1000/T for 1M DBSA, 1M SDS and 1M CSA doped PEDOT nanostructures (nanoparticles, nanofibers and nanotubes) are shown in Fig. 6.9. The slope of the best fitted straight line gives the activation energy and obtained values are tabulated in Table 6.3. The activation energy found to be minimum for 1M CSA doped nanotubes, which leads to higher conductivity as observed in section 5.1 of Chapter 5.

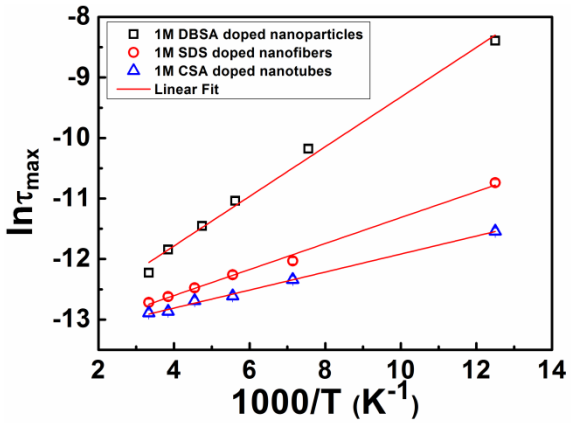

Figure 6.9: $\ln\tau_{max}$ *vs.* 1000/*T* plot of 1M DBSA, 1M SDS and 1M CSA doped PEDOT nanoparticles, nanofibers and nanotubes, respectively. Error bars show the standard deviation.

Table 6.3: *Calculated values of activation energy (E_a) of 1M DBSA, SDS and CSA doped PEDOT nanoparticles, nanofibers and nanotubes*

Sample name	E_a (±0.01) (meV)
1M DBSA doped PEDOT nanoparticles	36.23
1M SDS doped PEDOT nanofibers	18.11
1M CSA doped PEDOT nanotubes	12.94

6.3 Scaling properties analysis of PEDOT nanoparticles, nanofibers and nanotubes

6.3.1 Scaling of impedance formalism

The scaling behavior in disordered materials is often ascribed to the motion of the localized charge carriers, which at high frequencies perform a sequence of forward-backward hopping and at low frequencies the charge transport extends over long distances [315]. The imaginary (Z'') part of impedance formalism can be scaled according to the expression:

$$\frac{Z''(\omega)}{Z''_m} = F\left(\frac{\omega}{\omega_m}\right) \tag{6.15}$$

where the Z'' axis is scaled by Z''_m and frequency axis by ω_m. Figures 6.10 (a, b & c) depict the scaling plots of Z'' at different temperatures for 1M DBSA, SDS and CSA doped PEDOT nanostructures (nanoparticles, nanofibers and nanotubes). From Figs. 6.10 it is observed that the curves at different temperatures collapse into a single master plot implying that the relaxation process of charge carriers is temperature independent.

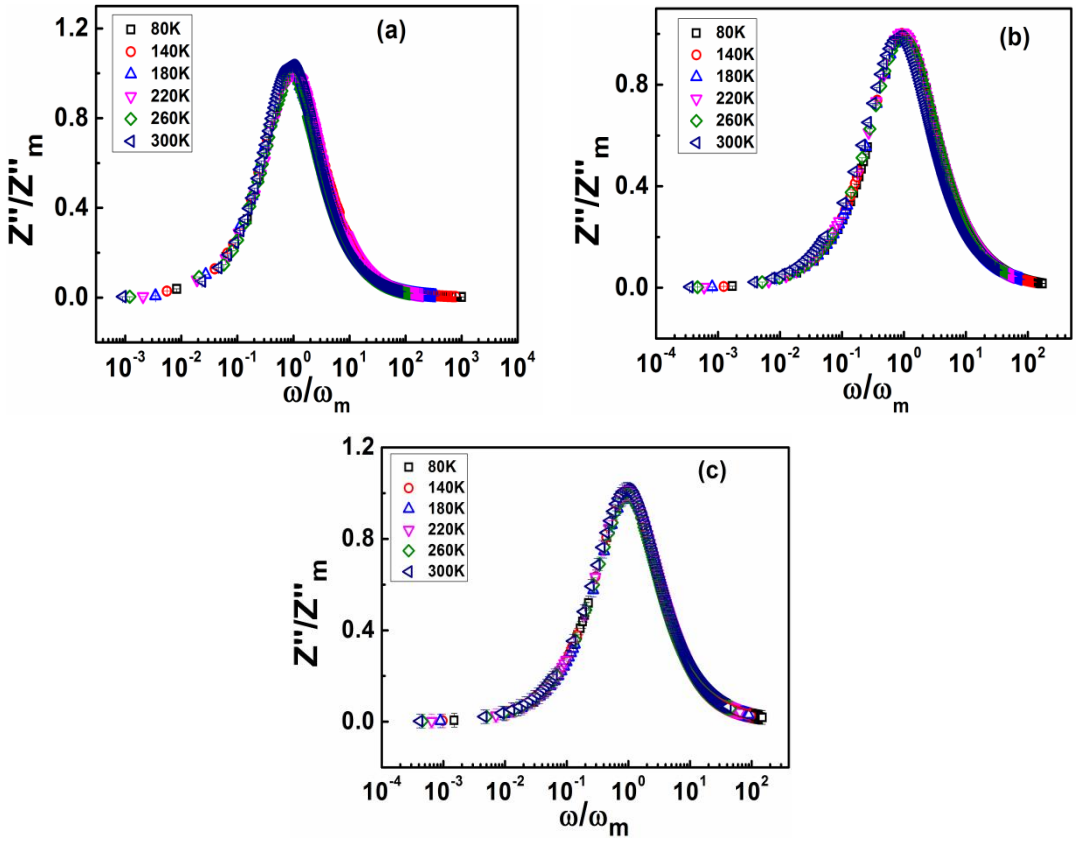

Figure 6.10: Scaling plots of Z'' at different temperatures for (a) 1M DBSA doped PEDOT nanoparticles, (b) 1M SDS doped PEDOT nanofibers and (c) 1M CSA doped PEDOT nanotubes. Error bars show the standard deviation.

6.3.2 Scaling of modulus formalism

Figures 6.11 (a, b & c) represent the scaling plots of M'' at different temperature for 1M DBSA, SDS and CSA doped PEDOT nanostructures (nanoparticles, nanofibers and nanotubes). In the scaling plot the x- axis is scaled by relaxation frequency ω_{max} and y-axis is scaled by M''_{max} at different temperatures according to the relation:

$$\frac{M''(\omega)}{M''_{max}} = F\left(\frac{\omega}{\omega_{max}}\right) \tag{6.16}$$

The scaling plot shows almost superimposition behavior leading to a single master curve at different temperatures. The overlapping of the individual modulus plot onto a single master curve indicates that the charge carrier relaxation process is independent of temperature [316]. The scaling master plot gives the dimensionless modulus and as a function of dimensionless frequency and the existence of such master plot is termed as time temperature superposition principle (TTSP).

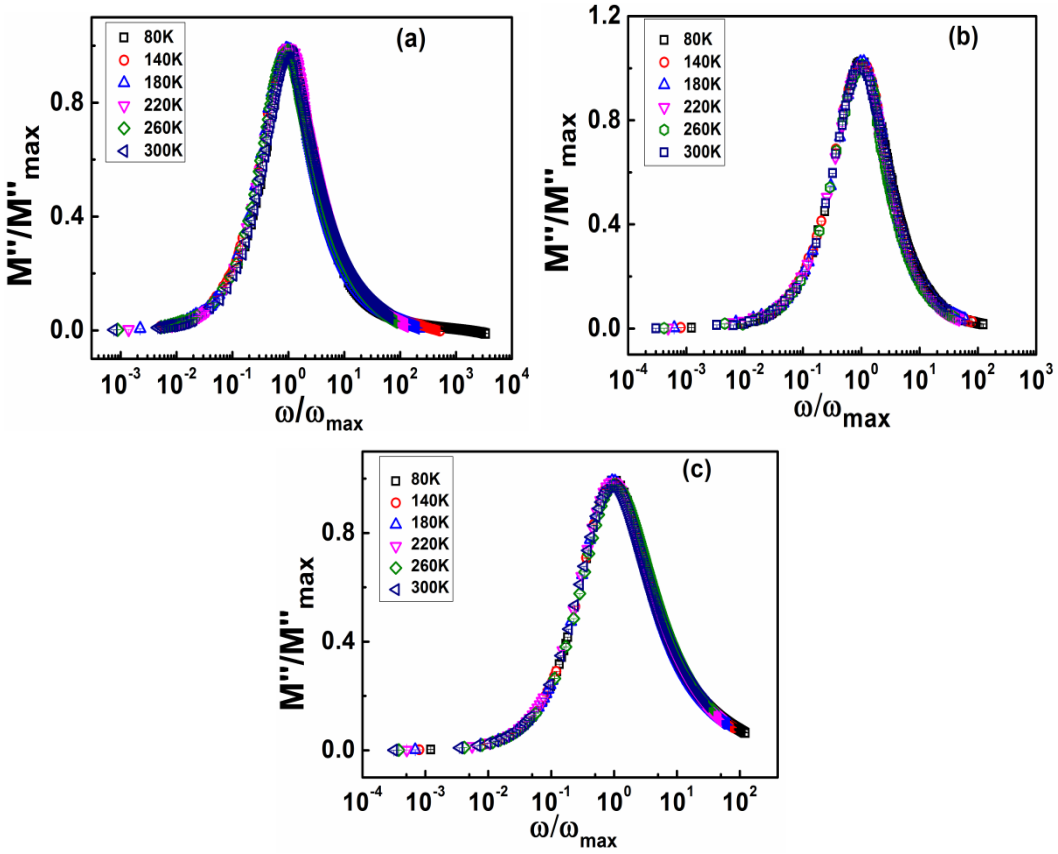

Figure 6.11: Scaling plots of *M´´* at different temperatures for (a) 1M DBSA doped PEDOT nanoparticles, (b) 1M SDS doped PEDOT nanofibers and (c) 1M CSA doped PEDOT nanotubes. Error bars show the standard deviation.

6.4 Summary

In summary, the dielectric properties and charge carriers' relaxation dynamics in synthesized poly(3,4-ethylenedioxythiophene) nanoparticles, nanofibers and nanotubes have been investigated as a function of frequency and temperature through the framework of dielectric permittivity, impedance and modulus formalisms in the frequency and temperature range of 20 Hz – 2 MHz and 80 K – 300 K, respectively.

The dielectric permittivity formalism analysis has been performed to obtain information about the charge carrier polarization. The high values of real part of dielectric permittivity at lower frequencies ($<10^4$ Hz) can be attributed to the interfacial polarization effect, whereas the decrease of ε' with increase in frequency corresponds to dipole relaxation. From the fitted plots of real part of dielectric permittivity with HN equation, it is observed that for PEDOT nanoparticles and nanofibers, the charge carriers follow Debye relaxation, whereas in PEDOT nanotubes they follow non-Debye relaxation. This may be attributed to the confinement of charge carriers in case of nanoparticles and nanofibers which restrict their movement, whereas, in case of nanotubes charge carriers can make random motion along all directions under the application of AC electric field. The log-log plots of imaginary permittivity *vs.* frequency exhibit that imaginary permittivity increases with decreasing frequency for all the nanostructures, which can be ascribed to the higher contribution of dc conductivity as compared to that of electrode polarization effects.

The impedance formalism analysis provides the information about the conductivity of the material and charge carrier relaxation behavior. The imaginary part of impedance Z'' exhibits a relaxation peak for all the nanostructures and it shifts towards higher frequency side with increasing dopant concentration and temperature. The shifting of relaxation peak towards higher frequency indicates the decrease of relaxation time of charge carriers i.e. enhancement in response of charge carriers. From the fitting of experimentally observed impedance data with Cole-Cole equation, it is observed that for nanoparticles and nanofibers systems the charge carriers follow Debye type relaxation whereas for nanotubes they follow non-Debye relaxation.

Modulus formalism is a powerful approach to understand the conductivity relaxation dynamics of charge carriers. The real part of modulus tends to zero with decreasing frequency which suggests the elimination of electrode polarization effect. The dispersive behavior of M' at higher frequency side indicates the presence of charge carriers relaxation. The imaginary part of modulus shows a relaxation peak which shifts towards higher frequency with increasing dopant concentration as well as temperature. The frequencies to the left of relaxation peak signify the region in

which charge carriers can take long range motion leading to DC conductivity. Whereas, the frequency regions to the right of relaxation peak the charge carriers are spatially confined and can make short range motion i.e. AC conductivity. The shifting of relaxation peak towards higher frequency with increasing dopant concentration and temperature indicates the faster response of charge carriers leading to higher conductivity.

Chapter 7

Conclusions and Future directions

This chapter summaries the major conclusions drawn from the present thesis work, which deals with the electrical transport and dielectric studies of different poly(3,4-ethylenedioxythiophene) nanostructures viz., nanoparticles, nanofibers and nanotubes. The future research potential in this area has also been discussed in the end of the chapter.

7.1 Conclusions

The present thesis deals with the synthesis and studies of structural, vibrational, thermal, electrical and dielectric properties of poly(3,4-ethylenedioxythiophene) nanostructures viz., DBSA doped nanoparticles, SDS doped nanofibers and CSA doped nanotubes by employing different characterization techniques. The major conclusions drawn from the present work are as given below:

1. High resolution transmission electron microscopy (HRTEM) studies reveal the formation of PEDOT nanostructures viz., nanoparticles, nanofibers and nanotubes. The average diameters of 0.003M and 1M DBSA doped PEDOT nanoparticles are found to be 13 and 40 nm, respectively. The average diameter of 0.03M and 1M SDS doped PEDOT nanofibers are 14 and 15.5 nm, respectively. The diameter of the nanotubes is also observed to increase with increasing CSA concentration. The average outer diameters of the nanotubes are found to be 65 nm and 101 nm for 0.001M and 1M CSA concentration, respectively. DBSA, SDS and CSA act as surfactants as well as functional dopants for the synthesis of different PEDOT nanostructures. The size of the micelle determines the diameter of the nanostructures. With increasing dopant concentration the size of micelle increases leading to the increase in the diameter of nanostructures.

2. XRD analysis shows the semi-crystalline nature of PEDOT nanostructures namely, nanoparticles, nanofibers and nanotubes. With increasing dopant concentration, the crystallite size increases for all the PEDOT nanostructures, which could be attributed to the increase in nanostructures size and is consistent with the HRTEM images. The increase in degree of crystallinity (*K*) with increasing dopant concentration indicates the enhancement in ordering of polymer chains in the nanostructures. Higher value of percentage of degree of crystallinity (46.19%) for 1M CSA doped PEDOT nanotubes can be attributed to the enhanced ordering of polymer chains. The Raman spectra of PEDOT nanoparticles and nanotubes show that the $C_\alpha=C_\beta$ symmetric stretching deformation band is shifted towards lower wavenumber side with increasing dopant concentration. The red shifting of $C_\alpha=C_\beta$ symmetric stretching deformation band with increasing dopant concentration indicates the conformational transition from benzenoid to quinoid structure. The polymer chain has a helically twisted structure in the benzenoid configuration, whereas in the oxidized quinoid state, the polymer main chain has planar configuration and the planarity of the main chain increases with increasing quinoid units in the main chain i.e. with increasing oxidation. The increase of linearity of the polymer chains with increasing dopant concentration facilitates the hopping of charge carriers.

3. Thermogravimetric analysis is usually used to monitor the thermal stability of polymers. The change in slope in the TGA plot corresponds to change in degradation mechanism. Thermogravimetric plots depict two step weight loss patterns for all the three PEDOT nanostructures, viz., nanoparticles, nanofibers and nanotubes. The thermal stability of all the nanostructures is found to increase with increasing dopant concentration, which is attributed to the increase of crystallinity. The 1M CSA doped PEDOT nanotubes exhibit relatively slower decomposition rate during the heating process, which is consistent with the degradation activation energy calculation. This slower decomposition rate i.e. higher thermal stability of 1M CSA doped PEDOT nanotubes is attributed to the higher degree of crystallinity (46.19%).

4. The temperature dependent resistivity for all the nanostructured systems shows semiconducting behavior i.e. resistivity decreases with increasing temperature in the entire measured temperature range of 5 – 300 K. From the resistivity analysis it is observed that dopant type and dopant concentration have significant effect on charge transport mechanism. The decrease of resistivity with increasing dopant concentration can be ascribed to the introduction of traps in the HOMO-LUMO gap, which helps in enhancing the hopping rate. At low doping concentration, the number of defect states is less in the band gap, and the charge carriers hop to a longer distance that reduces the hopping probability. With increasing doping level, the inter-chain hopping probability increases due to the increase of interstitial dopant counter-ions which serve as defect sites. Because of the local lowering of the potential energy for the charge carriers at the dopant ions, the wave-function overlapping increases between the two chains leading to higher hopping probability. The negative slope of (W vs. T) plots indicates that the synthesized samples fall in the insulating regime of the metal-insulator transition. The charge transport in DBSA doped nanoparticles and SDS doped nanofibers follow 3D VRH mechanism, whereas a crossover from 3D VRH mechanism to 1D VRH mechanism is observed in CSA doped nanotubes below 10 K. This is attributed to the presence of larger bulky cycloaliphatic ring in CSA anion restricts the twisting of polymer chains while it fills up the space between polymer chains. At low temperatures (< 10 K), the charge carriers have less thermal energy as a result they cannot make inter-chain hopping due to the absence of chain twisting leading to 1D VRH mechanism in case of CSA doped nanotubes. However, the long alkyl chains in DBSA and SDS cannot restrict the twisting of polymer chains, which leads to random orientation of polymer chains giving rise to 3D VRH mechanism in nanoparticles and nanofibers. The decrease of characteristic Mott temperature with increasing dopant concentration can be attributed to the enhancement of polymer chains ordering in the nanostructures (nanoparticles, nanofibers and nanotubes). The smaller value of Mott temperature (9.2×10^3 K) for 1M CSA doped sample leads to lower room temperature resistivity (0.04 Ωcm). The average hopping distance and average hopping energy decrease with increasing dopant concentration for all

the nanostructured systems which results in the enhancement of hopping rate between the localized states due to formation of more hopping sites between the band gap.

5. The isothermal magnetoresistance (MR) has been measured at eight different temperatures (5, 10, 20, 30, 50, 100, 200 & 300K) in the magnetic field range of 0 – 8 T. The MR values show a transition from positive to negative with increasing temperature for all the nanostructures. The observed positive and negative MR have been analyzed using wave-function shrinkage model and quantum interference model, respectively. The positive to negative cross-over temperature is found to decrease with increasing dopant concentration for all the nanostructures which can be attributed to the enhanced crystallinity that is consistent with XRD results. The smaller magnitude of negative MR than that of positive MR suggests that the quantum interference effect is much weaker than the wave -function shrinkage effect. The high value of negative MR (~ 3.58%) in case of 1M CSA doped PEDOT nanotubes indicates the higher delocalization of charge carriers, which gives rise to smaller room temperature resistivity (0.04 Ωcm).

6. The frequency dependent conductivity exhibits two distinct regimes for all the PEDOT nanostructures: the frequency independent plateau at lower frequency and a frequency dependent part at higher frequency. The frequency region of constant conductivity extends to higher frequency with increasing dopant concentration and temperature indicating the enhancement of DC conductivity. This frequency independent conductivity is due to the free charges which may undergo random diffusion via activated hopping. AC conductivity study displays significant enhancement in the conductivity with increasing dopant concentration for all the nanostructures. With increasing dopant concentration the number of free charge carriers increases leading to the increase of frequency independent conductivity i.e., DC conductivity. The frequency dependent conductivity in the higher frequency is ascribed to the activation of the trapped charges in the polymeric system. The temperature dependence of universal frequency exponent *s* reveals that the correlated barrier hopping (CBH) is the dominating charge transport

mechanism in the nanostructured systems under AC electric field. The scaling behavior of AC conductivity at different temperatures suggests that the conduction mechanism of charge carriers is temperature independent.

7. The dielectric permittivity formalism analysis has been performed to obtain information about the charge carrier polarization. It is observed that all the samples exhibit the higher values of ε' and ε'' in the low frequency region that decrease with increasing frequency attaining a constant value at about 10^6 Hz. The high values of real part of dielectric permittivity at lower frequencies ($< 10^4$ Hz) can be attributed to the interfacial polarization effect due to the charge carrier accumulation at the electrode-sample interface. At lower frequencies, the periodic reversal time of electric field is quite large as a result charge carriers get sufficient time to follow the direction of applied field leading to the increase of ε'. Whereas at high frequencies due to the high periodic reversal of applied AC field the charge carriers are no longer able to respond to applied field resulting in the decrease of ε'. As temperature increases the real part of dielectric permittivity increases, which is ascribed to the fact that increasing temperature mobilizes the polymer chains, reducing pinning leading to greater number of charge carrier participation in the relaxation process for a given frequency. From the fitted plots of real part of dielectric permittivity with HN equation it is observed that for PEDOT nanoparticles and nanofibers, the charge carriers follow Debye relaxation, whereas in PEDOT nanotubes they follow non-Debye relaxation. This may be attributed to the confinement of charge carriers in case of nanoparticles and nanofibers that restrict their movement, whereas in the case of nanotubes charge carriers can make random motion along all directions under the application of AC electric field. The log-log plots of imaginary permittivity vs. frequency exhibit that imaginary permittivity increases with decreasing frequency for all the nanostructures, which can be ascribed to the higher contribution of dc conductivity as compared to that of electrode polarization effects.

8. The impedance formalism analysis provides the information about the conductivity of the material and charge carrier relaxation behavior. The

imaginary part of impedance Z'' exhibits a relaxation peak for all the nanostructures that shifts towards higher frequency with increasing dopant concentration and temperature, which indicates the decrease of relaxation time of charge carriers. From the fitting of experimentally observed data with Cole-Cole equation, it is observed that for nanoparticles and nanofibers the charge carriers follow Debye type relaxation whereas for nanotubes they follow non-Debye relaxation. The magnitude of Z'' decreases and the peak frequency (ω_m) shifts towards higher frequency with increasing dopant concentration and temperature which indicates the decrease of relaxation time leading to higher conductivity. The scaling behavior of Z'' at different temperatures suggests that the charge carriers relaxation is a temperature independent process.

9. Modulus formalism is a powerful approach to understand the conductivity relaxation dynamics of charge carriers. The real part of modulus tends to zero at low frequencies indicating that the effect of electrode polarization gives a negligible contribution and can be ignored. The dispersive behavior of M' at higher frequency side indicates the presence of charge carriers relaxation. The imaginary part of modulus shows a relaxation peak which shifts towards higher frequency with increasing dopant concentration as well as temperature. The frequency to the left of relaxation peak signify the region in which charge carriers can have long range motion leading to the DC conductivity. Whereas, in the frequency region to the right of relaxation peak, the charge carriers are spatially confined and can make short range motion i.e., AC conductivity. The frequency range where the peak occurs is an indication of the transition from long-range to short-range motion of charge carriers. The shifting of relaxation peak towards higher frequency with increasing dopant concentration and temperature indicates the faster response of charge carriers. The shifting of relaxation peak with increasing dopant concentration can be ascribed to the increase of localization length of PEDOT nanostructures that facilitates the charge carrier hopping leading to higher conductivity. The scaling behavior of imaginary modulus spectra at different temperatures indicates that the charge carrier relaxation is a temperature independent process.

7.2 Future directions

The field of conducting polymer nanostructures is an emerging area of research as they find wide-spread applications in different technological and biomedical applications because of their interesting properties. There is an enormous scope of further development of high performance conjugated conducting polymers and fabrication of different electronic devices based on them such as organic light emitting diodes, supercapacitors, sensors, electrochromic windows etc. Although extensive research work is going on in this field, the charge transport mechanism in such disordered systems is a challenging problem. It has been observed from the present thesis work that the transport properties of conducting polymer nanostructures can be tuned by varying dopant concentration, dopant type and the nanostructure shape.

1. In the present thesis we have studied structural, vibrational, thermal, transport and dielectric properties of poly(3,4-ethylenedioxythiophene) nanoparticles, nanofibers and nanotubes. This work can be extended to the different nanostructures of other conducting polymers like polyaniline (PAni), polypyrrole (PPy), polythiophene (PTh) etc.

2. Disorder is a critical parameter in conducting polymers that controls the transport properties in conducting polymers. From the present study it is observed that controlled synthesis can reduce the disorder. Further study is required to optimize the disorder in order to obtain enhanced electrical conductivity.

3. From the transport properties study it has been observed that shape and morphology of the nanostructures greatly influence the charge transport mechanism. For better understanding the charge transport mechanism in such disordered systems this work can be further extended by synthesizing different nanostructures such as nanoneedles, nanospheres, nanorods, nanosheets, quantum dots etc.

4. Although in the present thesis we have studied the transport properties of PEDOT nanostructures, the study on single nanostructure is important for potential nano-device applications. Intensive research on single nanostructure is going on, but researchers are far away from achieving the goal. Research in this field has great prospects both from theoretical and application points of view.